



저작자표시-비영리-변경금지 2.0 대한민국

이용자는 아래의 조건을 따르는 경우에 한하여 자유롭게

- 이 저작물을 복제, 배포, 전송, 전시, 공연 및 방송할 수 있습니다.

다음과 같은 조건을 따라야 합니다:



저작자표시. 귀하는 원저작자를 표시하여야 합니다.



비영리. 귀하는 이 저작물을 영리 목적으로 이용할 수 없습니다.



변경금지. 귀하는 이 저작물을 개작, 변형 또는 가공할 수 없습니다.

- 귀하는, 이 저작물의 재이용이나 배포의 경우, 이 저작물에 적용된 이용허락조건을 명확하게 나타내어야 합니다.
- 저작권자로부터 별도의 허가를 받으면 이러한 조건들은 적용되지 않습니다.

저작권법에 따른 이용자의 권리는 위의 내용에 의하여 영향을 받지 않습니다.

이것은 [이용허락규약\(Legal Code\)](#)을 이해하기 쉽게 요약한 것입니다.

[Disclaimer](#)

**Dissertation for the Degree of Doctor of Philosophy**

**Discrimination of PD Signal using Wavelet Transform  
for Insulation Diagnosis of GIS under HVDC**

**Supervisor : Prof. Gyung-Suk Kil**

**August 2019**

**Department of Electrical and Electronics Engineering**

**Graduate School of Korea Maritime and Ocean University**

**Guoming Wang**

工學博士 學位論文

HVDC에서 GIS 절연진단을 위한  
Wavelet 변환 기반의 부분방전 신호 식별

指導教授 吉 暲 碩

2019年 8月

韓國海洋大學校 大學院

電氣電子工學科

王 國 明

**Dissertation Submitted by Guoming Wang in Partial Fulfillment  
of the Degree of Doctor of Philosophy**

**Committee Chairman : D. Eng. Yoon-Sik Kim**



**Committee Member : D. Eng. Gyung-Suk Kil**



**Committee Member : D. Eng. Nak-Won Jang**



**Committee Member : D. Eng. Young-Sik Lee**



**Committee Member : D. Eng. Joong-Han Yoon**



**June 2019**

**Department of Electrical and Electronics Engineering  
Graduate School of Korea Maritime and Ocean University**

**Guoming Wang**

# Contents

<b>Contents</b> .....	<b>i</b>
<b>Lists of Figures and Tables</b> .....	<b>iii</b>
<b>Abstract</b> .....	<b>vi</b>
<b>Chapter 1 Introduction</b> .....	<b>1</b>
1.1 Research Background .....	1
1.2 Dissertation Outline .....	5
<b>Chapter 2 Partial Discharge Review</b> .....	<b>7</b>
2.1 Mechanism and Recurrence .....	7
2.2 Detection and Measurement .....	12
2.3 Analysis Methods .....	23
<b>Chapter 3 Experiment and Optimization</b> .....	<b>45</b>
3.1 Experimental Setup .....	45
3.2 Optimization of Wavelet Transform .....	49

<b>Chapter 4 Discrimination of PD Sequences .....</b>	<b>66</b>
4.1 DEP-type Pulse Sequence .....	70
4.2 DOP-type Pulse Sequence .....	79
<b>Chapter 5 Conclusions .....</b>	<b>89</b>
<b>References .....</b>	<b>91</b>

## Lists of Figures and Tables

### <List of Figures>

Fig. 2.1 PD under AC voltage .....	8
Fig. 2.2 PD under DC voltage .....	10
Fig. 2.3 PD under impulse voltage .....	11
Fig. 2.4 Detection and measurement methods .....	12
Fig. 2.5 Test circuit according to IEC 60270 .....	14
Fig. 2.6 Detection circuit of AE method .....	15
Fig. 2.7 Typical AE signal .....	16
Fig. 2.8 UHF sensors .....	20
Fig. 2.9 Conversion of UHF signal magnitude into apparent charge .....	21
Fig. 2.10 Identification of faults by gas ratios .....	22
Fig. 2.11 Typical features of a PD pulse .....	24
Fig. 2.12 Typical phase-resolved partial discharge patterns .....	25
Fig. 2.13 Structure of artificial neural network .....	26
Fig. 2.14 3-phase amplitude relation diagram pattern .....	27
Fig. 2.15 PD pulse sequences .....	28
Fig. 2.16 An example of time-resolved partial discharge pattern .....	29
Fig. 2.17 Time-frequency map acquired from different insulation defects .....	31
Fig. 2.18 Waveform of mother wavelet .....	32
Fig. 2.19 Dilation and translation of mother wavelet .....	34
Fig. 2.20 Decomposition of a signal into three levels by MRA .....	35
Fig. 2.21 Responses of hard, soft, and medium thresholding function .....	40
Fig. 3.1 Experimental setup .....	46

Fig. 3.2 Typical insulation defects in GIS .....	48
Fig. 3.3 Artificial defects .....	48
Fig. 3.4 Typical single PD pulses .....	50
Fig. 3.5 Selection of mother wavelet using CC method .....	51
Fig. 3.6 Selection of mother wavelet using DTW method .....	52
Fig. 3.7 Simulated single PD pulses .....	54
Fig. 3.8 Discrimination of DEP by medium function-automatic threshold .....	59
Fig. 3.9 Discrimination of DEP by hard function-minimax threshold .....	60
Fig. 3.10 Comparison of signal energy for DEP .....	61
Fig. 3.11 Discrimination of DOP by medium function-automatic threshold .....	62
Fig. 3.12 Discrimination of DOP by hard function-SURE threshold .....	63
Fig. 3.13 Comparison of signal energy for DOP .....	64
Fig. 4.1 PD pulse sequences .....	67
Fig. 4.2 Noises in PD detection .....	68
Fig. 4.3 VI block diagram of wavelet denoising .....	69
Fig. 4.4 Discrimination of DEP-type pulse interfered by AM interference .....	71
Fig. 4.5 Elimination of AM interference in DEP-type pulse by wavelet method .....	72
Fig. 4.6 Discrimination of DEP-type pulse interfered by non-sinusoidal noise .....	74
Fig. 4.7 Elimination of non-sinusoidal noise in DEP-type pulse by wavelet method .....	75
Fig. 4.8 Discrimination of DEP-type pulse interfered by switching impulse .....	77
Fig. 4.9 Elimination of switching impulse in DEP-type pulse by wavelet method .....	78
Fig. 4.10 Discrimination of DOP-type pulse interfered by AM interference .....	80
Fig. 4.11 Elimination of AM interference in DOP-type pulse by wavelet method .....	81
Fig. 4.12 Discrimination of DOP-type pulse interfered by non-sinusoidal noise .....	83
Fig. 4.13 Elimination of non-sinusoidal noise in DOP-type pulse by wavelet method .....	84
Fig. 4.14 Discrimination of DOP-type pulse interfered by switching impulse .....	86
Fig. 4.15 Elimination of switching impulse in DOP-type pulse by wavelet method .....	87



**<List of Table>**

Table 2.1 Types of UHF antennas .....	20
Table 2.2 Overview of applying WT in discriminating PD signal under AC ..	44
Table 3.1 Parameters of single PD pulses .....	53
Table 3.2 Discrimination results of DEP .....	61
Table 3.3 Discrimination results of DOP .....	64
Table 3.4 Discrimination results of single PD pulses .....	65
Table 4.1 Results of PD signal discrimination .....	88

**Discrimination of PD Signal using Wavelet Transform  
for Insulation Diagnosis of GIS under HVDC**

*by Guoming Wang*

Department of Electrical and Electronics Engineering  
Graduate School of Korea Maritime and Ocean University  
Busan, Republic of Korea

**Abstract**

Detection and analysis of partial discharge (PD) have been regarded as the most effective method for condition monitoring and asset management of power apparatus in the heavy electric machine industry. However, PD detection sensitivity and accuracy are greatly influenced by on-site noise and interference, resulting in failures in PD severity assessment, defect identification or localization. Although denoising of PD signal under AC was well studied, related investigations under DC have not been carried out. With the rapid development of HVDC technology, it is a new challenge to eliminate noise from PD signal under DC for diagnosis of related power facilities. Therefore, this dissertation dealt with the discrimination of PD signal based on wavelet transform techniques for HVDC gas insulated structures (GIS), aiming to improve the sensitivity and accuracy of insulation diagnosis.

Experimental setup was configured to generate PD signal under DC. The HVDC source was generated by a rectifier circuit that was composed of a dry-type transformer, a high-voltage diode, and a capacitor. Four types of artificial defects, namely protrusion on conductor (POC), protrusion on enclosure (POE), free particle (FP), and crack inside spacer (CIS) were used to simulate typical insulation defects in GIS. All of them were filled with 0.5 MPa SF<sub>6</sub> and were placed inside a shielding box to reduce the external interference during PD detection.

Single PD pulses were acquired from four types of artificial defects and were used for optimizing the wavelet transform techniques in analyzing PD under DC. The correlation coefficient and dynamic time warping method were used to compare the similarity between PD pulses and various mother wavelets. It was verified that mother wavelet bior2.6 selected by dynamic time warping method was the most appropriate for analyzing PD signal under DC. A damped exponential pulse (DEP) and a damped oscillatory pulse (DOP) were simulated for selecting the optimal thresholding function and threshold. After comparing the signal-to-noise ratio (SNR), correlation coefficient ( $\gamma$ ), and change in amplitude (A%), the medium thresholding function-automatic threshold was selected as the optimal combination.

Since pulse sequences rather than single pulses are practically used for PD analysis and evaluation, the optimized wavelet transform techniques were used to discriminate PD pulse sequences detected from the artificial defects and the effectiveness was compared with a high-pass filter. From the results, discrimination of PD signal using wavelet techniques resulted in higher values of reduction in noise as well as correlated coefficient, and lower value of

change in amplitude compared with the high-pass filter. The wavelet method was verified to be effective in denoising PD pulse sequences that were interfered by background noise, amplitude modulation radio interference, non-sinusoidal noise, and switching impulse.

The wavelet transform techniques proposed in this dissertation successfully discriminated PD signal from on-site noise and interference. Results from this dissertation were expected to be applied for PD detection and analysis of HVDC GIS, by which accuracies of PD detection, risk assessment, defect identification and localization can be significantly improved.

# HVDC에서 GIS 절연진단을 위한 Wavelet 변환 기반의 부분방전 신호 식별

왕 국 명

전기전자공학부  
한국해양대학교 대학원  
부산, 대한민국

## 초록

중전기 산업에서 부분방전의 검출 및 분석 기술은 전력설비의 상태진단 및 자산관리를 위한 가장 효과적인 방법으로 간주되어 왔다. 그러나 검출의 감도 및 정확도는 현장 노이즈에 영향을 받아 위험도 평가, 결함 판별 또는 위치 추정의 오류를 유발한다. 교류전압에서 부분방전 신호의 노이즈 제거는 활발히 연구되었지만, 최근 이슈가 되고 있는 HVDC에서 관련 연구는 미흡한 실정이다. HVDC 기술이 급속히 발전되면서 관련 전력설비 진단을 위하여, HVDC에서 부분방전 신호의 노이즈를 제거할 필요가 있다. 이들 배경으로 본 논문에서는 HVDC 가스절연구조에서 절연진단의 감도 및 정확도를 향상할 목적으로 웨이블릿 변환을 이용하여 부분방전 신호를 식별하였다.

직류에서 부분방전 신호를 발생하기 위하여 실험계를 구축하였다. HVDC는 몰드변압기, 고압 다이오드 및 커패시터로 구성된 정류회로로

발생시켰다. 가스절연구조에서 발생하는 절연결함을 모의하기 위하여 도체돌출, 외함돌출, 자유입자 및 절연물 크랙 4종의 전극계를 제작하였다. 전극계는 SF<sub>6</sub> 가스를 0.5 MPa로 충전하였으며, 차폐함을 사용하여 외부 노이즈의 영향을 최소화하였다.

4종의 모의결함에서 부분방전 단일펄스를 검출하여 HVDC에서 부분방전을 분석하기 위한 웨이블릿 변환 기술을 최적화하였다. 상관계수 및 동적시간위평 방법을 이용하여 부분방전 펄스와 다양한 모웨이블릿의 유사성을 비교하였다. 결과로부터 동적시간위평 법에 의해 선정된 모웨이블릿 bior2.6이 HVDC에서 부분방전 신호 분석에 가장 적합하였다. 최적의 문턱함수 및 문턱값을 선정하기 위하여 감쇠 지수 펄스 및 감쇠 진동 펄스를 모의하였으며, 신호-잡음비, 상관계수, 크기 변화를 비교한 결과, 중간 문턱함수-자동 문턱값이 최적의 조합으로 선정되었다.

실제 부분방전 분석 및 평가 시 단일 펄스가 아닌 펄스 시퀀스가 사용되기 때문에, 최적화된 웨이블릿 변환 기술을 이용하여 모의결함으로부터 검출된 부분방전 신호를 식별하였으며, 그 효과를 고역 통과 필터와 비교하였다. 결과로부터, 부분방전 신호 식별 시 고역통과필터에 비해 웨이블릿 기술이 잡음 감소와 상관계수가 높게, 크기 변화가 낮게 나타났다. 뿐만 아니라 웨이블릿 방법은 배경 잡음, 진폭 변조 전파 장애, 비정현 잡음 및 스위칭 임펄스로 간섭된 부분방전 신호를 식별하는 데 효과적이었다.

본 논문에서 제안한 웨이블릿 변환 기술은 현장의 노이즈로부터 부분방전 신호를 성공적으로 식별하였다. 향후 HVDC에서 가스절연구조의 부분방전 검출 및 분석에 적용될 것으로 예상되며, 부분방전 검출, 위험도 평가, 결함 판별 및 위치 측정의 정확도가 향상될 수 있을 것으로 기대된다.

# Chapter 1 Introduction

## 1.1 Research Background

Failures of electrical power facilities are primarily resulted from poor insulation condition, causing serious economic, safety, and environmental issues. Condition monitoring and diagnosis are important methods to detect the insulation degradation at its early state and to ensure the reliability of power apparatuses. The diagnostic strategy for power facilities has been developed from run-to-failure, through maintenance as necessary, time-based maintenance, and condition-based maintenance, to the reliability-centered maintenance (RCM) that is advocated nowadays. The RCM strategy is a combination of the reactive, preventive, predictive, and proactive maintenance to maximize the reliability and availability of power apparatus<sup>[1-3]</sup>. The partial discharge (PD), which is a localized electrical discharge that partially bridges the insulation, causes progressive insulation deterioration and finally results in the failure of power equipment. Therefore, detection and characterization of PD on-site and on-line are important parts of RCM.

Based on the measurement of PD, insulation defects can be detected before the eventual breakdown, and therefore the reliability and availability of equipment can be significantly enhanced and the unplanned outage of power system can be decreased, making the operation intervals extend and the maintenance cost reduce. The safety of asset manager and service personnel can be also ensured owing to less risk of explosion and combustion accidents. In addition, the environmental risk such as leakage of harmful gas and greenhouse gas can be reduced<sup>[4]</sup>.

As a main indicator of electrical failure, detection, analysis, classification, and localization of PD under alternative current (AC) have been well studied<sup>[5-10]</sup>. Based on the different physical and chemical phenomena accompanying with PD, detection methods can be categorized into conventional method according to IEC 60270 and non-conventional methods, including the acoustic emission (AE), ultra-high frequency (UHF), optical detection, and dissolved gases methods. Generally, physical PD signals are analyzed in time or frequency domain, such as the single pulse, phase-resolved PD, time-resolved PD, and time-frequency method, and the dissolved gases are analyzed in terms of gas ratios. The parameters extracted from various patterns can be used for PD identification, which is realized by machine learning algorithms like the artificial neural network, fuzzy logic, and supported vector machine. In addition, PD source can be localized using the absolute and relative time of arrival of AE or UHF signal.

However, owing to the absence of phase information and the different recurrence mechanism, PD analysis methods under direct current (DC) are totally different from those under AC, although the detection methods are the same<sup>[11-13]</sup>. The pulse repetition rate and frequency under DC are much lower than those under AC<sup>[14]</sup>. As a result, parameters for PD classification are also different. Until now, PD under DC has not been studied in detail, and experience from PD under AC cannot be applied to DC directly, including the denoising method. As the high voltage direct current (HVDC) distribution and transmission systems increase rapidly all over the world, it is necessary to deal with PD under DC voltage for the purpose of risk assessment and asset management of related power facilities.



The gas insulated structures (GIS) such as switchgear and transmission line are filled with sulphur hexafluoride ( $\text{SF}_6$ ) gas and have high insulation and arc-extinguishing capability, ensuring their high reliability, compact size, and economical efficiency<sup>[15-16]</sup>. As a result, they are widely installed in space-limited locations, such as city substations, offshore plants, and electric railway systems. The gas insulated switchgear, which is composed of circuit breaker, disconnect switch, grounding switch, and other high voltage components, has been used for power transmission and distribution since 1960s. In addition, gas insulated transmission line (GIL) is regarded as a safe and flexible alternative to an overhead line. However, insulation defects generated during the manufacture, assembly, transportation, and operation are one of the primary causes of GIS failures. Owing to the large power supply capacity, these failures result in enormous economic losses and serious human injuries. Therefore, diagnostics of PD are implemented for condition monitoring of GIS to ensure their reliable operation.

PD is evaluated using apparent charge that is expressed in picocoulomb (pC). It is specified that the maximum permissible PD level for GIS should not exceed 5 pC<sup>[17]</sup>. However, when PD signals are buried in excessive noise or interference, they cannot be exactly discriminated, leading to a reduce in detection sensitivity and a failure of assessing PD severity. Furthermore, noise is a major bottleneck that influences the accuracy of defect identification and localization. In practice, the on-site noise and interference can be classified as

- ( i ) White noise from amplifier and ambient noise, which is a random signal with equal intensity at different frequencies.
- ( ii ) Discrete spectral interferences (DSI) from communication system,

frequency modulation (FM) radio, and amplitude modulation (AM) radio, whose frequency bands are 890 MHz-1.88 GHz, 88 MHz-108 MHz, and 535 kHz-1,605 kHz, respectively. The communication interference and FM radio have frequency much higher than that of PD electrical current pulse, therefore, only the AM radio interference is taken into consideration when the conventional PD detection method is used.

(iii) Periodic non-sinusoidal noise from power electronics or other periodic switching operations.

(iv) Stochastic pulse-shaped interferences from infrequent switching operation, arcing between adjacent metallic contacts, and corona emitted from high voltage equipment<sup>[18-19]</sup>.

Although great efforts have been made to suppress the noise associated with PD measurement, the existing methods have inherent limitations. The balance circuit recommended in IEC 60270 requires addition experiment devices and is not suitable for on-line application<sup>[5]</sup>. The fast Fourier transform (FFT) only analyzes signals in frequency domain. Since actual PD pulses are non-periodic, transient, and irregular, and frequencies of various noises are not easily to be determined, the FFT method has difficulty in deciding the threshold<sup>[19]</sup>. When the digital filter is implemented, there is also difficulty in determining the optimal cutoff frequency. As a result, the noises cannot be completely removed and original PD signal may be distorted<sup>[20]</sup>.

Wavelet transform (WT), which was first introduced in practical application in mid-1980s, analyzes signal in both time and frequency domain simultaneously, and has been recognized as an effective method to discriminate PD from noise. Previous works, including selection of the most

appropriate wavelet, determination of decomposition level, and selection of threshold, have been done to reject noises from PD under AC<sup>[18-22]</sup>. However, there is few related research so far dealing with PD under HVDC.

## **1.2 Dissertation Outline**

This dissertation dealt with the discrimination of PD signal based on the wavelet transform for HVDC GIS, aiming to improve the detection sensitivity and accuracy. It is organized as follows.

Chapter 2 introduced the occurrence mechanism of PD and the difference recurrence theories of PD under AC and DC. Furthermore, features of state-of-the-art PD detection methods, including conventional electrical method, and non-conventional AE, UHF, and chemical method were described. The PD analysis methods, in terms of pulse shape, phase-resolved partial discharge (PRPD), 3-phase amplitude relation diagram (3-PARD), time-resolved partial discharge (TRPD), and time-frequency (TF) map were also discussed. Finally, the methodologies of wavelet transform and multi-resolution analysis (MRA) were explained.

Chapter 3 firstly described the experiment configuration for PD detection under HVDC, and then gave the simulation of typical insulation defects in GIS, including protrusion on conductor (POC), protrusion on enclosure (POE), free particle (FP), and crack inside spacer (CIS). The optimal mother wavelet, decomposition level, thresholding function, and threshold were selected by denoising simulated and actually detected single PD pulses after comparing the signal-to-noise ratio (SNR), reduction in noise (RN), correlation coefficient ( $\gamma$ ), and change in amplitude (A%). From the results, the mother wavelet

bior2.6, medium thresholding function, automatic threshold were the optimal selection for discriminating PD signal under DC.

Chapter 4 presented the discrimination of practical PD pulse sequences detected from the fabricated electrode systems under HVDC using the optimized wavelet transform techniques, and the effectiveness of denoising was compared with a high-pass filter that had a cutoff frequency of 800 kHz. A DEP-type PD sequence and a DOP-type PD sequence were denoised from the detected signal interfered by background noise, amplitude AM radio interference, non-sinusoidal noise, and switching impulse. Results showed the superiority of wavelet transform techniques over the high-pass filter in discriminating PD pulse sequence.

Chapter 5 gave the overall conclusions and evaluations of discriminating PD signal in HVDC GIS using the optimized wavelet transform techniques proposed in this dissertation. Recommendation and expectation for future application were also discussed.

## Chapter 2 Partial Discharge Review

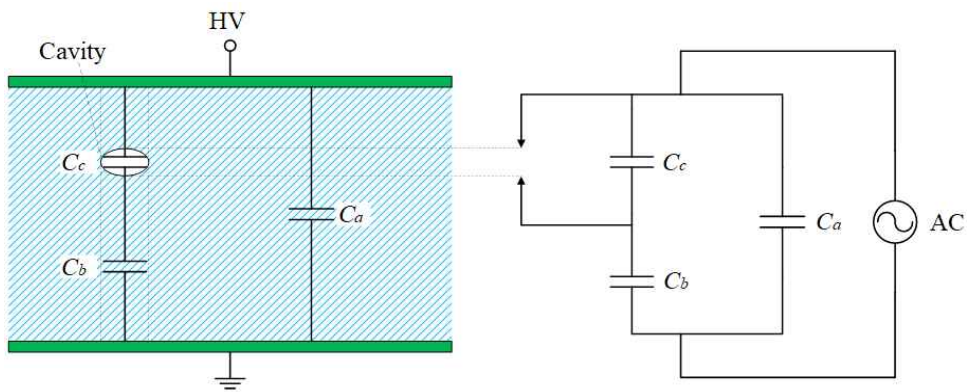
### 2.1 Mechanism and Recurrence

PD occurs when the local electrical stress is higher than the dielectric strength of insulation. Generally, PD is classified into four types: internal discharge, surface discharge, corona discharge, and discharge in electrical tree<sup>[14,23-24]</sup>. To be specific, typical insulation defects such as protrusion, moving particle, void inside spacer, and contamination are observed in the GIS, GIL, power transformer, and cable<sup>[25-27]</sup>. Although the magnitude of PD is usually small at the early stage, it causes progressive deterioration of insulation material and finally results in the failure of power facilities.

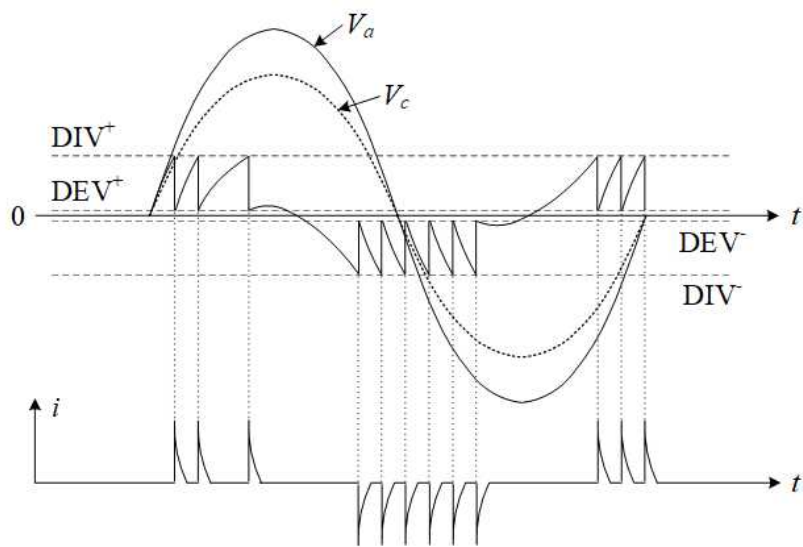
#### 2.1.1 PD under AC voltage

The equivalent circuit and recurrence of PD in a cavity of insulation material under AC voltage are shown in Fig. 2.1<sup>[14]</sup>.  $C_c$  represents the capacitance of the cavity where the discharge occurs in the insulation, the capacitance of the dielectric in series with the cavity is represented by  $C_b$  and the sound part of the dielectric is represented by capacitance  $C_a$ . When AC voltage  $V_a$  is applied to the sample and the voltage across the cavity  $V_c$  reaches the partial discharge inception voltage (DIV), a discharge occurs in the cavity. As a result of the opposite electric field induced by space charge, voltage  $V_c$  drops to a level at which the discharge extinguishes, this voltage is called partial discharge extinction voltage (DEV). A discharge finishes in the cavity and causes a current impulse. This process takes place in less than  $10^{-7}$ s, so the current impulse appears as a vertical line corresponding to the

applied voltage. As the applied voltage increases, discharge recurs when  $V_c$  reaches DIV again. The same phenomenon occurs at the negative half of the applied voltage.



(a) Equivalent circuit



(b) Recurrence of discharges

Fig. 2.1 PD under AC voltage

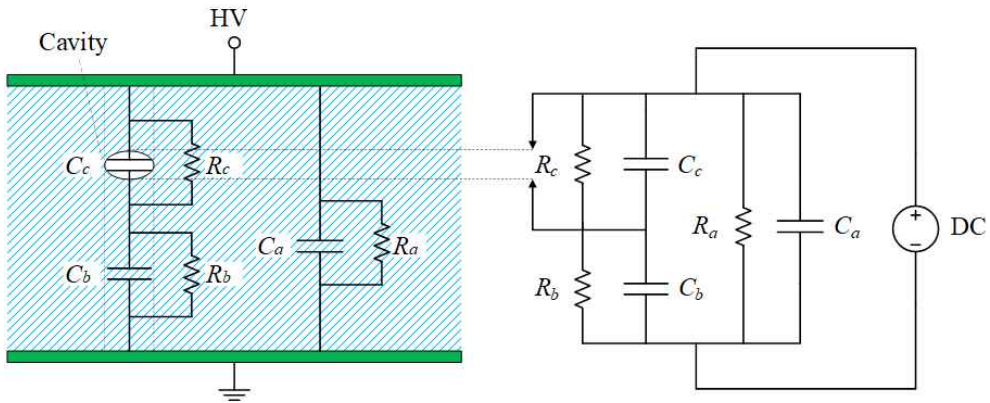
### 2.1.2 PD under DC voltage

Different from that under AC voltage, as a result of the absence of changes both in amplitude and polarity of the DC voltage, once PD occurs in the cavity, the opposite electric field induced by space charge makes PD extinguish. Discharge will recur until the induced field decreases to some degree due to the dissipation of space charge through the dielectric conductivity. In other words, the space charge disappears in the form of leakage current. Based on above consideration, the equivalent circuit for internal discharge under DC is presented by the extended circuit with some resistive elements in parallel with the corresponding capacitances, which is shown in Fig. 2.2(a).

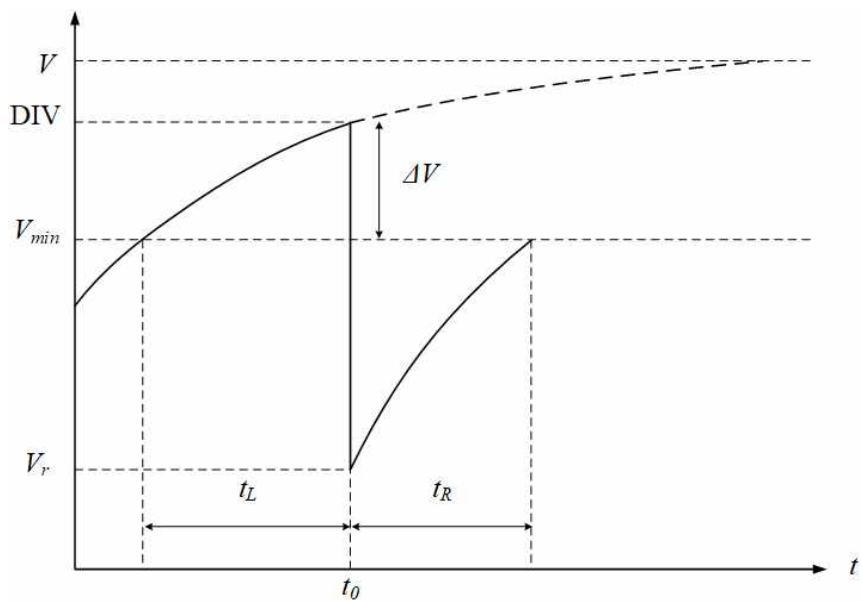
The voltage across a cavity under DC is shown in Fig. 2.2(b). For PD occurrence, two conditions must be satisfied: an initiatory electron and a sufficient electric field. The initiatory electron may come from external environment such as radiation and field emission or from previous discharge. Since the acquirement of initiatory electrons is a stochastic process, a statistical time lag  $t_L$  is needed, during which the voltage across the cavity increases from the minimum breakdown voltage  $V_{min}$  to the DIV. A discharge occurs at  $t_0$  and then drops voltage across the cavity to the residual value  $V_r$ . For recurrence of PD, a recovery time  $t_R$  is required, during which the voltage across the cavity increases from  $V_r$  to  $V_{min}$ . The time interval between two successive PD is the sum of  $t_L$  and  $t_R$ <sup>[12-13,28-29]</sup>.

The repetition rate of PD under DC voltage is much less than that under AC voltage, and it is thought that PD under DC is far less dangerous. However, with the increasing demand for HVDC application, related facilities

have been widely developed and their condition monitoring should also be carried out by investigating PD.



(a) Equivalent circuit



(b) Recurrence of discharges

Fig. 2.2 PD under DC voltage



### 2.1.3 PD under impulse voltage

Occurrence of PD under impulse voltage requires a higher voltage level compared with that under AC and DC voltage due to the low possibility to obtain an initiatory electron. PD occurrence under impulse voltage is shown in Fig. 2.3. Discharge pulse first occurs on the rising edge after the applied voltage reaches the discharge inception voltage and the starting electron is obtained. It remains energized until the crest of the impulse is reached. On the falling edge of impulse, discharges with smaller magnitudes occur in the opposite direction. PD under impulse voltage is usually tested by high-voltage impulse generator or switching impulse generator, the test levels are sufficiently high to ignite an internal discharge, surface discharge, corona discharge, or discharge in electrical tree where electric field is concentrated<sup>[14]</sup>.

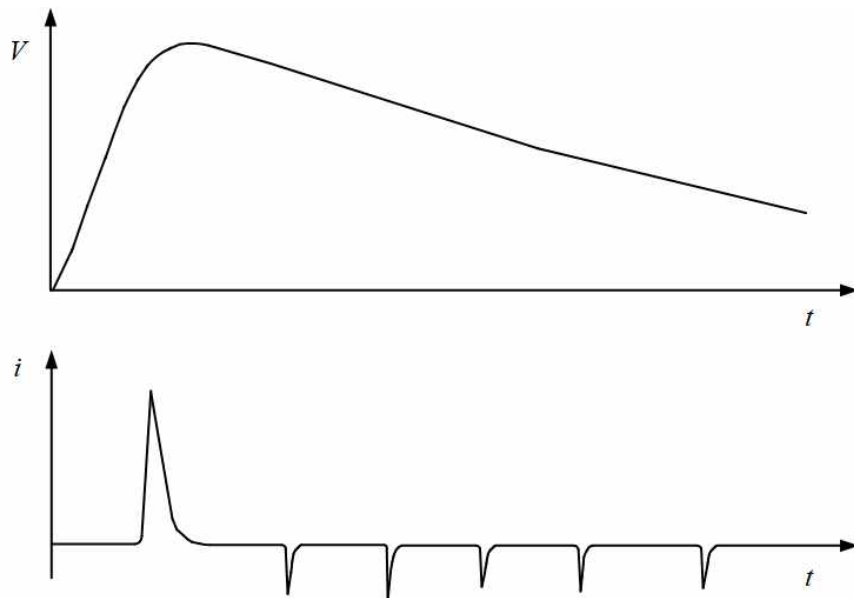


Fig. 2.3 PD under impulse voltage

## 2.2. Detection and Measurement

When PD occurs, it accompanies with various physical and chemical phenomena, based on which detection methods can be applied. Despite of different recurrence mechanisms under AC, DC, and impulse voltage, PD detection methods are the same. As shown in Fig. 2.4, PD detection and measurement methods can be classified into the conventional methods according to IEC 60270 and the non-conventional methods that mainly include acoustic emission (AE), electromagnetic transient, and chemical decomposition. In this section, PD detection mechanisms, features, applications, advantages, and disadvantages are introduced.

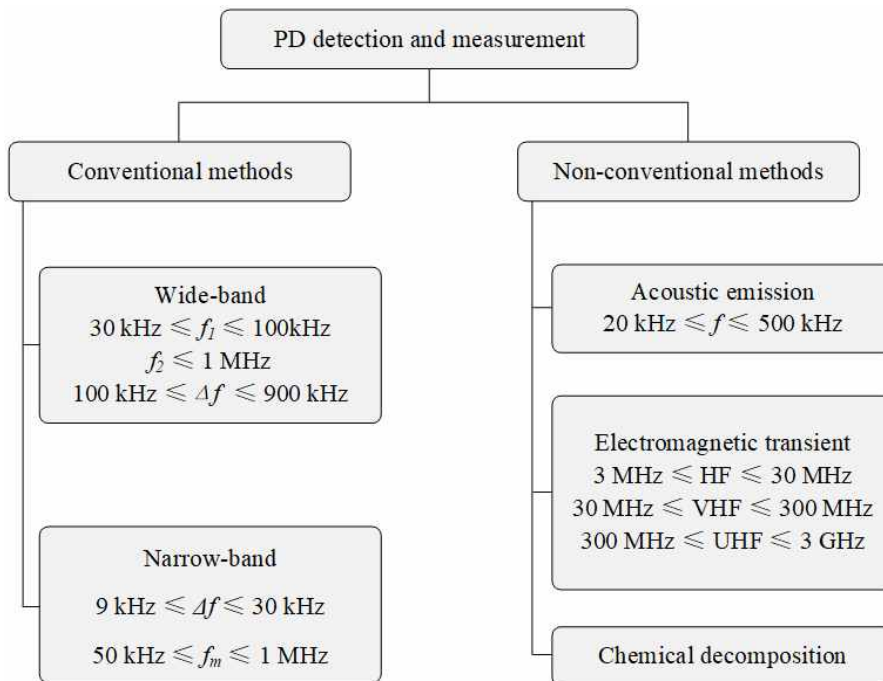


Fig. 2.4 Detection and measurement methods

### 2.2.1 Conventional methods

The conventional methods standardized in IEC 60270 detect PD current pulse using a coupling capacitor based on the series, parallel, or balanced circuit<sup>[5]</sup>. The coupling capacitor is intended to close the measuring circuit by transferring the high frequency PD pulse to the coupling device. Simultaneously the test voltage is attenuated to a harmless magnitude<sup>[30-31]</sup>. The measuring instruments are classified as wide-band and narrow-band instrument. The lower limit frequency  $f_1$ , upper limit frequency  $f_2$ , and bandwidth  $\Delta f = f_2 - f_1$  of wide-band instrument, as well as bandwidth  $\Delta f$  and midband frequency  $f_m$  of narrow-band instrument are given in Equation 2.1 and Equation 2.2, respectively.

$$30 \text{ kHz} \leq f_1 \leq 100 \text{ kHz} \quad (2.1.1)$$

$$f_2 \leq 1 \text{ MHz} \quad (2.1.2)$$

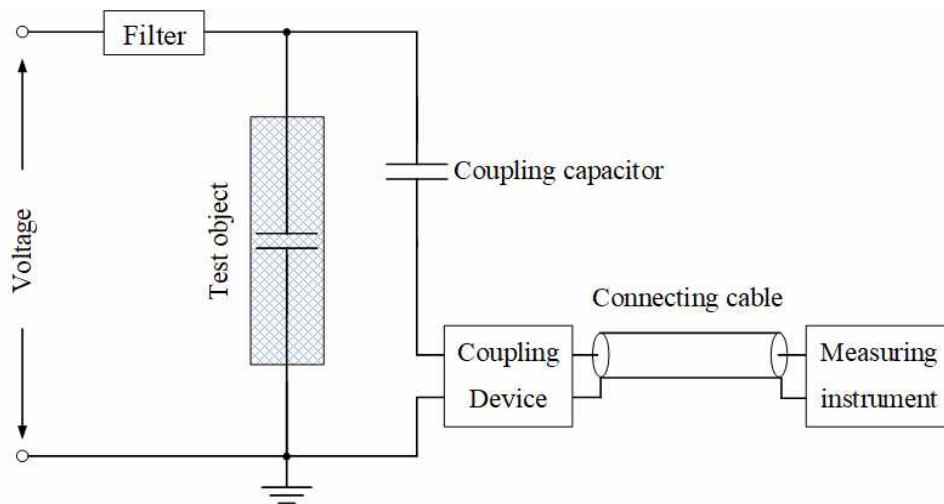
$$100 \text{ kHz} \leq \Delta f \leq 900 \text{ kHz} \quad (2.1.3)$$

$$9 \text{ kHz} \leq \Delta f \leq 30 \text{ kHz} \quad (2.2.1)$$

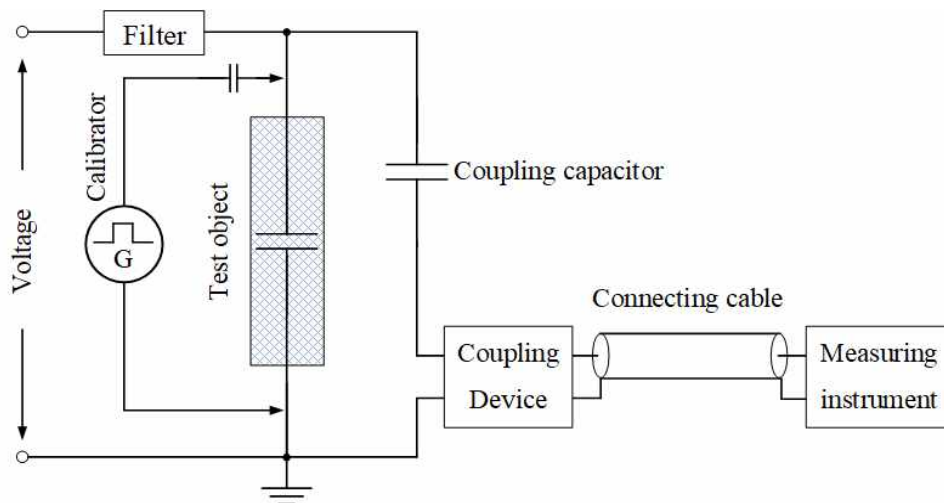
$$50 \text{ kHz} \leq f_m \leq 1 \text{ MHz} \quad (2.2.2)$$

It should be noted that the frequency requirements were revised in the third version of IEC 60270. The conventional methods are the only standardized means for quantification of PD, by measuring the apparent charge after a calibration procedure. The calibration is carried out by injecting current pulses with known charge magnitudes across the terminal of test object using a calibrator. The apparent charge is usually expressed in picocoulombs. The

basic partial discharge detection and calibration circuit according to IEC 60270 are shown in Fig 2.5.



(a) Detection



(b) Calibration

Fig. 2.5 Test circuit according to IEC 60270

### 2.2.2 Non-conventional methods

Non-conventional methods are not suitable for quantitative measurement of PD, however, they are practically implemented for on-line detection, identification, and localization of PD source.

#### 1) Acoustic emission

AE signal is generated by the rapid release of energy from PD sources within the insulation material. The acoustic wave propagates in all direction within the power facilities and the propagation is complex owing to the changes in propagation mode and velocity, reflection, and refraction<sup>[32-34]</sup>. Such signal can be detected by an AE sensor with a piezoelectric element that converts the acoustic wave into electrical signal. A typical detection circuit of AE method is shown in Fig. 2.6, which consists of a decoupler to separate acoustic signals from power source, an amplifier, and a filter.

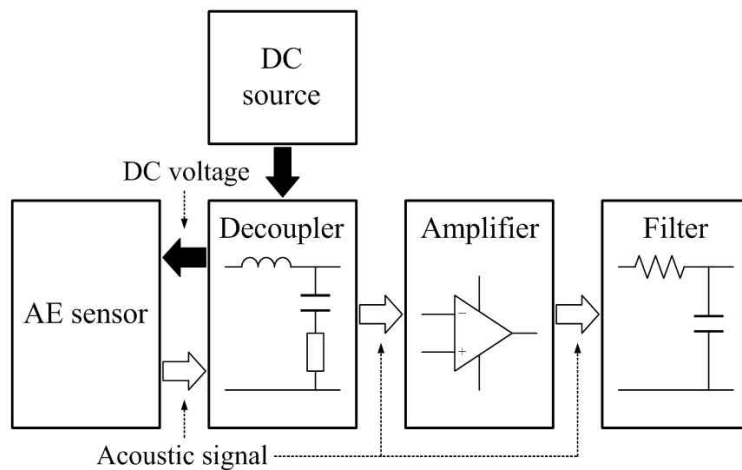
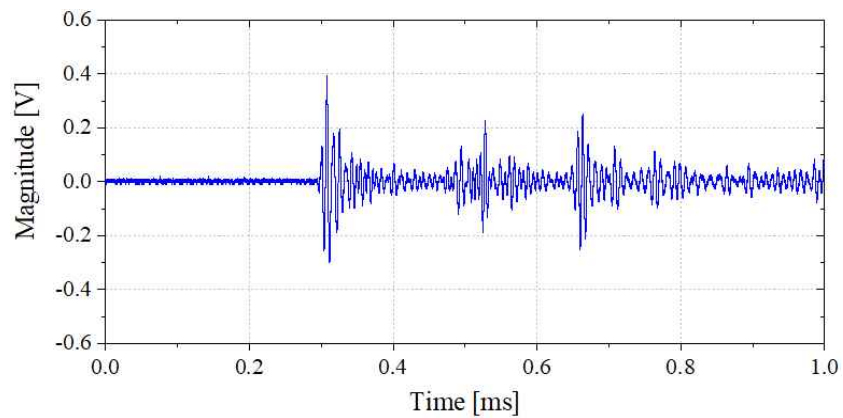
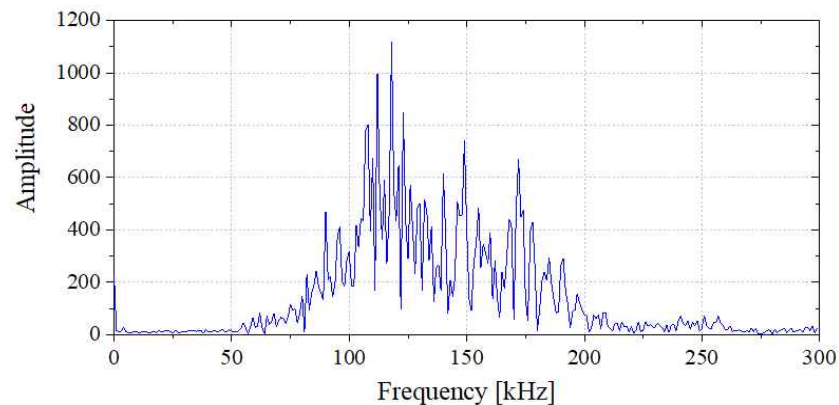


Fig. 2.6 Detection circuit of AE method

A typical AE signal in time and frequency domain is shown in Fig. 2.7. The ultrasonic AE signal is measured in frequency range of 20 kHz - 500 kHz in oil-immersed power transformer<sup>[35]</sup> and in 20 kHz - 250 kHz in GIS<sup>[36]</sup>. The AE method has advantages of low cost, easy installation, immunity to electromagnetic noise, and availability in PD localization, whereas it suffers from limitations of high attenuation and low sensitivity<sup>[10,37]</sup>.



(a) Time domain



(b) Frequency domain

Fig. 2.7 Typical AE signal

AE method is usually carried out for localizing the PD source in power transformer in the factory and in the field based on the all-acoustic system or electrical-acoustic method. The all-acoustic method localizes PD using at least four sensors based on the relative arrival times of the acoustic signals reaching each sensor, which is also called time difference of arrival method. Electrical PD signal such as the current or UHF pulse can be considered as detected synchronously with PD occurrence. Therefore, they can be used as a trigger for AE sensors. The absolute time of arrival (TOA), which means time difference between electric and acoustic signal, is the propagation time for AE signal traveling from the PD source to sensor location. Based on the TOA, localization can be realized by the following non-linear equation:

$$\begin{aligned}
 (x-x_1)^2 + (y-y_1)^2 + (z-z_1)^2 &= (vt_1)^2 \\
 (x-x_2)^2 + (y-y_2)^2 + (z-z_2)^2 &= (vt_2)^2 \\
 (x-x_3)^2 + (y-y_3)^2 + (z-z_3)^2 &= (vt_3)^2
 \end{aligned} \tag{2.3}$$

where  $(x_i, y_i, z_i)$  ( $i=1, 2, 3$ ) are the coordinates of AE sensors,  $t_i$  are time of arrival of three AE signals relative to the electrical pulse, respectively.  $v$  is the velocity of acoustic signal in insulation oil, which is 1,413 m/s at 20°C. Unknown quantity  $(x, y, z)$  is the coordinate of PD source to be calculated.

The structure-borne propagation mode of AE signal should be taken into consideration when PD localization is conducted. Generally, there are three typical propagation paths for an AE signal transmitting from the PD source

to sensors mounted on the outside of a transformer tank: direct acoustic path, reflection path in insulation oil, and structure-borne path via oil and then the tank steel. Also, the acoustic signals are classified by transverse wave and longitudinal wave according to the oscillation form. The acoustic signal propagates in insulation oil only by the form of longitudinal wave, while propagates by the forms of both transverse wave and longitudinal wave in tank steel. The velocity of transverse wave in steel is lower than that of longitudinal wave in steel but greater than that of acoustic wave in oil. In addition, attenuation of acoustic signal propagating in steel is more serious than that in oil. Therefore, the AE signal propagating in structure-borne arrives at sensor earlier with lower magnitude than propagating in direct path and thus the direct acoustic path is suggested for PD localization<sup>[32]</sup>.

The threshold method is achieved by moving the cursor over the magnitude of waves in steel to estimate TOA of acoustic signals. It is a manual method but has high precision. For accurate and automatic localization of defect, various criteria are used for determination of the TOA. The cumulative energy criterion focuses the keen on the energy curve of AE signal that eventually approaches to a constant. The energy criterion is equal to the cumulative energy subtracted by a negative trend and TOA is the minimum point on the energy curve. The Akaike information criterion estimates the TOA using the global minimum value. The cross correlation method is used to calculate the similarity between two signals. The time of maximum cross correlation value represents the TOA. By comparing these methods, it is verified that the energy criterion has the highest performance from the perspectives of precise and automatic determination of TOA<sup>[38-39]</sup>.



## 2) Electromagnetic transient

PD pulse has a short time of less than 1 ns and a pulse width of a few ns, such pulse excites electromagnetic transient that covers frequency range of high frequency (HF, 3 MHz - 30 MHz), very high frequency (30 MHz - 300 MHz), and ultra high frequency (UHF, 300 MHz - 3 GHz)<sup>[40]</sup>.

In the HF/VHF range, various sensors based on the capacitive and inductive measurement principles are used for PD detection, including the capacitive probe, transient earth voltage, high frequency current transformer, and Rogowski coils<sup>[41-43]</sup>.

The UHF method has achieved its rapid application in on-line and on-site monitoring owing to the advantages of great immunity against external disturbance, high sensitivity, and localization ability. As shown in Fig 2.8, the UHF sensor can be broadly classified into internal sensor such as drain valve sensor, and external sensor like window sensor. The sensitivity of internal sensor was confirmed to be 0.3 pC at signal-to-noise ratio (SNR) of 3 whereas that of the external sensor was confirmed to be 2 pC at SNR=3. As shown in Table 2.1, from the perspectives of sensitivity, frequency bandwidth, directivity, size, and assembly, it is confirmed that the semicircular dipole UHF sensor has the highest performance compared with the disk, monopole, logarithmic periodical, and spiral sensor<sup>[26,44]</sup>. When the UHF method is applied, the interference from video broadcasting and mobile communication, and the sensitivity verification proposed by CIGREWG15/33. 03.05 should be taken into consideration<sup>[45-46]</sup>. Since high-performance data acquisitions unit and processors are necessary to deal with the UHF signals, the related test equipment and system are more costly than other methods.



(a) Drain valve sensor

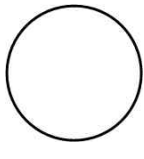
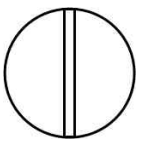





(b) Window sensor

Fig. 2.8 UHF sensors<sup>[26]</sup>

Table 2.1 Types of UHF antennas<sup>[44]</sup>

● : Excellent, ○ : Good, × : Not good

Shape					
Antenna	Disk	Semicircular dipole	Monopole	Logarithmic periodical	Spiral
Sensitivity	○	●	●	●	●
Frequency bandwidth	●	●	×	●	●
Directivity	●	○	○	○	○
Size(small)	○	○	○	×	×
Assembly	●	●	×	×	×
Evaluation	○	●	×	×	×

The magnitude of UHF signal is usually expressed in dBm. The conversion of UHF signal magnitude into the apparent charge has been studied for on-site and on-line quantitative evaluation of PD using UHF sensors. Conversion experiment is carried out by simultaneously measuring the UHF pulse and the PD current pulse and by matching the magnitudes. The results are shown in Fig. 2.9. It can be seen that relationships between the magnitude of UHF signal and the amplitude of apparent discharge follow a single curve<sup>[3]</sup>. However, these results are seriously influenced by the complicated propagation path of UHF signal from the PD site to the sensor, including reflection, refraction, and diffraction. Such drawbacks can be resolved by locating the PD source first and then compensating the attenuation factor of magnitude of UHF signal.

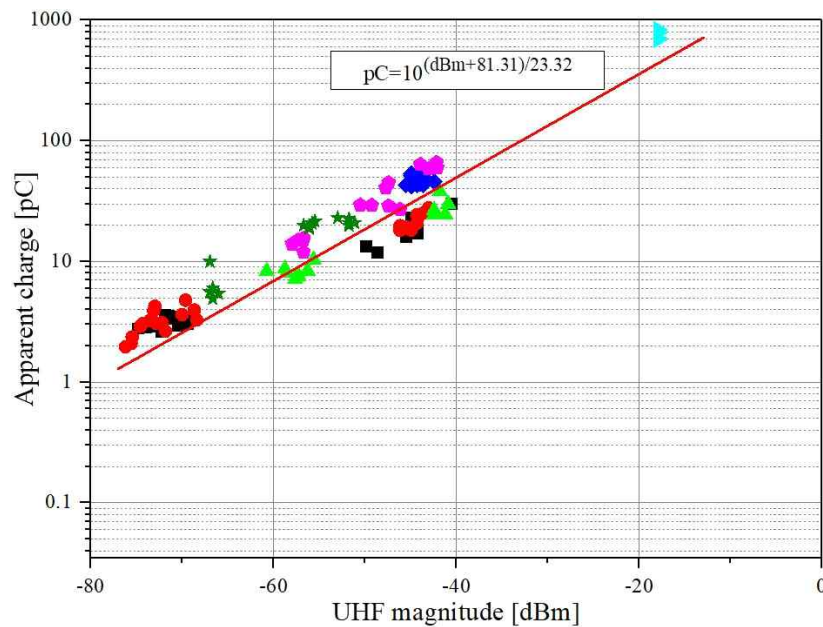


Fig. 2.9 Conversion of UHF signal magnitude into apparent charge

### 3) Chemical decomposition

Discharge causes decomposition of insulation material in the oil or gas insulated power apparatus owing to the released high energy, chemical detection methods are based on the analysis of the decomposition products. In the oil-immersed transformer, the dissolved gas analysis method specified by IEC 60599 and IEEE C57.104 analyzes the ratios of  $C_2H_2/C_2H_4$ ,  $CH_4/H_2$ , and  $C_2H_4/C_2H_6$  to identify faults such as PD, discharge of low energy (D1), discharge of high energy (D2), and thermal fault (T1 :  $T < 300^\circ C$ , T2 :  $300^\circ C < T < 300^\circ C$ , T3 :  $T > 300^\circ C$ ), as shown in Fig. 2.10<sup>[47-49]</sup>. In the GIS, concentration ratios of decomposition products of  $SF_6$  such as  $SOF_2/SO_2F_2$ ,  $CF_4/CO_2$ , and  $(SOF_2+SO_2F_2)/(CO_2+CF_4)$  are confirmed to indicate the PD energy and source type<sup>[50]</sup>.

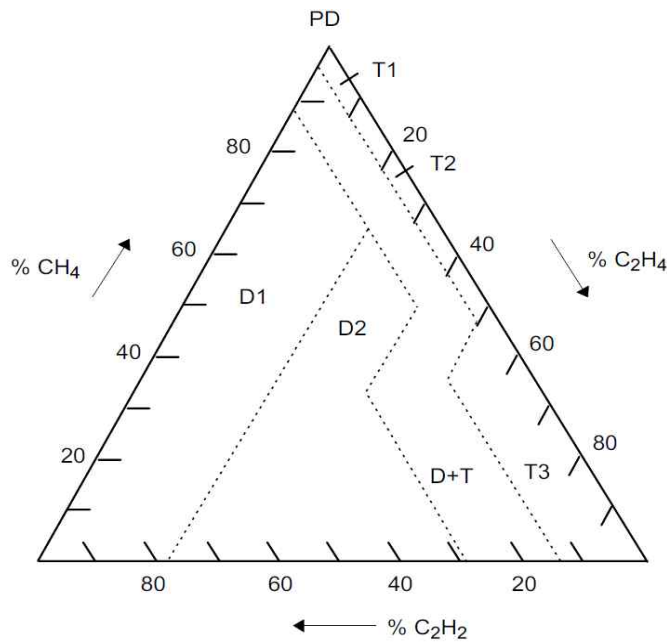


Fig. 2.10 Identification of faults by gas ratios

## 2.3 Analysis Methods

There are various of analysis methods used to evaluate the risk level of PD, to extract the discharge features for further defect classification, and to denoise PD signal, including the pulse shape, phase-resolved partial discharge (PRPD), 3-phase amplitude relation diagram (3-PARD), time-resolved partial discharge (TRPD), time-frequency (TF) map, and wavelet transform (WT).

### 1) Pulse shape

An example of PD pulse is shown in Fig. 2.11 and the features used to describe the pulse shape are given as following<sup>[10]</sup>.

Rise time ( $t_r$ ): time from 0.1 to 0.9 times of peak value at the rising side

Decay time ( $t_d$ ): time from 0.9 to 0.1 times of peak value at the falling side

Pulse width ( $t_w$ ): time interval between 0.5 times of peak value at both the rising and falling sides

Kurtosis: an indicator for the steepness of a probability distribution and defined as

$$K = \sum_{i=1}^n \frac{(x_i - \mu)^4}{n \cdot \sigma^4} \quad (2.4)$$

where  $\mu$  is the mean and  $\sigma$  is the standard deviation. The normal distribution has a kurtosis value of 3. Data with kurtosis higher than 3 tend to a steep distribution while data with kurtosis lower than 3 tend to distribute evenly.

Skewness: a measure of symmetry of a distribution around the sample and defined as

$$S = \sum_{i=1}^n \frac{(x_i - \mu)^3}{n \cdot \sigma^3} \quad (2.5)$$

Negative value for the skewness indicates data are skewed left and positive value for the skewness indicates data are skewed right. Symmetric data which are called normal distribution have a skewness value of zero.

Apparent charge ( $q$ ) : used for evaluation of PD level and can be calculated by integrating the pulse

$$q = \int_{t_1}^{t_2} i(t) dt = \int_{t_1}^{t_2} \frac{v(t)}{R_m} dt \quad (2.6)$$

where  $i(t)$  is the current pulse and  $v(t)$  is voltage pulse across the detection impedance  $R_m$ .

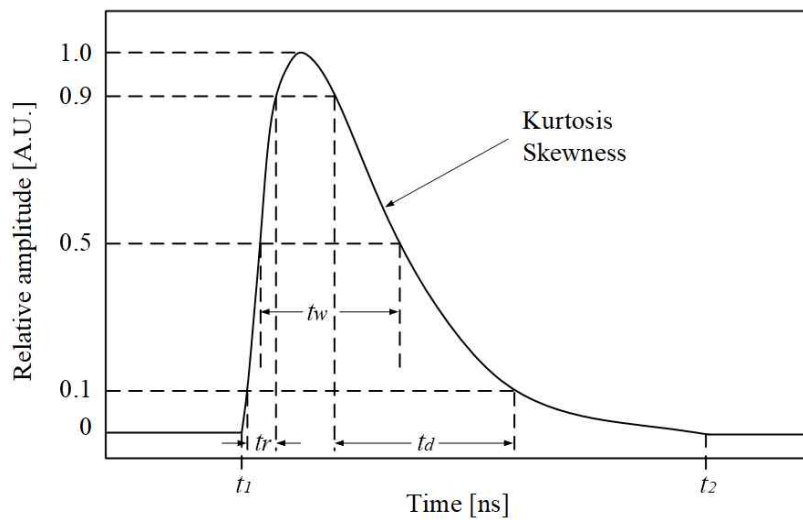
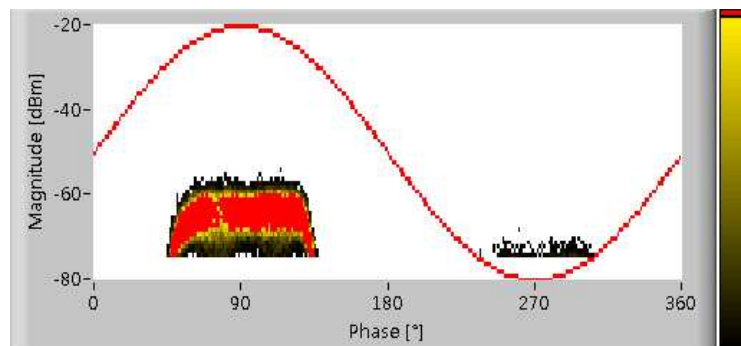


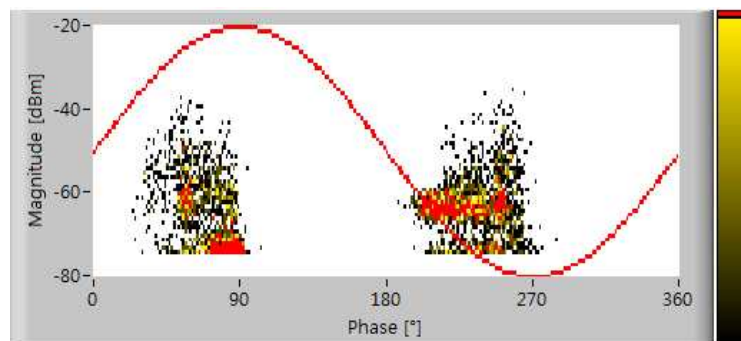
Fig. 2.11 Typical features of a PD pulse

## 2) Phase-resolved partial discharge

The PRPD method is a mostly used method for analysis of PD and for identification of defect type. It is an accumulation of the PD data under AC, including the phase on which discharge occurs, discharge magnitude, and number of discharge. The PD data can be acquired by the electrical or UHF method. Fig. 2.12 shows typical PRPD patterns in the protrusion on conductor and void inside spacer defect in GIS, which are acquired using the UHF sensor<sup>[3]</sup>. This method is unavailable under DC because of the absence of phase.



(a) Protrusion on conductor



(b) Void inside spacer

Fig. 2.12 Typical phase-resolved partial discharge patterns

An effective defect identification method based on PRPD pattern is artificial neural network, which analyzes the magnitude and phase distribution of PD pulses. The neural network is comprised of an input layer, one or more hidden layer, and a output layer. A typical structure of neural network is demonstrated in Fig. 2.13. The neurons in the input layer are as many as the number of extracted parameters. The hidden layer is used to connect the neurons in the input and output layer. The number of neurons in the output layer is the same as that of the possible defects. In addition, a sigmoid function is used to determine the activation function. During the training procedure, a back propagation algorithm is applied to update the weights and biases until the allowable error is less than expected value. Then, the updated weights and biases are rewritten into the network to replace their initial values and are finally used for real-time defect identification.

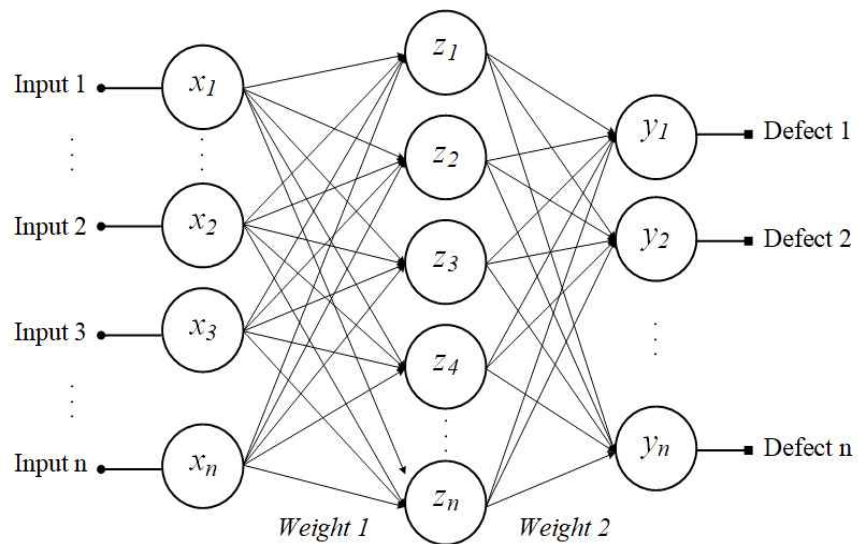
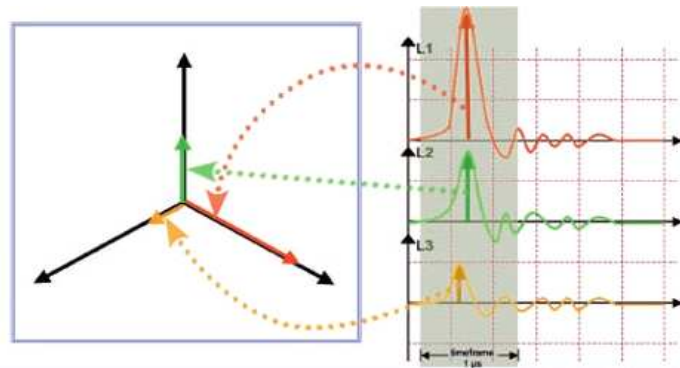


Fig. 2.13 Structure of artificial neural network

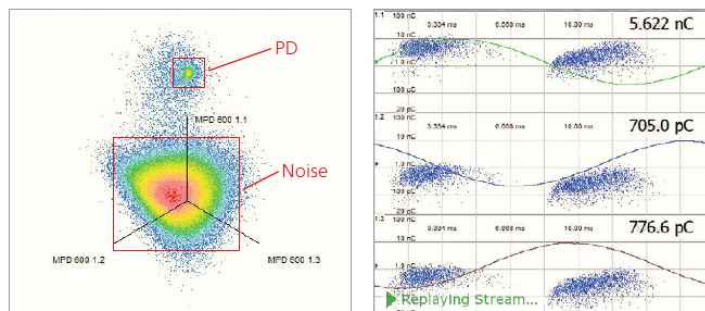


### 3) 3-phase amplitude relation diagram

The 3-PARD is used for analyzing three-phases PD by synchronous multi-channel acquisition. As shown in Fig. 2.14, 3-PARD describes the relations among amplitudes of a single PD pulse in one phase and its induced signals in the other two phases. PD signals generated from different sources and locations appear specific 3-PARD patterns and can be analyzed separately in real-time. The 3-PARD method enables noise to be clearly separated from actual PD signal as well as an easy separation of overlapped PD patterns<sup>[51-52]</sup>.



(a) Creation



(b) Separation of noise from PD

Fig. 2.14 3-phase amplitude relation diagram pattern<sup>[51]</sup>

#### 4) Time-resolved partial discharge

The TRPD method is used to investigate the statistical characteristics of pulse sequences under DC voltage. It includes two basic quantities: discharge magnitude  $q_i$  and time of discharge occurrence  $t_i$ . Fig. 2.15 demonstrates the PD sequences. The measured quantities are time-based discharge sequences  $(q_i, t_i)$ .  $\Delta t_{pre} = t_i - t_{i-1}$  and  $\Delta t_{suc} = t_{i+1} - t_i$  are the time intervals of  $q_i$  to its preceding and successive discharge, respectively. Based on the basic quantities and derived quantities, the discharge distribution and density function can be established: PD magnitude as a function of time  $q(t)$ , relation between discharge magnitude and time interval to its preceding discharge  $q(\Delta t_{pre})$ , relation between discharge magnitude and time interval to its successive discharge  $q(\Delta t_{suc})$ , density function of the discharge magnitude  $H(q)$ , and density function of the time interval  $H(\Delta t)$ . An example of TRPD pattern is shown in Fig. 2.16<sup>[11,29]</sup>.

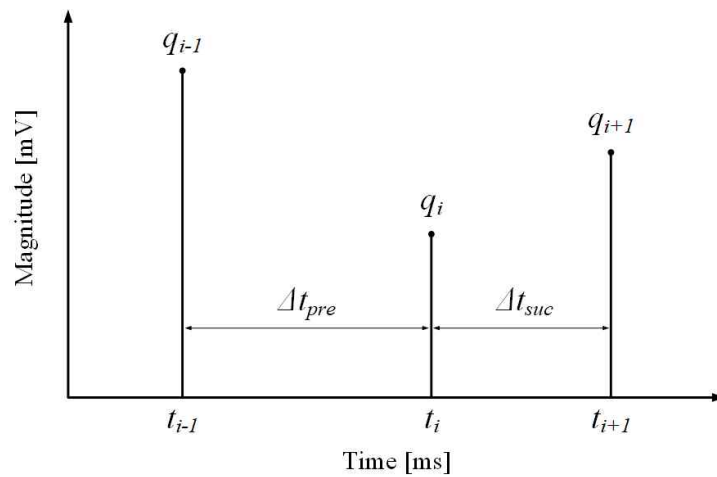
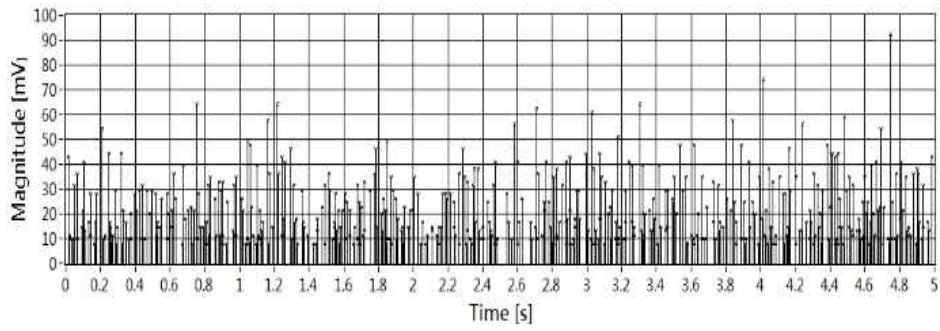
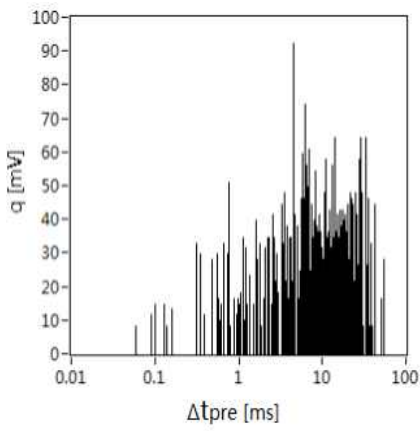


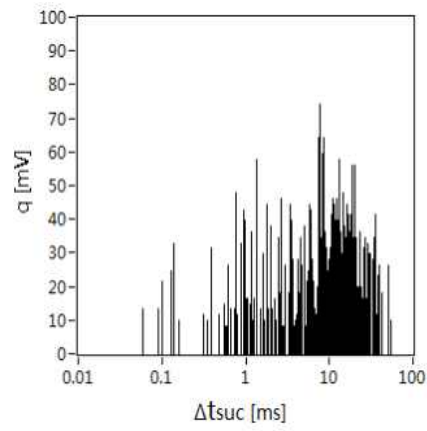
Fig. 2.15 PD pulse sequences



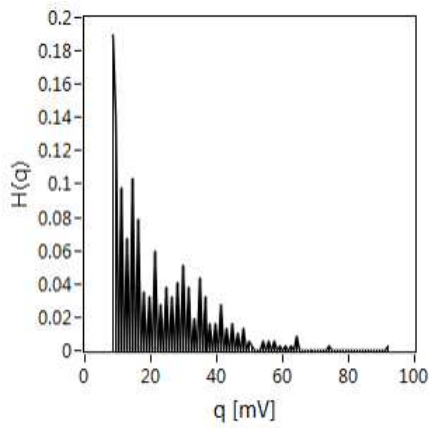
(a) PD sequences



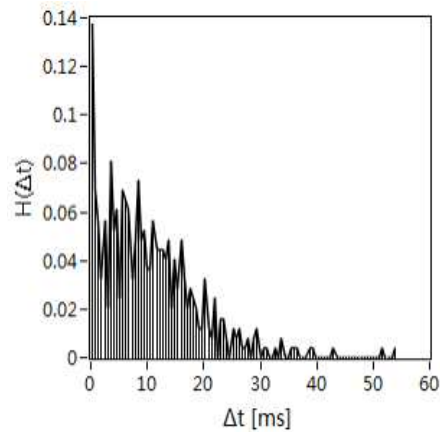
(b)  $q(\Delta t_{pre})$



(c)  $q(\Delta t_{suc})$



(d)  $H(q)$



(e)  $H(\Delta t)$

Fig. 2.16 An example of time-resolved partial discharge pattern

### 5) Time-frequency map

The TF method is an analysis of PD in time and frequency domain by extracting the equivalent time  $\sigma_T$  and the equivalent frequency  $\sigma_F$  from each PD pulse<sup>[42]</sup>. The detected signal  $s(t)$  is normalized by:

$$\tilde{s}(t) = \frac{s(t)}{\sqrt{\int_0^T s(t)^2 dt}} \quad (2.7)$$

$\sigma_T$  and  $\sigma_F$  are the standard deviations which mean the effective range of time around the time gravity and the effective range of bandwidth around the frequency gravity, respectively and are given by:

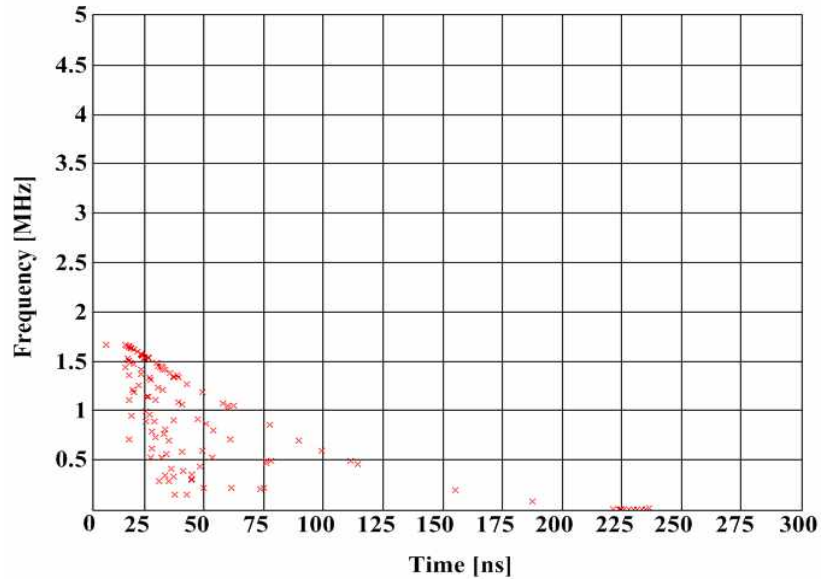
$$\sigma_T = \sqrt{\int_0^T (t-t_0)^2 \tilde{s}(t)^2 dt} \quad (2.8)$$

$$\sigma_F = \sqrt{\int_0^\infty f^2 |\tilde{S}(f)|^2 df} \quad (2.9)$$

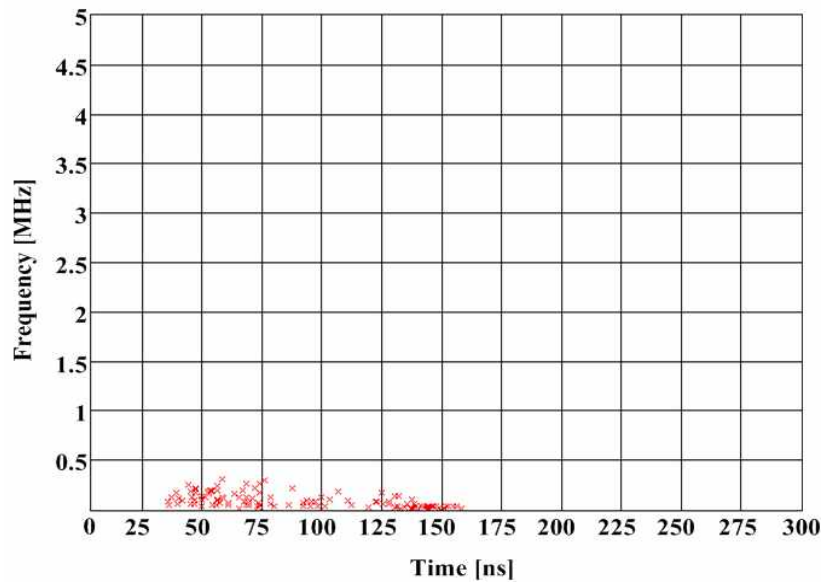
where  $\tilde{S}(f)$  is the Fourier transform of the normalized signal,  $t_0$  is the time gravity of  $\tilde{s}(t)$  and given by:

$$t_0 = \int_0^T t \tilde{s}(t)^2 dt \quad (2.10)$$

Based on the above analysis, the TF map can be established. The TF map provides method for separation of PD signal from the noise and for PD identification as shown in Fig. 2.17.



(a) Protrusion



(b) Crack

Fig. 2.17 Time-frequency map acquired from different insulation defects

## 6) Wavelet transform techniques

In this dissertation, the WT techniques are applied for discriminating PD signal under HVDC. As the Fourier transform decomposes a signal into a family of complex sinusoids, WT decomposes a signal into a family of wavelets. The family of wavelets contains the dilated and translated versions of a prototype function, which is called the mother wavelet, such as Daubechies $XX$  (db $XX$ ), Biorthogonal $XX$  (bior $XX$ ), Coiflet $XX$  (coif $XX$ ), and Symlet (sym $XX$ ) wavelet. Integer  $XX$  indicates the order of the wavelet. The higher the order, the smoother the wavelet. Examples of mother wavelet waveform are shown in Fig. 2.18.

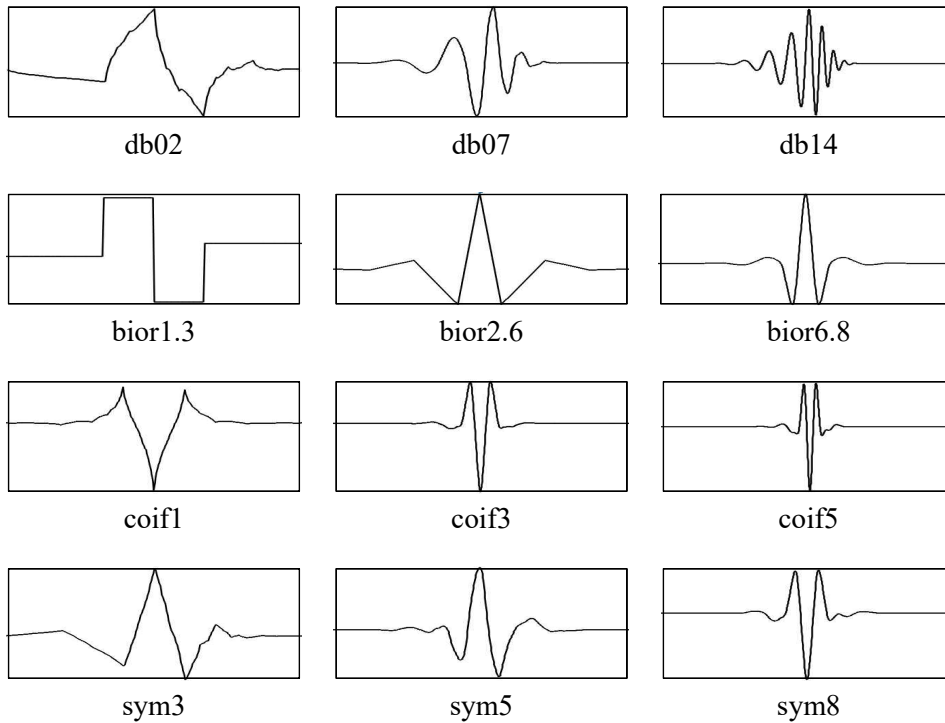


Fig. 2.18 Waveform of mother wavelet

The family of dilated and translated wavelets are given by

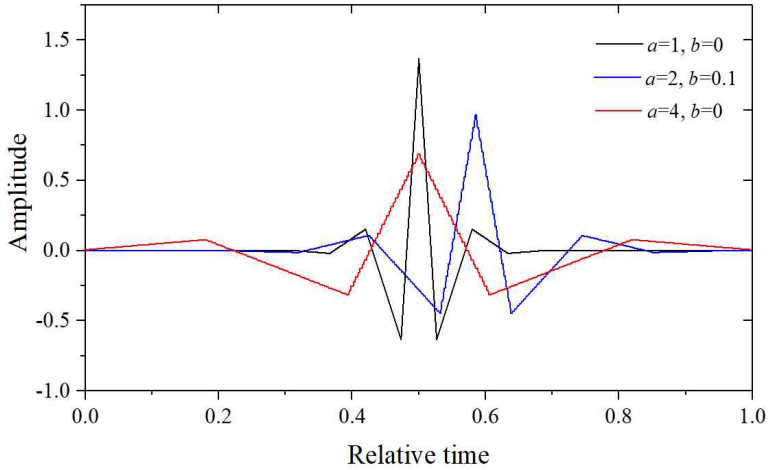
$$\Psi_{a,b} = \frac{1}{\sqrt{a}} \cdot \Psi\left(\frac{t-b}{a}\right) \quad (2.11)$$

where  $\Psi(t)$  is the mother wavelet. The scale factor  $a$  determines the amplitude and duration of the dilated wavelets to ensure that each of them has the same energy, and the shift factor  $b$  corresponds to a translation of scaled wavelet in the time domain<sup>[18-20,53]</sup>. Fig. 2.19 shows the dilated and translated wavelet with different values of  $a$  and  $b$ , and the corresponding fast Fourier transform (FFT). A wavelet with a small scale factor has a high amplitude, a short time duration, a wide frequency bandwidth, and a high central frequency, whereas a wavelet with a large scale factor has a low amplitude, a long time duration, a narrow frequency bandwidth, and a low central frequency. Therefore, a given signal can be decomposed from the time domain into a series of dilated and translated versions of a mother wavelet, thus characterizing the signal in both time and frequency domain simultaneously.

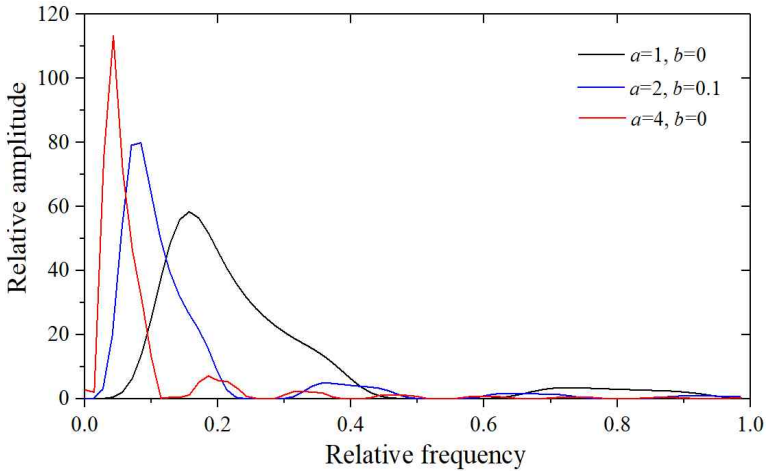
The continuous wavelet transform (CWT) of a given time-domain signal  $f(t)$  is defined as Equation 2.12. Since the CWT calculates the wavelet coefficients at every possible scale for every time instant, it is excessively redundant and computationally intensive. Furthermore, the original signal cannot be well reconstructed from the CWT coefficients<sup>[14,19]</sup>. In addition, the majority of measured signals are available as discrete-time sample. Therefore, CWT is seldom used whereas the discrete wavelet transform (DWT) is effective

in overcoming these drawbacks.

$$CWT_{\psi}f(a,b) = \frac{1}{\sqrt{|a|}} \int f(t)\Psi\left(\frac{t-b}{a}\right)dt \tag{2.12}$$



(a) In time domain



(b) Corresponding FFT

Fig. 2.19 Dilation and translation of mother wavelet



In DWT, the mother wavelet is dilated and translated discretely by selecting  $a = a_0 m$ ,  $b = nb_0 a_0^m$ , where  $m$  and  $n$  are positive integers. Therefore,

$$DWT_{\Psi} f(m,n) = \frac{1}{\sqrt{a_0^m}} \cdot \int f(t) \Psi(a_0^{-m} t - nb_0) \quad (2.13)$$

when  $a_0 = 2$  and  $b_0 = 1$ , the DWT is called a dyadic-orthonormal WT, which is actually an band filter from the perspective of signal processing. Therefore, the DWT can be obtained by using multi-resolution analysis (MRA) to decompose a given signal with different time and frequency resolutions<sup>[6,54-56]</sup>. Fig. 2.20 shows an example of the decomposition of the original signal into three levels by MRA.

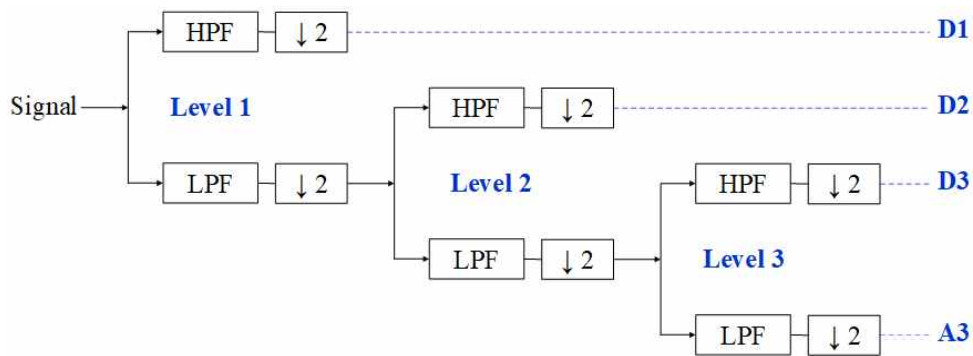


Fig. 2.20 Decomposition of a signal into three levels by MRA

In the MRA, the time-domain signal is fed through a series of high pass filters (HPF) and low pass filters (LPF) using down-sampling. The outputs of HPF and LPF define the detail coefficients (D) and approximation coefficients

(A), respectively. The approximation component is then fed through the HPF and LPF again and decomposed at the next level. The result of the MRA is a series of approximation coefficients at the maximum decomposition level and detail coefficients at every decomposition level. Filters used in MRA are called analysis filters.

The original signal can be perfectly reconstructed by inverse discrete wavelet transform (IDWT), during which signals at every level are passed through a set of synthesis filters using up-sampling<sup>[57-58]</sup>.

There are three steps for wavelet denoising.

1. Select a mother wavelet, a level  $J$ , and compute the wavelet decomposition coefficients of a given signal from level 1 to  $J$ .

As to the mother wavelet, the linear relationship between phase and frequency is expected to ensure that the time delay due to frequency is constant, which in turn ensures that the signal will not be distorted during decomposition or overlapped after reconstruction<sup>[21,59]</sup>. The correlation coefficient  $\gamma$  can be used to evaluate the similarity between the PD signal and the wavelet function. It is defined as

$$r = \frac{\sum_{i=0}^{N-1} [X(i) - \bar{X}][Y(i) - \bar{Y}]}{\sqrt{\sum_{i=0}^{N-1} [X(i) - \bar{X}]^2 \sum_{i=0}^{N-1} [Y(i) - \bar{Y}]^2}} \quad (2.14)$$

where  $X(i)$  and  $Y(i)$  represent the PD signal and the wavelet function, respectively, and  $\bar{X}$  and  $\bar{Y}$  are their average values. The value of  $\gamma$  is

between 0 and 1. The larger the value of  $\gamma$ , the greater the similarity between the two signals. Therefore, the optimal wavelet for a PD signal is the one that has the maximum value of  $\gamma$ . As defined in Equation 2.14, two signals should have the same length. However, this is hard to achieve since PD signal is usually acquired with a higher record length compared with the wavelet. Therefore, they must be normalized by resampling and shifting as the following procedures before correlation coefficient calculation<sup>[58]</sup>.

- a. Normalize the peak magnitudes of PD signal  $X(i)$  and mother wavelet function  $Y(i)$  as 1.
- b. Calculate the signal lengths of  $X(i)$  and  $Y(i)$ , which can be assumed to be  $m$  and  $n$ , respectively.
- c. Resample the length of  $Y(i)$  with a sampling interval of  $m/n$  so that two signals have the same length.
- d. Detect the peak times of  $X(i)$  and  $Y(i)$ , and shift  $Y(i)$  with a time difference so that their peaks are at the same time.

Other than the correlation coefficient method, another method applied for selecting wavelet is called dynamic time warping (DTW)<sup>[6,60-62]</sup>. The DTW is used for evaluating the similarity between two discrete signals with different lengths. It is widely applied in data mining and information retrieval.

Assuming there are two time-domain signals with lengths  $N$  and  $M$ ,

$$X = (x_1, x_2, \dots, x_i, \dots, x_N) \quad (2.15)$$

$$Y = (y_1, y_2, \dots, y_j, \dots, y_M) \quad (2.16)$$

Then an  $N \times M$  matrix using the square distance is given as

$$d(i, j) = (x_i - y_j)^2 \quad (2.17)$$

The warp path across the matrix defines the correspondence of  $x_i$  from  $X$  to  $y_j$  from  $Y$  and is given as

$$W = (W_1, W_2, \dots, W_k, \dots, W_K) \quad \max(N, M) \leq K \leq N + M \quad (2.18)$$

where  $K$  is the length of warp path. This path can be found by dynamic programming, which determines the contribution of neighboring cells in the matrix to the global matrix  $D(i, j)$  by

$$D(i, j) = \begin{cases} g(i-1, j) + d(i, j) \\ g(i, j-1) + d(i, j) \\ g(i-1, j-1) + 2d(i, j) \end{cases} \quad (2.19)$$

$g(i, j)$  is the cumulative distance of  $d(i, j)$ . The optimal warp path between  $X$  and  $Y$  is the one that has minimal distance among all possible warp paths, which can be described by

$$DTW(X, Y) = \min \sum_{k=1}^K w_k \quad (2.20)$$

The optimal mother wavelet always has a minimum DTW value associated

with the original PD signal. Certain criterion must be taken into consideration when the DTW is applied. The boundary condition ensures every index of two time-domain signals is used in the warp path. The monotonicity condition preserves the warp path without overlap. The step size condition limits the warp path from long jump.

For determining the decomposition level, it is difficult to distinguish the PD signal from interferences if a lower level is used<sup>[16]</sup>. However, much more time will be spent if the level of decomposition is redundant<sup>[18]</sup>. The optimal decomposition level is the one with which WT avoids time wastage and has sufficient resolution to recognize noises. The method for determining the maximum level is given by

$$J_{max} = \text{fix}(\log_2 \frac{L}{L_w^{-1}}) \quad (2.21)$$

where  $\text{fix}$  approximates the value to the largest integer no greater than the data in the parenthesis, and  $L$  and  $L_w$  are the lengths of the signal and the decomposition filter, respectively. This method ensures that the signal length at the highest level is not less than that of  $L_w$ <sup>[22,63]</sup>.

2. Apply a thresholding function  $\delta_\lambda(t)$  with a threshold  $\lambda$  to the detail coefficients at each level.

The application of thresholding function and threshold to the wavelet coefficients determines how these coefficients will be modified in order to effectively suppress the noisy component in a signal. This is conducted by

retaining the detail coefficients associated with the PD signal and discarding those related with noise. The mostly used thresholding function are the hard, soft, and medium thresholding, whose responses are shown in Fig 2.21<sup>[6,57]</sup>.

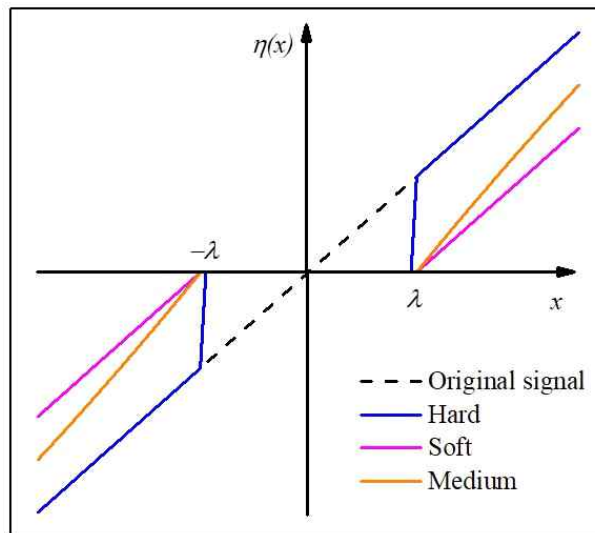


Fig. 2.21 Responses of hard, soft, and medium thresholding function

Hard thresholding function processes data in a way that wavelet coefficients whose absolute values are greater than the threshold are kept and those lower than the threshold are set to zero. The hard thresholding function is given by

$$\delta_{\lambda}^H(t) = \begin{cases} x, & \text{if } |x| > \lambda \\ 0, & \text{otherwise} \end{cases} \quad (2.22)$$

where  $x$  is the original decomposition coefficient,  $\delta_{\lambda}(t)$  is the result after thresholding, and  $\lambda$  is the threshold<sup>[35]</sup>.

Soft thresholding function sets the coefficients below  $\lambda$  to zero whereas

those greater than  $\lambda$  are retained and brought closer to zero by subtracting them from  $\lambda$ . The soft thresholding function is described as

$$\delta_{\lambda}^S(t) = \begin{cases} x - \lambda, & \text{if } x > \lambda \\ x + \lambda, & \text{if } x < -\lambda \\ 0, & \text{if } |x| \leq \lambda \end{cases} \quad (2.23)$$

Hard thresholding function is recommended for PD denoising since it provides a higher signal-to-noise ratio (SNR) after reconstruction<sup>[21,22]</sup>. However, it loses continuity at  $\lambda$ , resulting in a roughly reconstructed signal. In addition, soft thresholding function reduces the magnitude of PD pulse and therefore reduces the SNR. A medium thresholding function whose values are between the hard and soft thresholding function and provides good continuity is expressed as

$$\delta_{\lambda}^S(t) = \begin{cases} \text{sign}(x) \left( x - \frac{\lambda}{\exp[(|x| - \lambda)/\eta]} \right), & \text{if } |x| > \lambda \\ 0, & \text{if } |x| \leq \lambda \end{cases} \quad (2.24)$$

where  $\eta$  is a positive integer.

Four methods, including the automatic level-dependent threshold, Stein's unbiased risk estimate (SURE), hybrid compromising between universal and SURE, and minimax threshold are widely used as the threshold<sup>[21,64]</sup>.

The automatic level-dependent threshold  $\lambda_A$  is a modified version of the universal threshold that only estimates the noise variance using the detail coefficients at the first decomposition level. Since the detail coefficients at the first level are mainly considered as noise, the universal threshold

eliminates too much of the PD signal energy.  $\lambda_A$  estimates the noise level based on the detail coefficients at each decomposition level. It is defined as

$$\lambda_{A,j} = \frac{m_j}{q} \sqrt{2 \times \ln(n_j)} \quad (2.25)$$

where  $\lambda_{A,j}$  is the threshold at level  $j$ , and  $m_j$  and  $n_j$  are the median and the length of the detail coefficients at that level, respectively. Constant  $q$  varies between 0.4 and 1 and is usually suggested to be 0.6745<sup>[21]</sup>. Since the automatic level-dependent threshold considers the coefficient fluctuation at each decomposition level, it is more practical to suppress noise with a small elimination of the original signal.

The SURE method firstly estimates the risk for a particular threshold using the following equation

$$c(i) = \text{sort}(|x(i)|^2) \quad (2.26)$$

where  $x(i)$  is the wavelet coefficient, and  $c(i)$  is the ascending version of the wavelet coefficient. The Stein's unbiased risk  $r(i)$  for the threshold is defined as

$$r(i) = \frac{N - 2i + (N - i) \cdot c(i) + \sum_{k=1}^i c(i)}{N} \quad (2.27)$$



Suppose risk is the minimum of  $r(i_{min})$  and the threshold can be determined by

$$\lambda_{SURE} = \sqrt{c(i_{min})} \quad (2.28)$$

The hybrid threshold  $\lambda_H$  is defined as a compromise between the universal and the SURE threshold. The modified hybrid threshold is developed as a combination of the universal threshold method and the Stain's unbiased risk estimate method depending on the parameter  $\varepsilon$  and bound  $\hbar$ , which are given by

$$\varepsilon = \frac{\sum_{i=0}^N x(i)^2}{N} - 1 \quad (2.29)$$

$$\hbar = \frac{(\log_2^N)^{1.5}}{\sqrt{N}} \quad (2.30)$$

when  $\varepsilon < \hbar$ , the universal threshold is applied. When  $\varepsilon \geq \hbar$ , the Stain's unbiased risk estimate method is implemented.

The minimax threshold  $\lambda_M$  proposed by Donoho and Johnstone estimates the threshold using the minimax principle and is given as

$$\lambda_M = \begin{cases} 0.3936 + 0.1829 \ln(N-2), & N > 32 \\ 0, & N \leq 32 \end{cases} \quad (2.31)$$

3. Reconstruct signal using the modified detail coefficients from level 1 to  $J$  and the original approximation coefficients at level  $J$ .

Previous works about denoising of PD signals based on wavelet techniques were all dealt with pulses under AC, whereas related studies under DC have not been carried out. Table 2.2 shows an overview of applying WT in discriminating PD signal under AC.

Table 2.2 Overview of applying WT in discriminating PD signal under AC

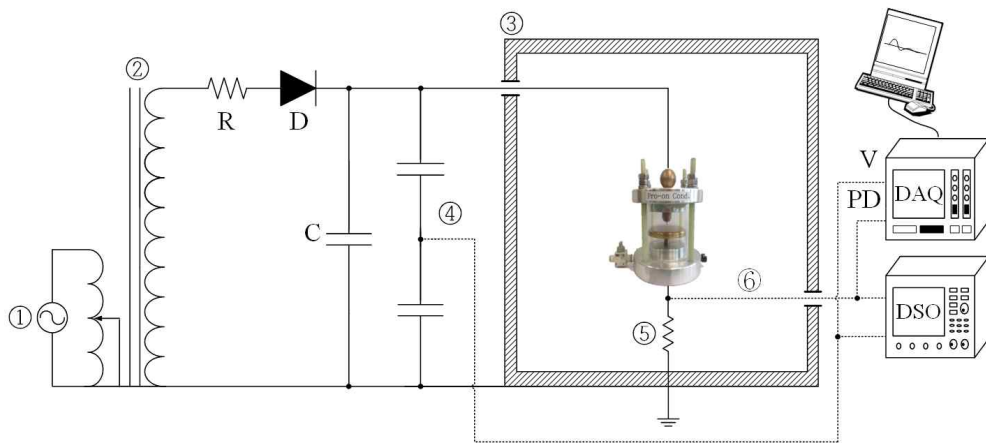
Wavelet	Level	Function	Threshold	Noise	Ref.
bior1.5	10	hard	noise based	white noise	[18]
db7 db12	10	-	-	white noise, AM periodic interference pulsive interference	[19]
db10	-	hard	automatic	white noise, corona	[21]
db7	7	hard	-	white noise, AM	[22]
db10	3	Soft	SURE	white noise, DSI	[65]

## Chapter 3 Experiment and Optimization

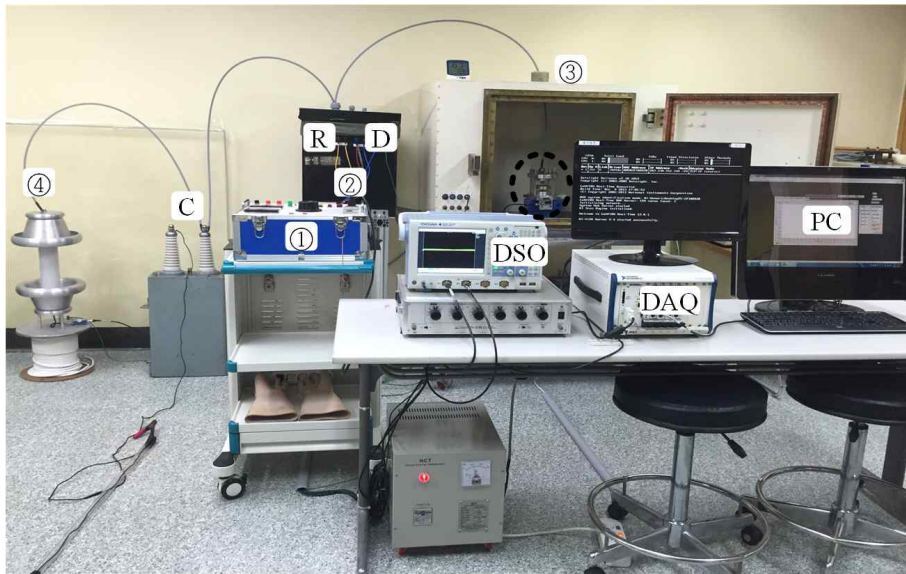
### 3.1 Experimental Setup

Configuration of experimental setup is illustrated in Fig. 3.1. A HVDC source was generated by a rectifier circuit that was composed of a dry-type transformer, a 100 kV diode, and a 0.5  $\mu$ F capacitor. The transformer with a maximum output of 50 kV and 30 mA was PD-free. It was immersed in insulation oil to ensure that there was no corona occurring adjacent to the high voltage connection. A resistor R was used in the test circuit for limiting the current that may damage the measuring instruments. Artificial defects filled with SF<sub>6</sub> gas were placed inside a shielding box to reduce the external interference. The length, width, and height of the shielding box were 1,020 mm, 720 mm, and 760 mm, respectively<sup>[3,29]</sup>.

The applied voltage was measured by a high-voltage capacitive divider (Div., North Star High Voltage, VD-100). It had a capacitance of 25 pF and a voltage ratio of 10,000:1. For accurate measurement, PD signals generated from the artificial defects were detected through a 50  $\Omega$  non-inductive resistor that was connected between the defect and the ground. A digital storage oscilloscope (DSO, Yokogawa, DL9140) with a sampling rate of 5 GS/s and a bandwidth of 1 GHz, as well as a data acquisition unit (DAQ, National Instruments, NI-5114) with a sampling rate of 250 MS/s and a bandwidth of 50 MHz were used for signal acquisition. To avoid an electric potential difference, the transformer, voltage divider, artificial defects, and measuring instruments were grounded.



(a) Circuit diagram



(b) Photograph

- |                        |                        |                 |
|------------------------|------------------------|-----------------|
| ① Voltage regulator    | ② Dry-type transformer | ③ Shielding box |
| ④ High-voltage divider | ⑤ Detection resistor   | ⑥ RG-58         |
- DSO : digital storage oscilloscope    DAQ : data acquisition unit

Fig. 3.1 Experimental setup

PD occurs at insulation defects generated during the manufacture, assembly, and transportation procedures of GIS, where the local electrical stress is higher than the insulation strength. Most of such defects can be detected in the factory test or commissioning test, whereas there are still some micro ones hard to be found. Left without checking, these defects cause progressive deterioration of the dielectric material even though facilities operate at their rated voltage. Since PD presents different patterns depending on the type of insulation defects, it is necessary to study their specific characteristics. As shown in Fig. 3.2, typical insulation defects in GIS include protrusion on conductor (POC), protrusion on enclosure (POE), free particle (FP), and crack inside spacer (CIS). In this dissertation, four artificial defects were fabricated. They were filled with 0.5 MPa SF<sub>6</sub> with a purity of 99.99%. To avoid any pollution of SF<sub>6</sub>, a vacuum pump was used to vacuumed the defects for 30 minutes before gas injection. Fig. 3.3 shows the photographs of POC and FP.

In the POC and POE, a needle electrode with a curvature radius of 5 μm and a plane electrode with a diameter of 80 mm were used. The distance between two electrodes was 3 mm. The needle electrode was used to represent a micro-size metallic protrusion on the conductor or chamber of gas insulated structures. The plane electrode was made of tungsten copper and its edge was rounded to prevent corona occurring due to the concentration of electric field. The FP, which is the most common defect, was fabricated with a 1 mm-diameter aluminum sphere to simulate a free moving metallic particle. The CIS was designed to simulate deficiency in the spacer of gas insulated structures that may result from mechanical impact. It was fabricated using an epoxy insulation plate with a diameter of 80 mm and a thickness of 5 mm.

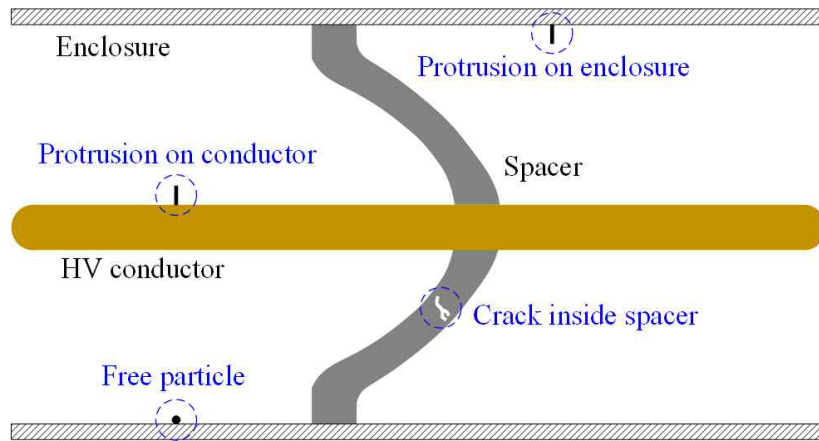
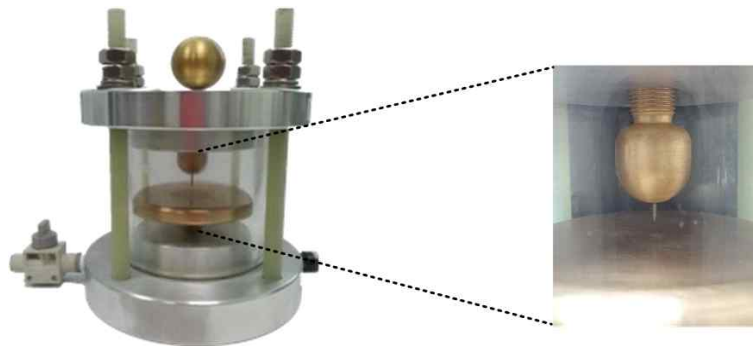
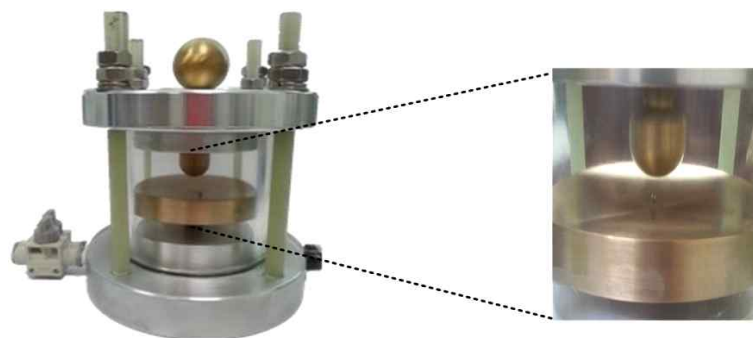


Fig. 3.2 Typical insulation defects in GIS



(a) Protrusion on conductor



(b) Free particle

Fig. 3.3 Artificial defects

## 3.2 Optimization of Wavelet Transform

### 3.2.1 Selection of the optimal mother wavelet and decomposition level $J$

50 single PD pulses were acquired from each artificial defect for selecting the optimal mother wavelet. The correlation coefficient (CC) and dynamic time warping (DTW) method were used to compare the similarity between PD pulses and various mother wavelets. The mother wavelet with the maximum CC value or the minimum warp path in DTW method is preferable for analyzing PD pulses. Typical PD pulses detected from four defects are shown in Fig. 3.4. Fig. 3.5 and Fig. 3.6 show the results of optimal mother wavelet selection using the CC and DTW method, respectively.

When CC method was used, PD pulses showed the highest similarity with wavelet bior6.8 in the POC, POE, and CIS. In the FP, the CC value of single pulse with bior2.8 was 0.65 and was 0.54 with bior6.8. Since the type of defect is unknown before the PD identification, bior6.8 was selected as the optimal wavelet for uniform analysis by the CC method. It can be seen from Fig. 3.6 that the best wavelet for analyzing PD pulses in four defects based on the DTW method was consistently bior2.6, which presented the minimal warp path with discharge pulses. The effectiveness of denoising using these two different wavelets was compared after determining the thresholding function and threshold.

The Equation 2.21 was used for determining the decomposition level. The signal length of single PD pulse was 5,000. The wavelet bior6.8 and bior2.6 have a length of 17 and 13, respectively. Therefore, the optimal decomposition level was calculated as 8 for two different types of mother wavelets.

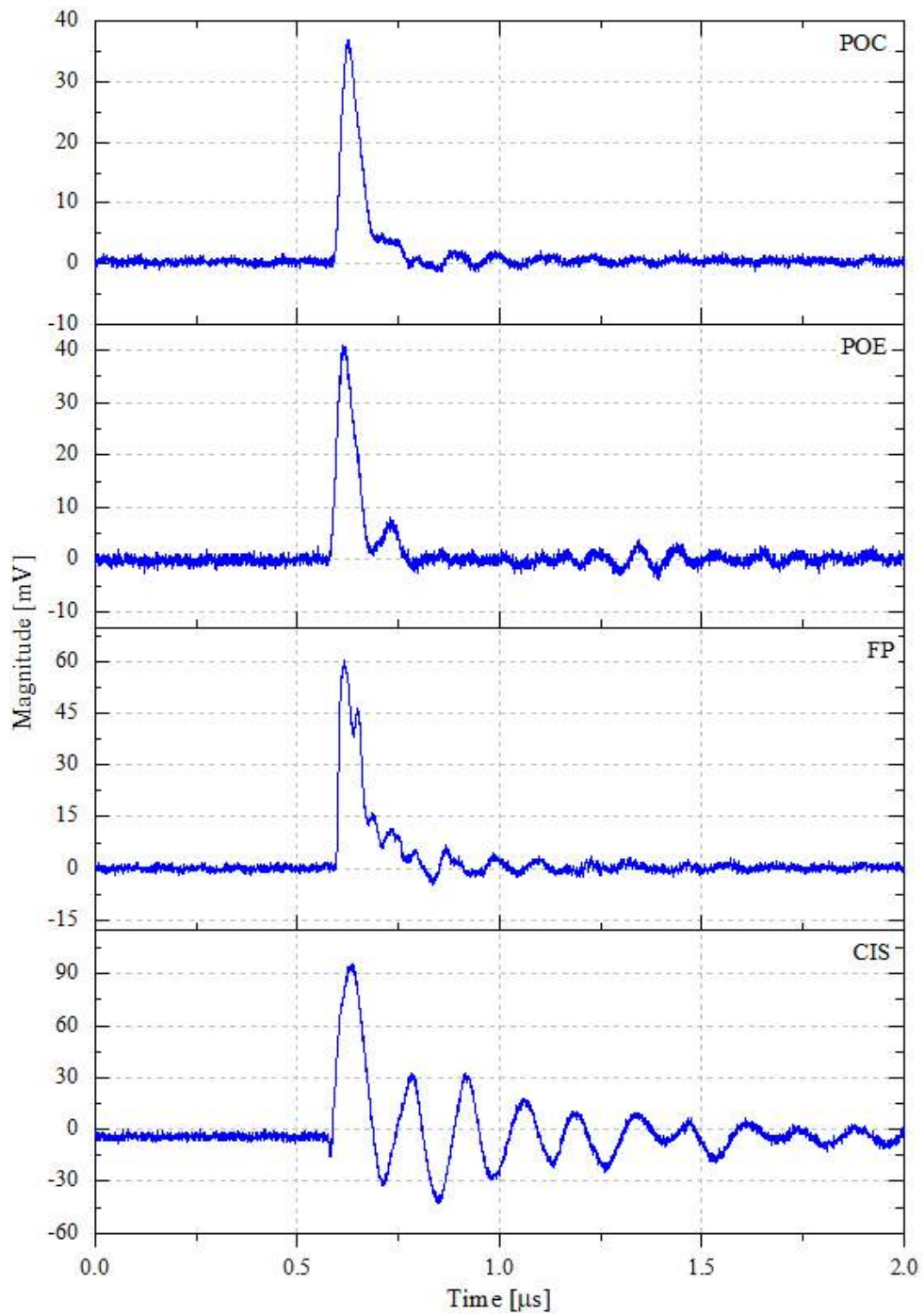


Fig. 3.4 Typical single PD pulses



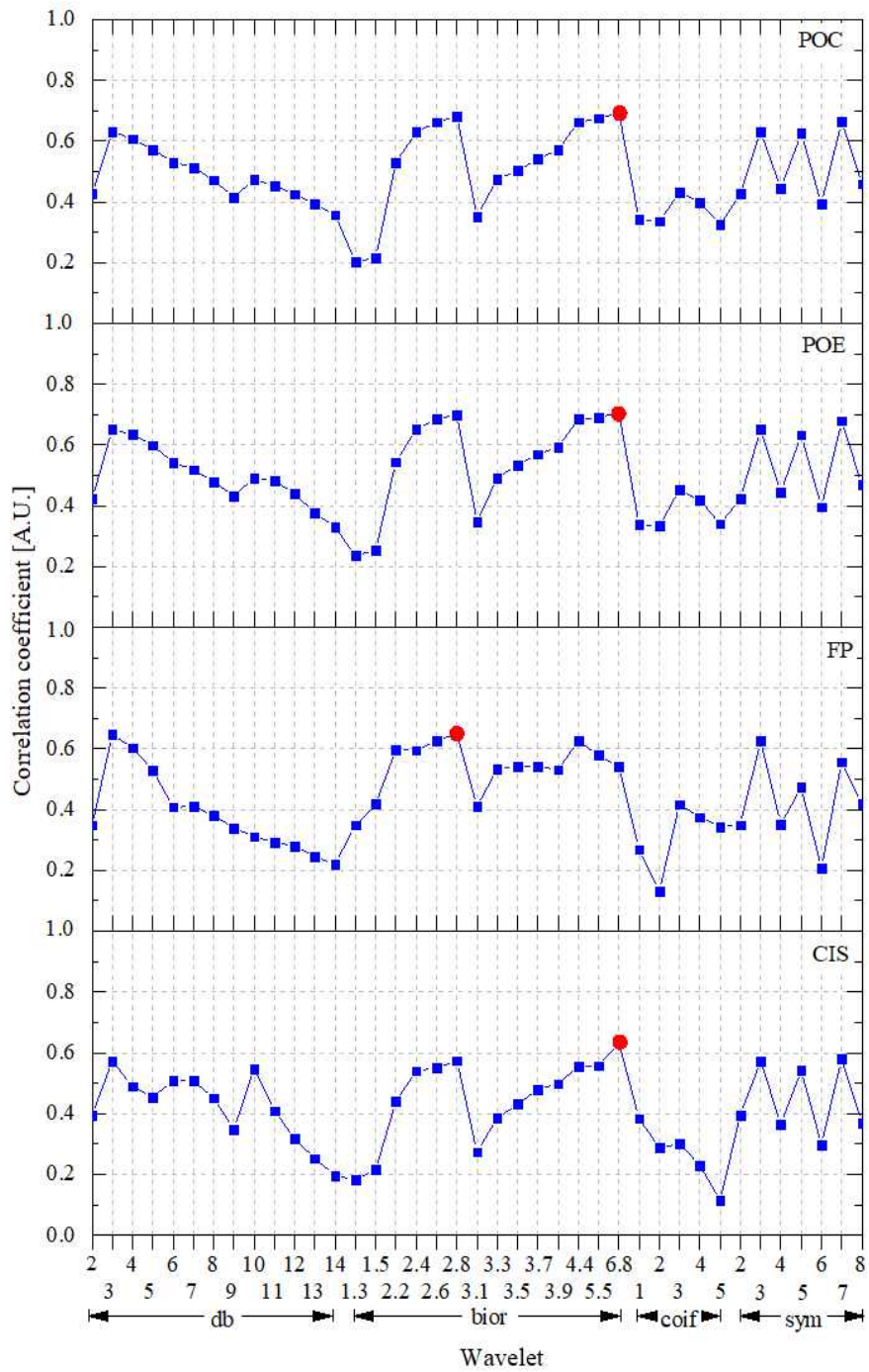


Fig. 3.5 Selection of mother wavelet using CC method

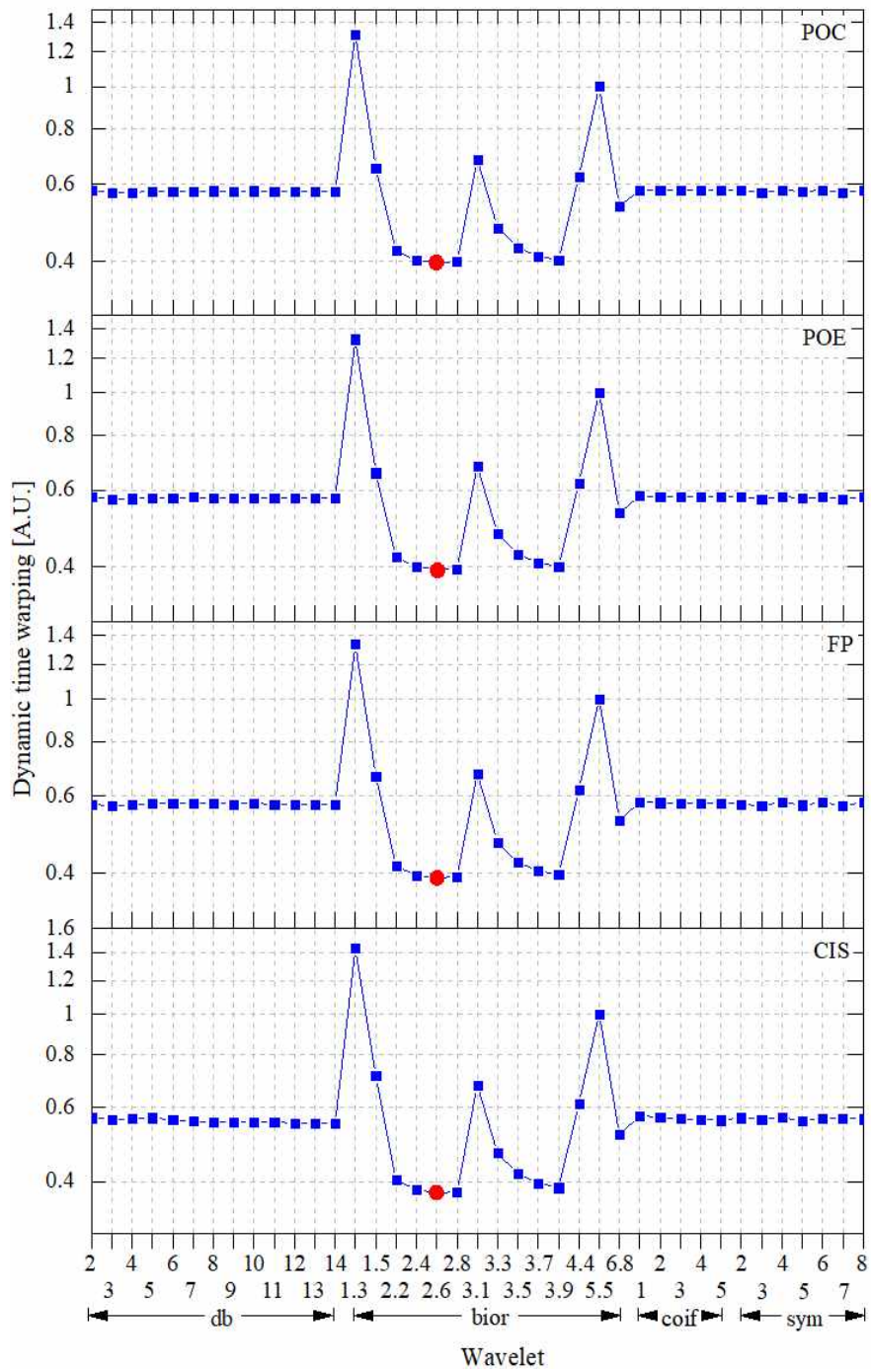


Fig. 3.6 Selection of mother wavelet using DTW method

### 3.2.2 Selection of the optimal thresholding function and threshold

The average rise time ( $t_r$ ), decay time ( $t_d$ ), and pulse width ( $t_w$ ) of single PD pulses are shown in Table 3.1. These parameters were used to determine the simulated pulse waveform for selecting the optimal thresholding function and threshold.

Table 3.1 Parameters of single PD pulses

Defect	$t_r$ [ns]	$t_d$ [ns]	$t_w$ [ns]
POC	18	45	46
POE	18	51	53
FP	11	83	58
CIS	30	35	65

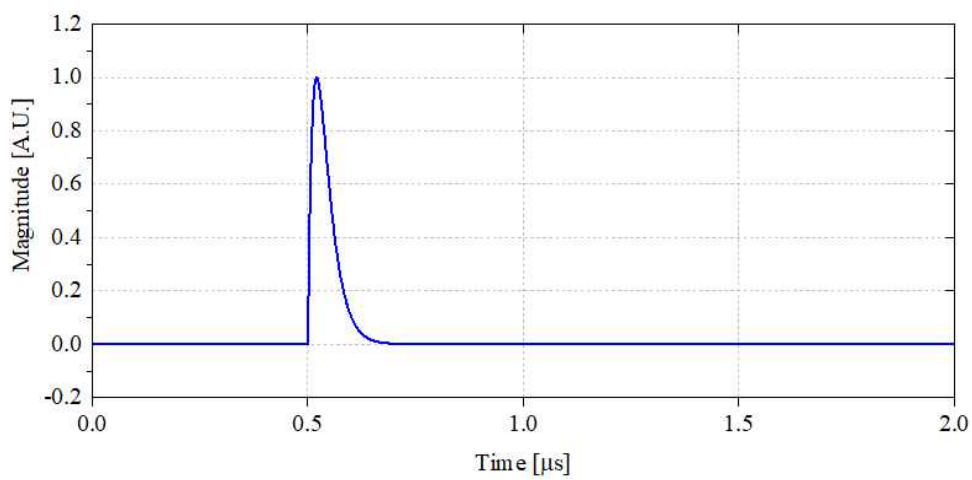
Based on the parameters of detected single PD pulses, a damped exponential pulse (DEP) was used to simulate pulses in the POC, POE as well as FP, and a damped oscillatory pulse (DOP) was used to simulate pulses in the CIS. Simulated pulses are given by

$$DEP(t) = A(e^{-t/t_1} - e^{-t/t_2}) \quad (3.1)$$

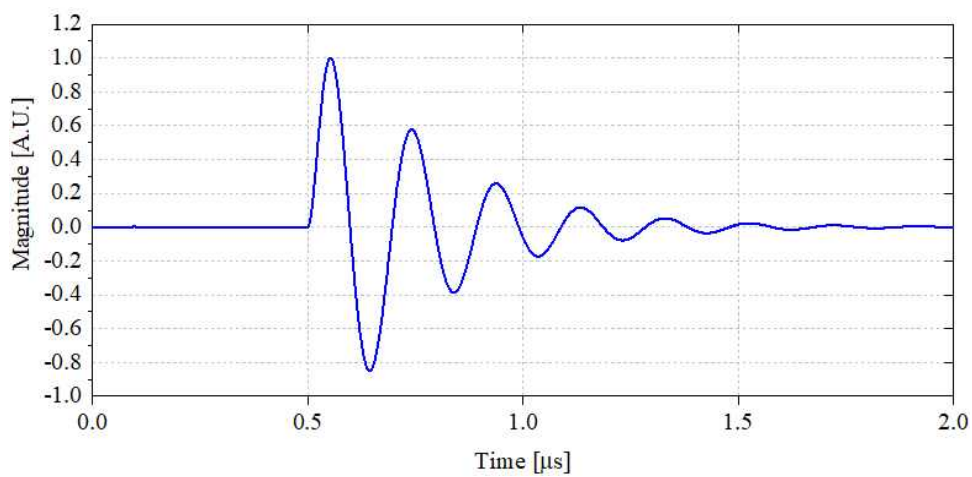
$$DOP(t) = A \sin(2\pi f_c t) (e^{-t/t_1} - e^{-t/t_2}) \quad (3.2)$$

where  $A$  is the peak value and is assumed to be 1,  $t_1$  and  $t_2$  are damping coefficients that determine the pulse waveform, and  $f_c$  is the oscillatory

frequency of DOP<sup>[18]</sup>. According to Table 3.1, the rise time, decay time, and pulse width were 15 ns, 60 ns, and 50 ns for DEP, and were 30 ns, 35 ns, and 65 ns for DOP. The lengths of two pulses were 5,000. Waveforms of simulated pulses are illustrated in Fig. 3.7.



(a) DEP



(b) DOP

Fig. 3.7 Simulated single PD pulses

These two types of simulated pulses interfered by Gaussian white noise were used to select the optimal thresholding function from hard, soft, and medium methods, and to select the optimal threshold from automatic level-dependent, SURE, hybrid, and minimax method. The noisy signals were decomposed by bior6.8 and bior2.6 wavelet into 8 levels and then denoised by various combinations of thresholding functions and thresholds. The optimization was carried out by calculating the signal-to-noise ratio (SNR), reduction in noise (RN), correlation coefficient ( $\gamma$ ), and change in amplitude (A%) between the original and denoised signal<sup>[59]</sup>.

The SNR defines the effectiveness of denoising and is given by

$$\text{SNR} = 10 \log \frac{\sum_{i=1}^N Y^2(i)}{\sum_{i=1}^N [X(i) - Y(i)]^2} \quad (3.3)$$

where  $X(i)$  and  $Y(i)$  are the simulated signal and the denoised signal, respectively.  $N$  is the signal length and  $i$  is the index number. The correlation coefficient given in Equation 2.14 indicates the similarity between two signals and therefore reflects the degree of distortion of PD pulses after denoising by different methods.

The RN and A% are defined as

$$\text{RN} = 10 \log \sum_{i=0}^N [X(i) - Y(i)]^2 \quad (3.4)$$

$$A\% = \frac{|X - Y|}{X} \times 100\% \quad (3.5)$$

where  $X$  and  $Y$  are peak values of the simulated signal and the denoised signal, respectively. After denoising by different thresholding functions and thresholds, noise should be eliminated effectively while the original signal should not be distorted. Therefore, an acceptable denoising method corresponds to the largest SNR, RN, and correlation coefficient, as well as the lowest A%.

The simulated pulses immersed in Gaussian white noise were decomposed into 8 levels by bior6.8 and bior2.6, and then denoised by a threshold and thresholding function. The same result was obtained by two mother wavelets. The sampling rate of signal acquisition was 2.5 GS/s, thus the maximum frequency of single PD pulse was 1.25 GHz. The MRA decomposed the frequency band of signal into half by down-sampling at each decomposition level, making the detail components (D) go through the high pass filter and the approximation components (A) go through the low pass filter, which is to be decomposed again at the next level. Therefore, the frequency bands of detail components ( $f_{D,N}$ ) and the frequency bands of approximation components ( $f_{A,N}$ ) at each decomposition level can be expressed by Equation 3.6 and 3.7 as following

$$\frac{1.25 \times 10^9}{2^N} < f_{D,N} \leq \frac{1.25 \times 10^9}{2^{N-1}} \quad (3.6)$$

$$0 < f_{A,N} \leq \frac{1.25 \times 10^9}{2^N} \quad (3.7)$$

where  $N$  is the decomposition level and is an integer in range of 1 - 8.

Fig. 3.8 and Fig. 3.9 show the discrimination of DEP by medium function-automatic threshold and hard function-minimax threshold combination, which were the best and the worst situation, respectively. The high-frequency noise located in detail components of D1-D5 distributed in a frequency range of 39 MHz-1.25 GHz. The PD-related components were mainly detail components D6-D8 and approximate component A8, covering the frequency up to 39 MHz. The thresholding function and threshold were only applied to process detail components whereas the approximate component was retained.

In Fig. 3.8 and Fig. 3.9, the SNR of original signal (simulated PD interfered by white noise) was -45.61 dB. When the medium function-automatic threshold was applied, the high-frequency noise components were well eliminated and the simulated signal was well reconstructed, as the red signal shown in Fig. 3.8. Denoising resulted in a SNR of 12.59 dB, which was improved by 58.20 dB. The correlation coefficient was 0.97, showing high consistency between the simulated signal and denoised signal. The A% was 0.67, which indicated that the simulated pulse was not distorted. On the contrary, when the hard function-minimax threshold was implemented, noise components were not eliminated thoroughly and the simulated pulse was still interfered. The SNR and correlation coefficient were 3.62 dB and 0.74, both of which were lower than those obtained by medium function-automatic threshold. The A% was 46.49, meaning serious distortion

of the simulated pulse.

The effectiveness of denoising was also verified by the signal energy at each decomposition level, which was calculated by

$$\text{Signal energy} = \sum_{i=0}^N x_i^2 \quad (3.8)$$

where  $x_i$  is the component at each decomposition level and  $N$  is the signal length. The comparison of signal energy is shown in Fig. 3.10. The energies of components related with noise at lower levels were reduced by hard function-minimax threshold, and were significantly reduced by medium function-automatic threshold. The results of discrimination of DEP by different combinations are shown in Table 3.2. Therefore, medium function-automatic threshold was selected.

Fig. 3.11 and Fig. 3.12 show the discrimination of DOP by medium function-automatic threshold and hard function-SURE threshold, respectively. The SNR of original signal was  $-2.08$  dB and was increased to  $17.86$  dB after applying the medium function-automatic threshold. The correlation coefficient and A% were  $0.99$  and  $8.76$ , respectively. The comparison of signal energy is shown in Fig. 3.13. And the results of discrimination of DOP by different combinations are shown in Table 3.3. Therefore, medium function -automatic threshold, which was the same as for DEP, was selected for denosing DOP.

Based on above analysis, the medium-automatic combination was selected as the optimal thresholding function and threshold.



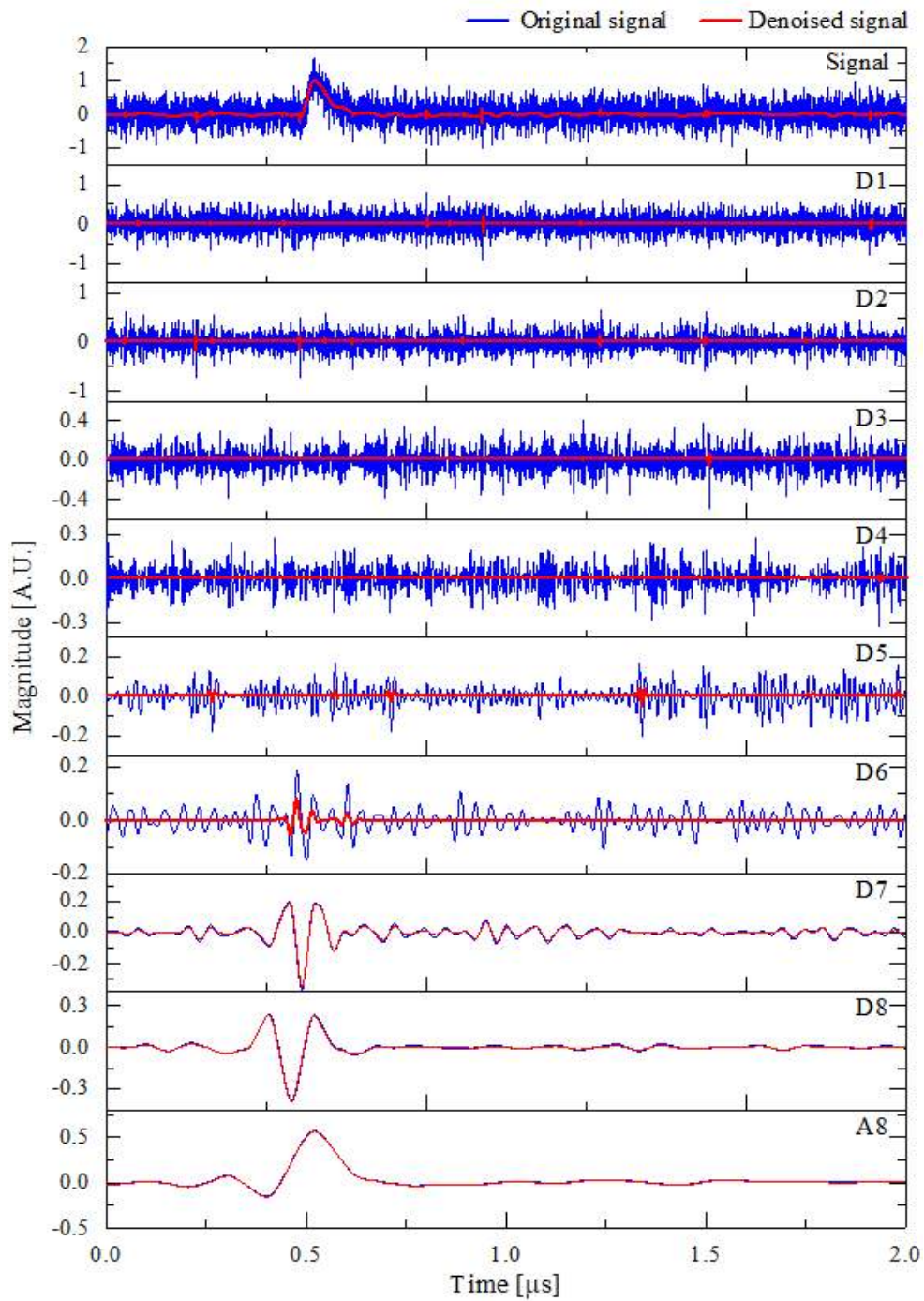


Fig. 3.8 Discrimination of DEP by medium function-automatic threshold

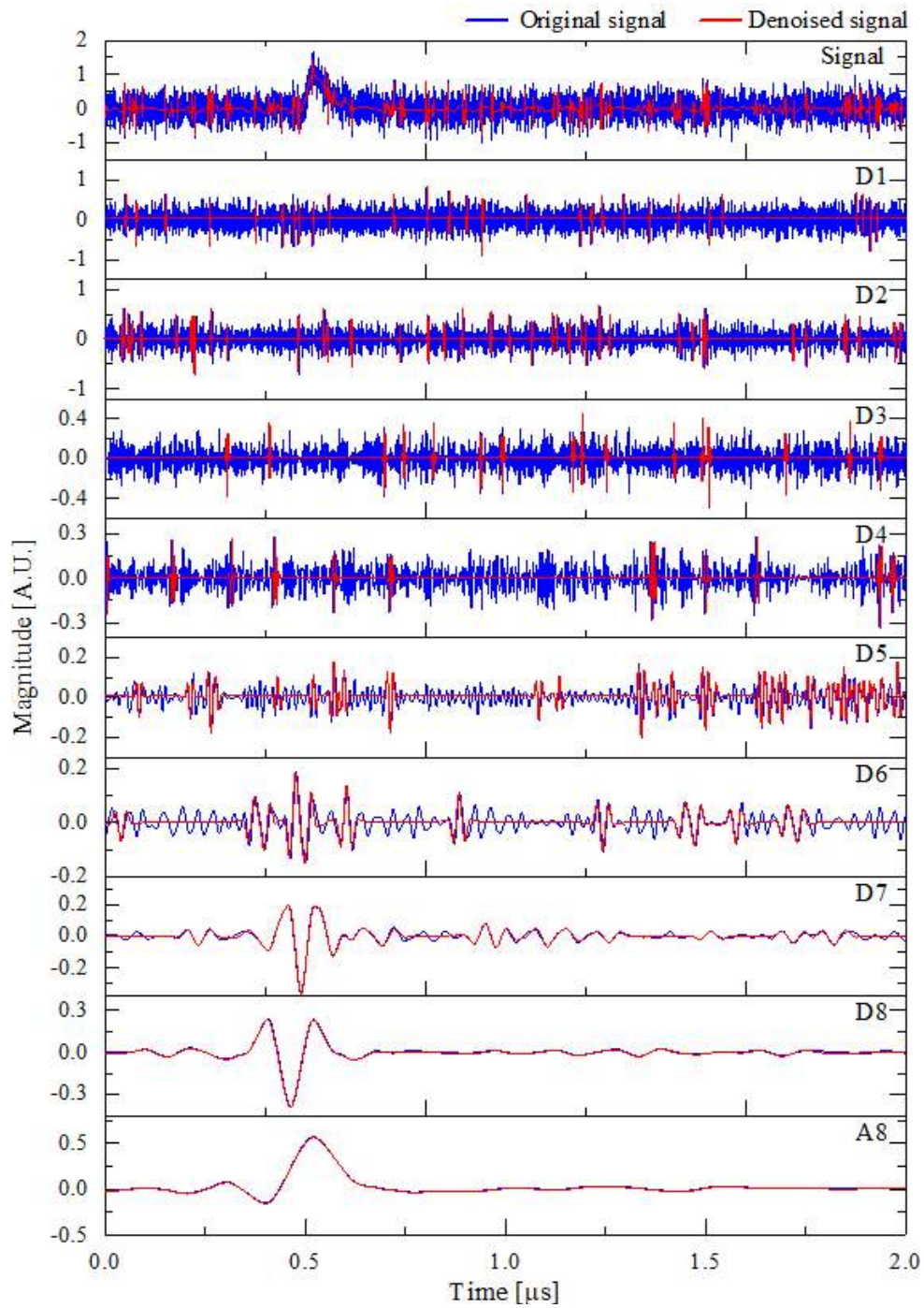


Fig. 3.9 Discrimination of DEP by hard function-minimax threshold

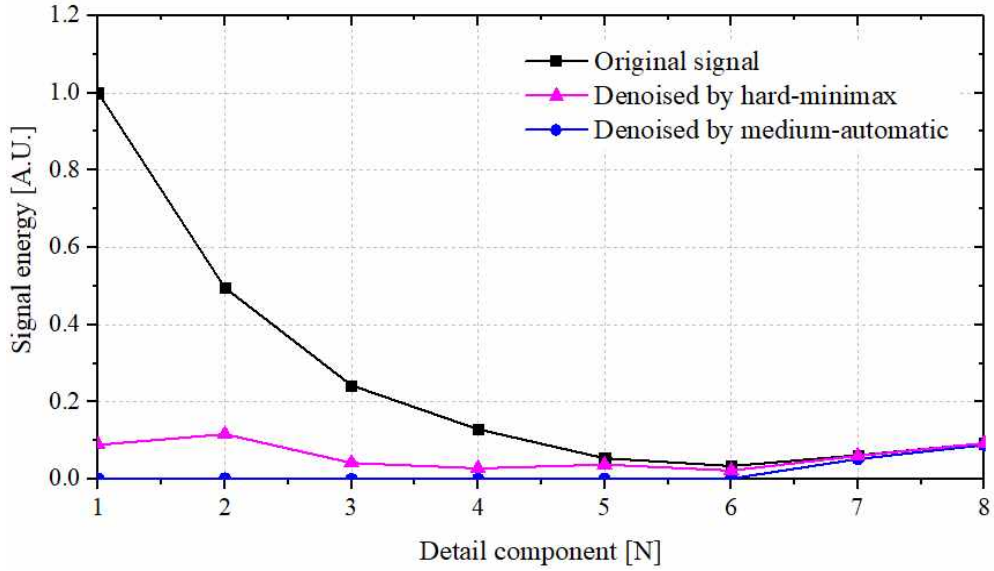


Fig. 3.10 Comparison of signal energy for DEP

Table 3.2 Discrimination results of DEP

Function	Threshold	SNR [dB]	$\gamma$	A%
Hard	Automatic	4.94	0.82	43.95
	SURE	3.40	0.73	23.95
	Hybrid	6.17	0.87	43.93
	Minimax	3.62	0.74	46.49
Soft	Automatic	10.96	0.97	4.89
	SURE	9.22	0.94	7.32
	Hybrid	9.97	0.97	3.69
	Minimax	11.89	0.97	7.09
Medium	Automatic	12.59	0.97	0.67
	SURE	8.64	0.93	8.84
	Hybrid	12.73	0.97	2.41
	Minimax	11.30	0.96	10.13

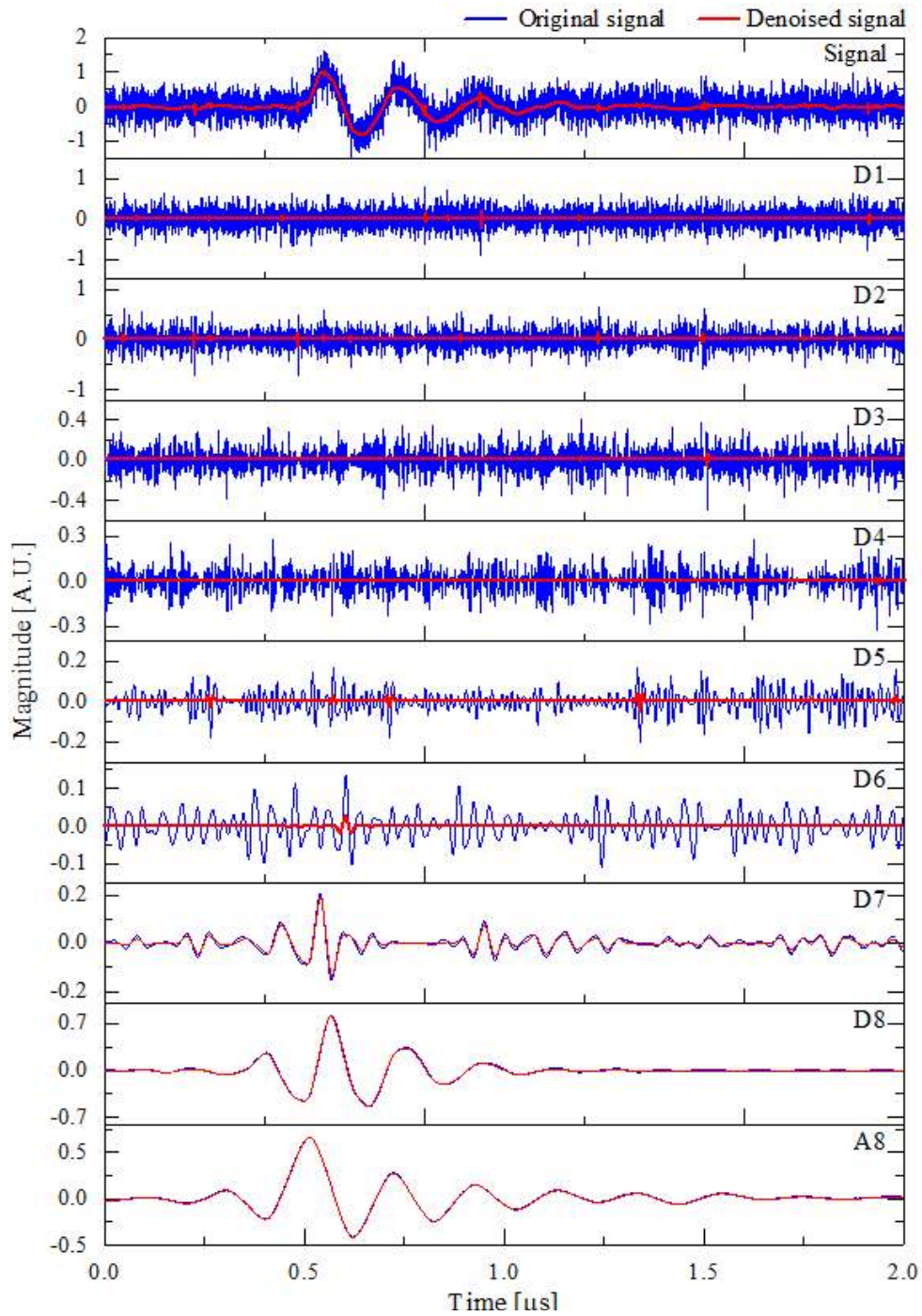


Fig. 3.11 Discrimination of DOP by medium function-automatic threshold



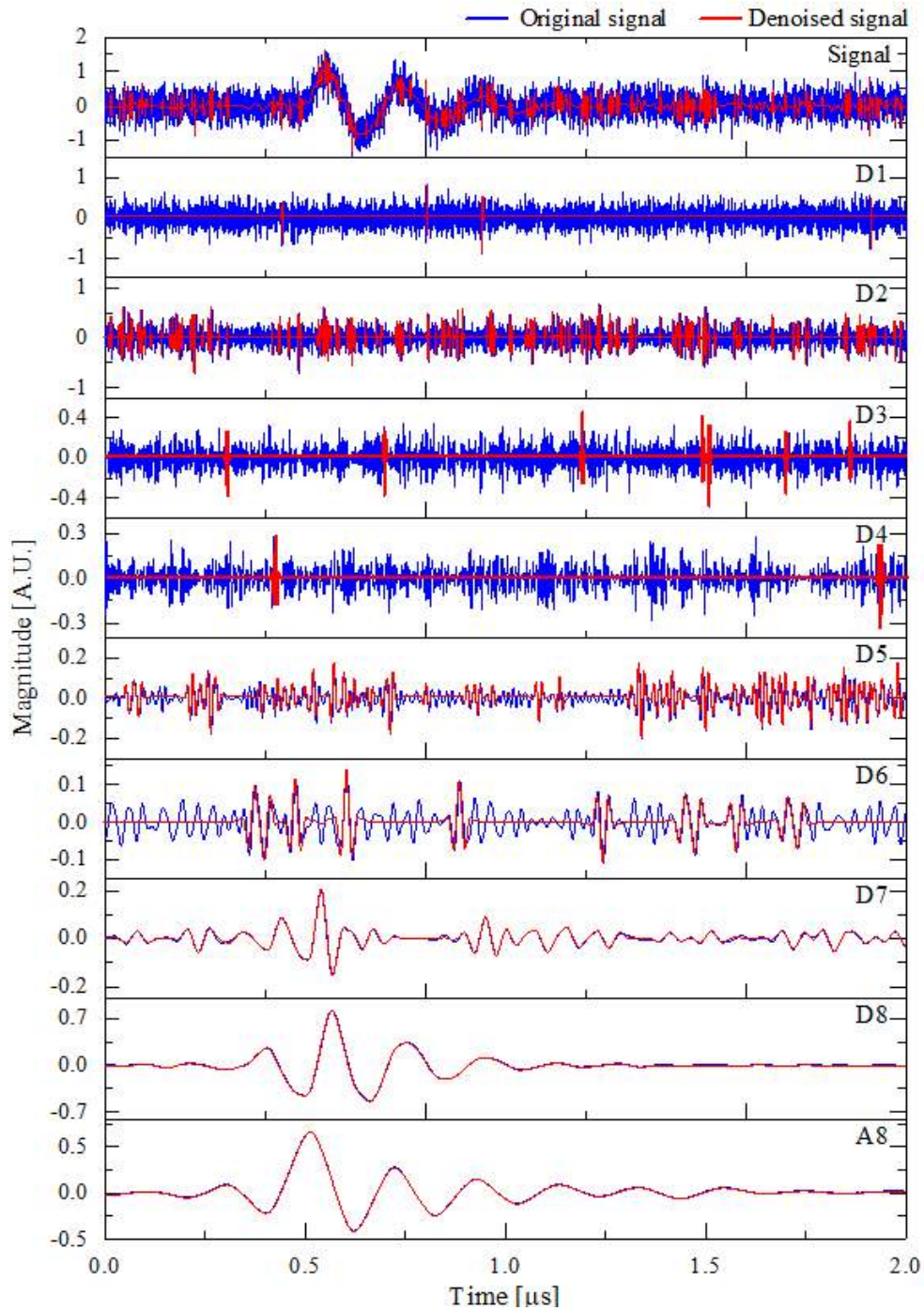


Fig. 3.12 Discrimination of DOP by hard function-SURE threshold

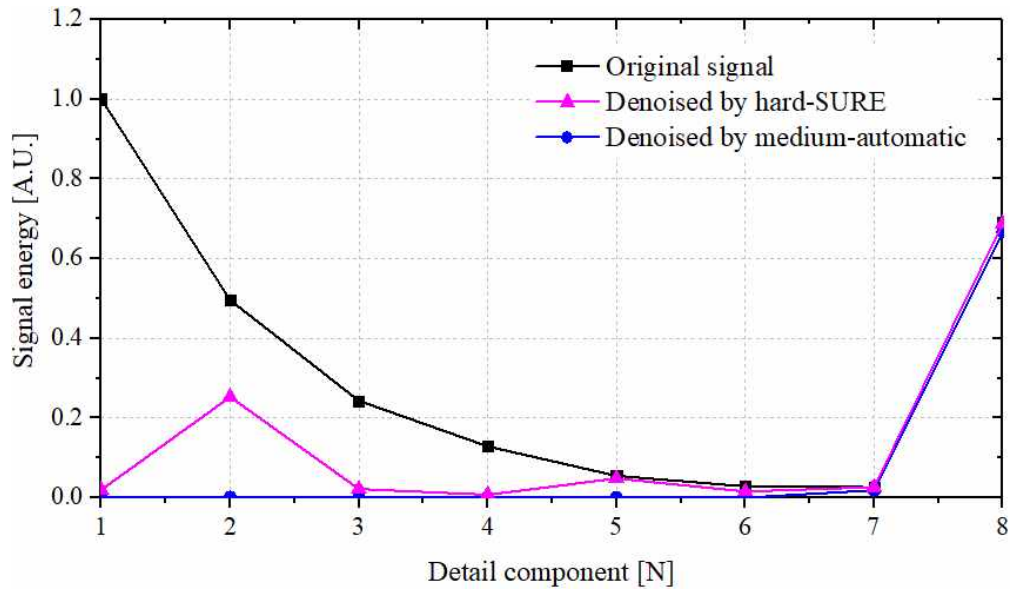


Fig. 3.13 Comparison of signal energy for DOP

Table 3.3 Discrimination results of DOP

Function	Threshold	SNR [dB]	$\gamma$	A%
Hard	Automatic	8.22	0.92	61.79
	SURE	6.16	0.87	60.83
	Hybrid	9.73	0.95	61.38
	Minimax	6.49	0.88	61.06
Soft	Automatic	10.21	0.99	9.41
	SURE	13.31	0.98	28.81
	Hybrid	14.86	0.99	16.35
	Minimax	11.14	0.99	13.34
Medium	Automatic	17.86	0.99	8.76
	SURE	12.68	0.97	33.58
	Hybrid	12.61	0.99	14.66
	Minimax	15.61	0.99	18.88

### 3.2.3 Discrimination of single PD pulses

In order to evaluate the selected thresholding function and threshold and to compare the validity of mother wavelets selected by two methods, the bior6.8 and bior2.6 were applied to denoise the detected PD pulses with medium function-automatic threshold. As there was not a reference signal (simulated pulse) for the actually detected pulses, the RN rather than SNR was considered for comparing the effectiveness of denoising. Results of denoising detected single PD pulses are shown in Table 3.4. It can be seen that denoising with bior2.6 that was selected by the DTW method resulted in a higher values of RN and correlation coefficients, and lower value of A%, compared with the bior6.8 selected by the CC method. The correlation coefficients were nearly 1, which meant that the denoised signals were almost the same with the original signals. Therefore, bior2.6 was selected as the optimal mother wavelet to discriminate PD signal under HVDC.

Table 3.4 Discrimination results of single PD pulses

Defects	bior6.8			bior2.6		
	RN	$\gamma$	A%	RN	$\gamma$	A%
POC	-30.50	0.996	3.18	-30.00	0.996	3.15
POE	-25.48	0.989	5.38	-25.36	0.991	2.81
FP	-25.43	0.996	3.06	-24.05	0.996	2.10
CIS	-16.93	0.978	2.70	-12.70	0.986	2.49
Average	-24.59	0.990	3.58	-23.02	0.992	2.64

## Chapter 4 Discrimination of PD Sequences

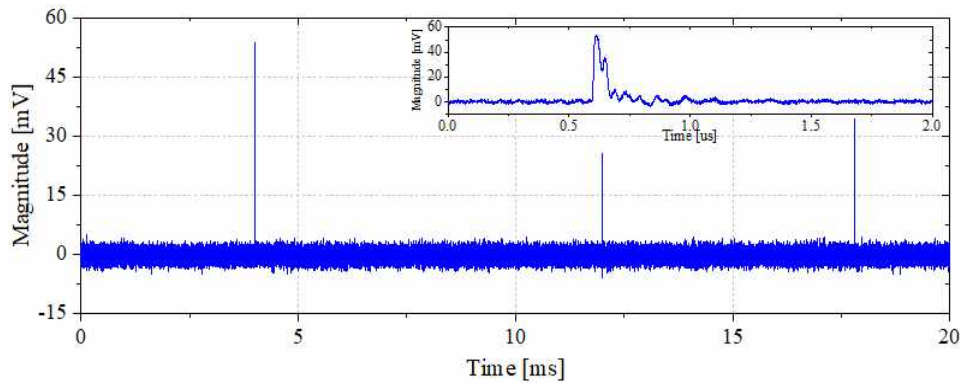
From the pre-denoising of single discharge pulse, it was verified that mother wavelet bior2.6, medium thresholding function, automatic threshold were the optimal selection for dealing with single PD pulse under HVDC. During on-site PD condition monitoring, pulse sequences rather than single pulse are acquired for evaluating the severity of insulation defect, for extracting discharge features and finally for classifying the defect type, such as the TRPD method introduced in Section 2.3. In this chapter, therefore, the optimized wavelet transform techniques were used to discriminate practical PD pulse sequences and the effectiveness was compared with a high-pass filter that had a cutoff frequency of 800 kHz. A DEP-type PD sequence and a DOP-type PD sequence that were interfered by background noise, amplitude modulation (AM) radio interference, non-sinusoidal noise, and switching impulse were used to verify the effect of wavelet de-noising.

Different with previous studies that used calibrated or simulated PD pulse [19,21], the DEP-type and DOP-type pulse sequences in this paper were actually detected from four types of electrode systems, all of which inherently contained the background noise generated from the detection system. Fig. 4.1 shows the sequences with different pulse magnitudes in the FP and CIS. Given the low PD repetition rate under DC, pulse sequences in 20 ms were acquired for further denoising. There were 3 pulses in the DEP-type pulse sequences and 2 pulses were acquired in the DOP-type pulse sequences.

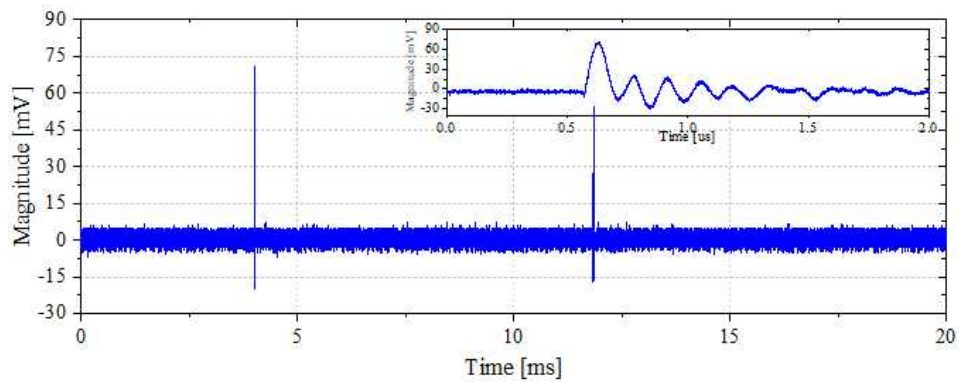
Fig. 4.2 shows three types of noises commonly presented in PD detection. The noises were also acquired in 20 ms and detail information was indicated



in the inset graph. AM radio signal with a central frequency of 600 kHz and a magnitude of 10 mV generated from a signal generator was externally injected to the PD pulse sequence to present the DSI. Fig. 4.2(b) is a periodic non-sinusoidal noise with main component of 2 kHz to simulate interference from power electronics. A switching impulse shown in Fig. 4.2(c) that had a pulse width higher than that of PD pulse was used to represent the stochastic pulse-shaped interferences.

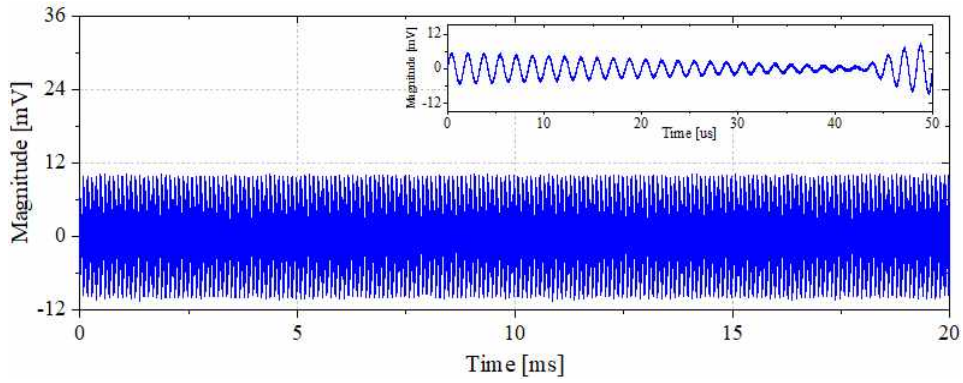


(a) DEP-type pulse

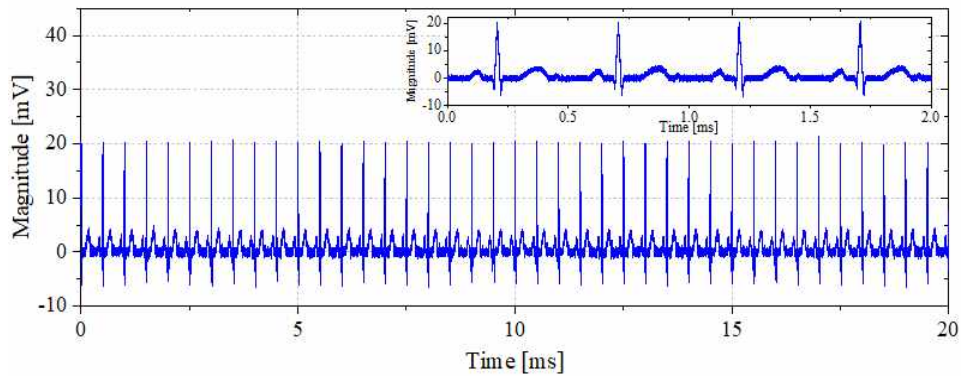


(b) DOP-type pulse

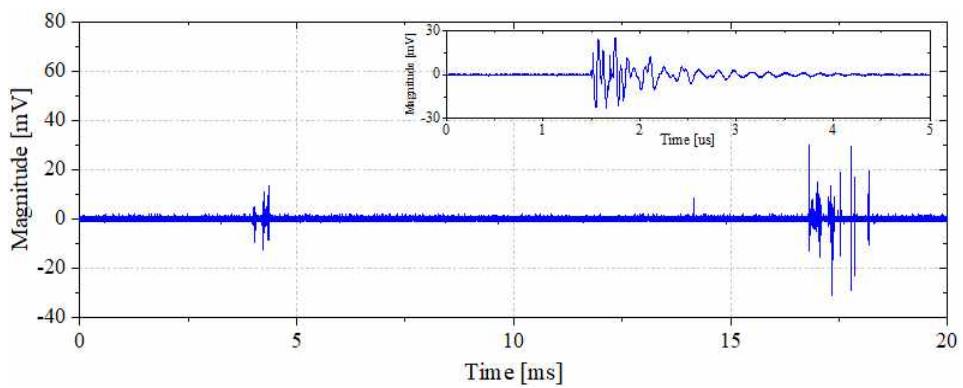
Fig. 4.1 PD pulse sequences



(a) AM radio interference



(b) Non-sinusoidal noise



(c) Switching impulse

Fig. 4.2 Noises in PD detection

The proposed wavelet denoising method was developed based on LabVIEW program. The virtual instruments (VI) block diagram is shown in Fig. 4.3, which is mainly composed of discrete wavelet transformation VI and subVI of threshold, thresholding function as well as denoising evaluation. The interfered signal was first decomposed into 8 levels using bior2.6 mother wavelet by discrete wavelet transformation, generating the detail coefficients at all levels and the approximation coefficients at the highest level. In the loop, the detail coefficients at each decomposition level were extracted respectively and then modified by the selected medium thresholding function and automatic threshold. A shift register was used to pass detail coefficients from previous iteration through the loop to the next iteration. Finally, the modified detail coefficients and the original approximation coefficients were used for signal reconstruction. Effectiveness of denoising was verified by the evaluation subVI, in which the reduction in noise, correlation coefficient, and change in amplitude were calculated.

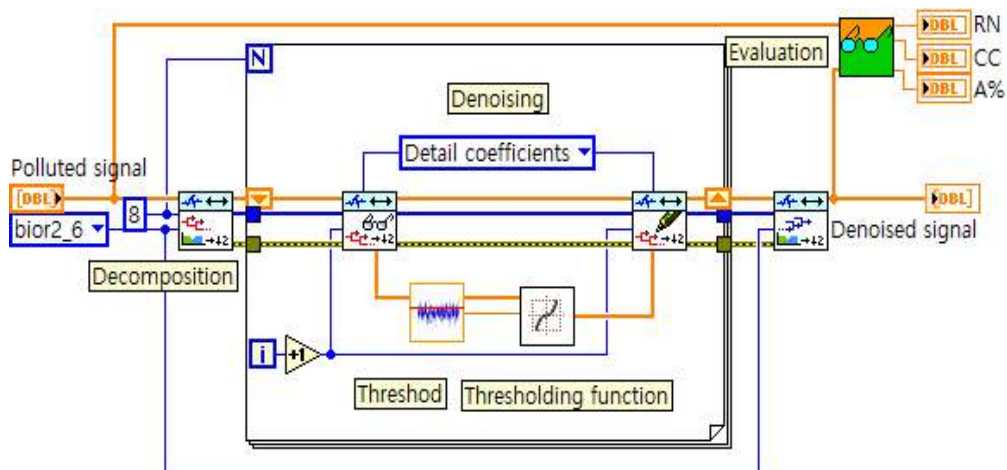
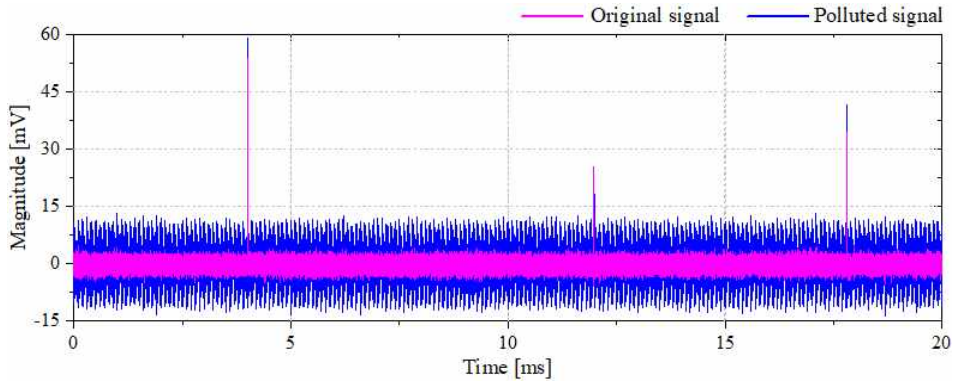


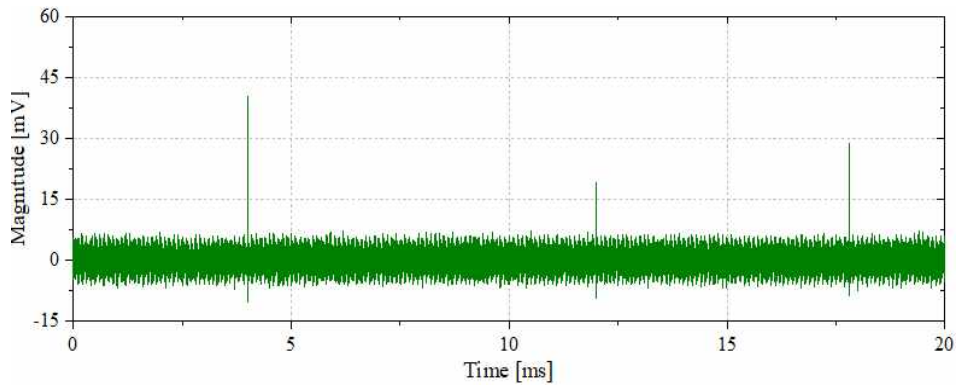
Fig. 4.3 VI block diagram of wavelet denoising

#### 4.1 DEP-type Pulse Sequence

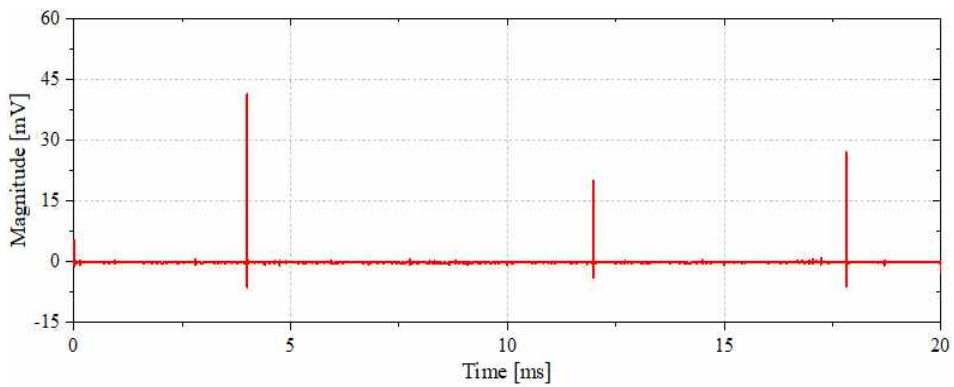
Fig. 4.4 shows discrimination of DEP-type pulse sequence interfered by AM interference using the high-pass filter with cutoff frequency of 800 kHz and the wavelet method. In Fig. 4.4(a), the original signal with three PD pulses that had different magnitudes was detected from the FP electrode system. Such signal was interfered by AM interference with central frequency of 600 kHz. It can be seen that the original signal was immersed in the noise and it is hard to distinguish the second discharge pulse from the interfered signal by visual inspection. The SNR of interfered signal was -23.59 dB. Fig 4.4(b) and (c) show denoising of the interfered signal using high-pass filter and wavelet method, respectively. After denoising by high-pass filter, the background noise and AM interference were not completely eliminated. As a result, the denoised signal had a reduction in noise (RN) of 6.65, a correlation coefficient (CC) of 0.07 with the original signal, and a change in amplitude (A%) of 25.21%. On the contrary, both the background noise and AM interference were significantly reduced by the wavelet method. Details of the application of medium thresholding function-automatic threshold to the detail coefficients and the signal reconstruction are illustrated in Fig. 4.5. Detail coefficients that were related with PD were retained whereas that associated with noise were suppressed, the approximation coefficients were not modified. The denoised signal was reconstructed by all of the modified detail components D1-D8 and the original approximation component A8. The RN, CC, and A% values of signal denoised by wavelet method were 11.64 dB, 0.17, and 23.36%, respectively, all of which showed the superiority compared with the high-pass filter method.



(a) Original signal and interfered signal



(b) Denoised by filter



(c) Denoised by wavelet method

Fig. 4.4 Discrimination of DEP-type pulse interfered by AM interference

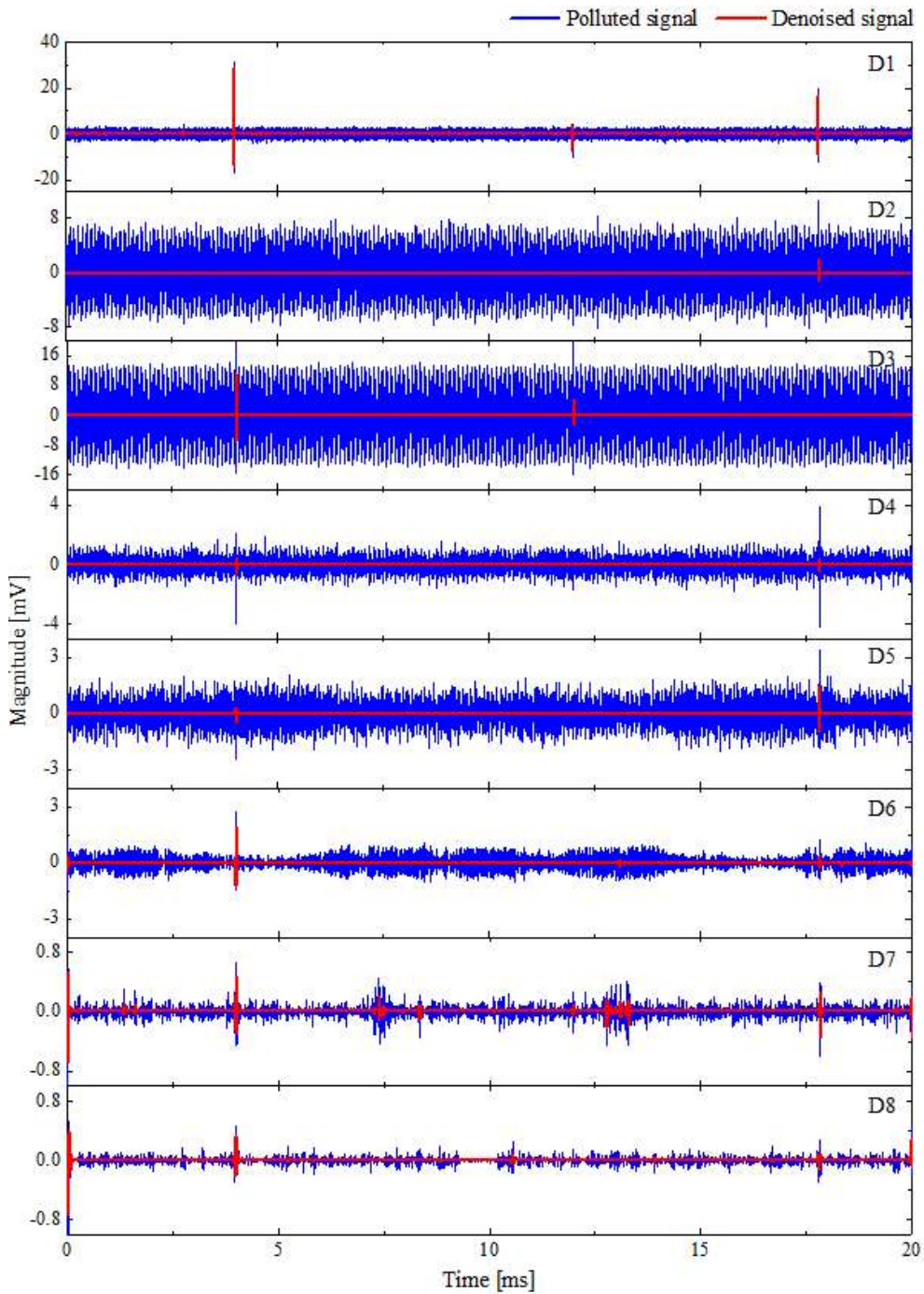
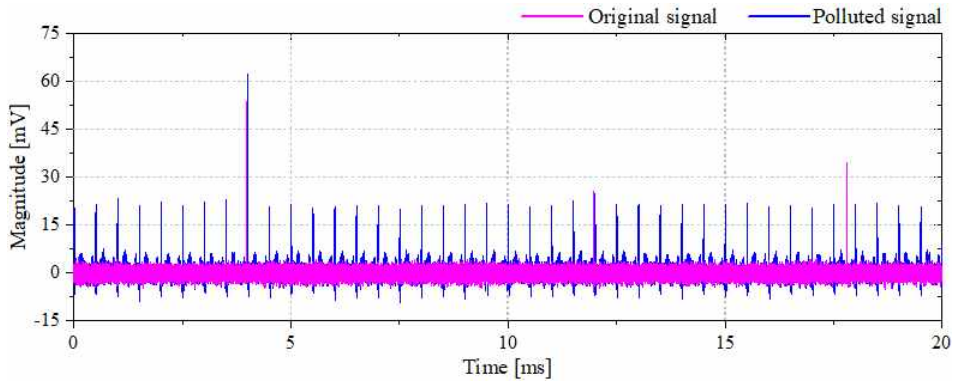


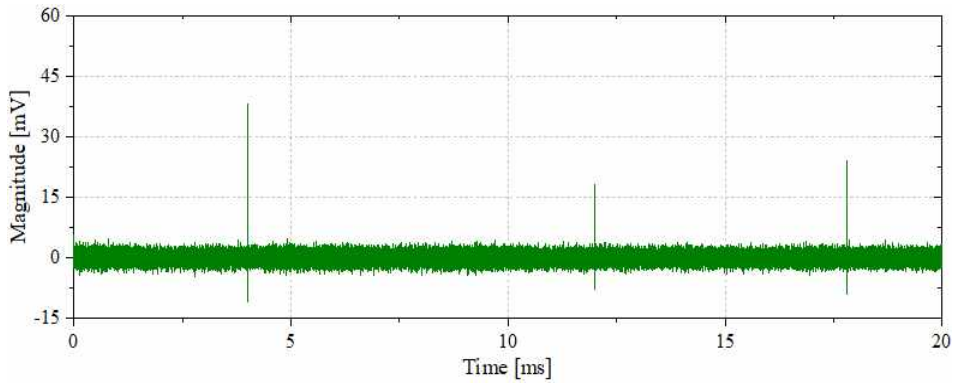
Fig. 4.5 Elimination of AM interference in DEP-type pulse by wavelet method

Discrimination of DEP-type pulse interfered by periodic non-sinusoidal noise is shown in Fig. 4.6. The noise contained 2 kHz component with magnitude of 20 mV and other components with frequencies lower than 2 kHz and lower magnitudes. As shown in Fig. 4.6(a), the second PD pulse was completely buried in the non-sinusoidal noise and it was impossible to be identified without the help of denoising. The SNR of interfered signal was -24.55 dB. Although applying the high-pass filter can reduce the periodic non-sinusoidal noise, background noise was also remained, as shown in Fig. 4.6(b). Denoising by the high-pass filter method resulted in a reduction in noise of 0.19 dB, a correlation coefficient of 0.13, and a change in amplitude of 29.41%. Decomposition of the interfered signal into 8 levels using the optimized wavelet method (mother wavelet bior2.6, medium thresholding function, automatic threshold) is shown in Fig. 4.7. It was indicated that the detail components D1-D5 contained PD signal whereas the detail components D6-D8 were related with the background noise and the periodic non-sinusoidal noise. However, denoising with wavelet method did not eliminate the noise-related coefficients in detail components D6-D8. It was therefore only detail components at levels 1-5 were used for signal reconstruction, as the denoised signal shown in Fig. 4.6(c). From visual inspection, both the background noise and the periodic non-sinusoidal noise were significantly reduced. Denoising using the wavelet method resulted in a reduction in noise of 0.71, dB, a correlation coefficient of 0.17, and a change in amplitude of 27.67%, all of which revealed the higher performance of wavelet method compared with the high-pass filter method.

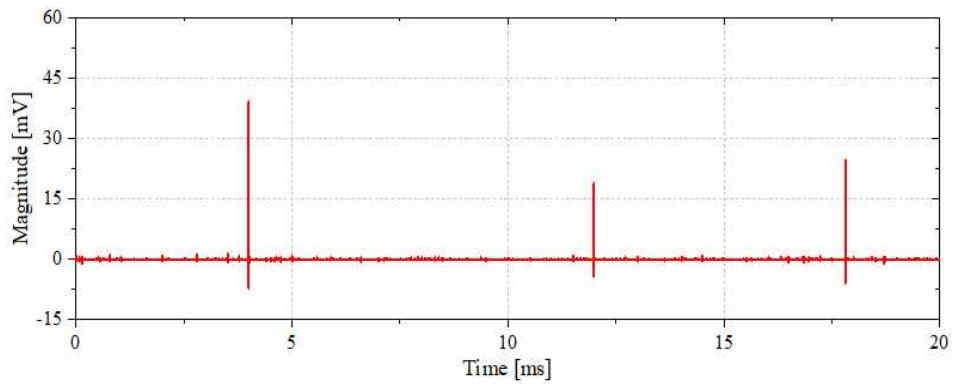




(a) Original signal and interfered signal



(b) Denoised by filter



(c) Denoised by wavelet method

Fig. 4.6 Discrimination of DEP-type pulse interfered by non-sinusoidal noise



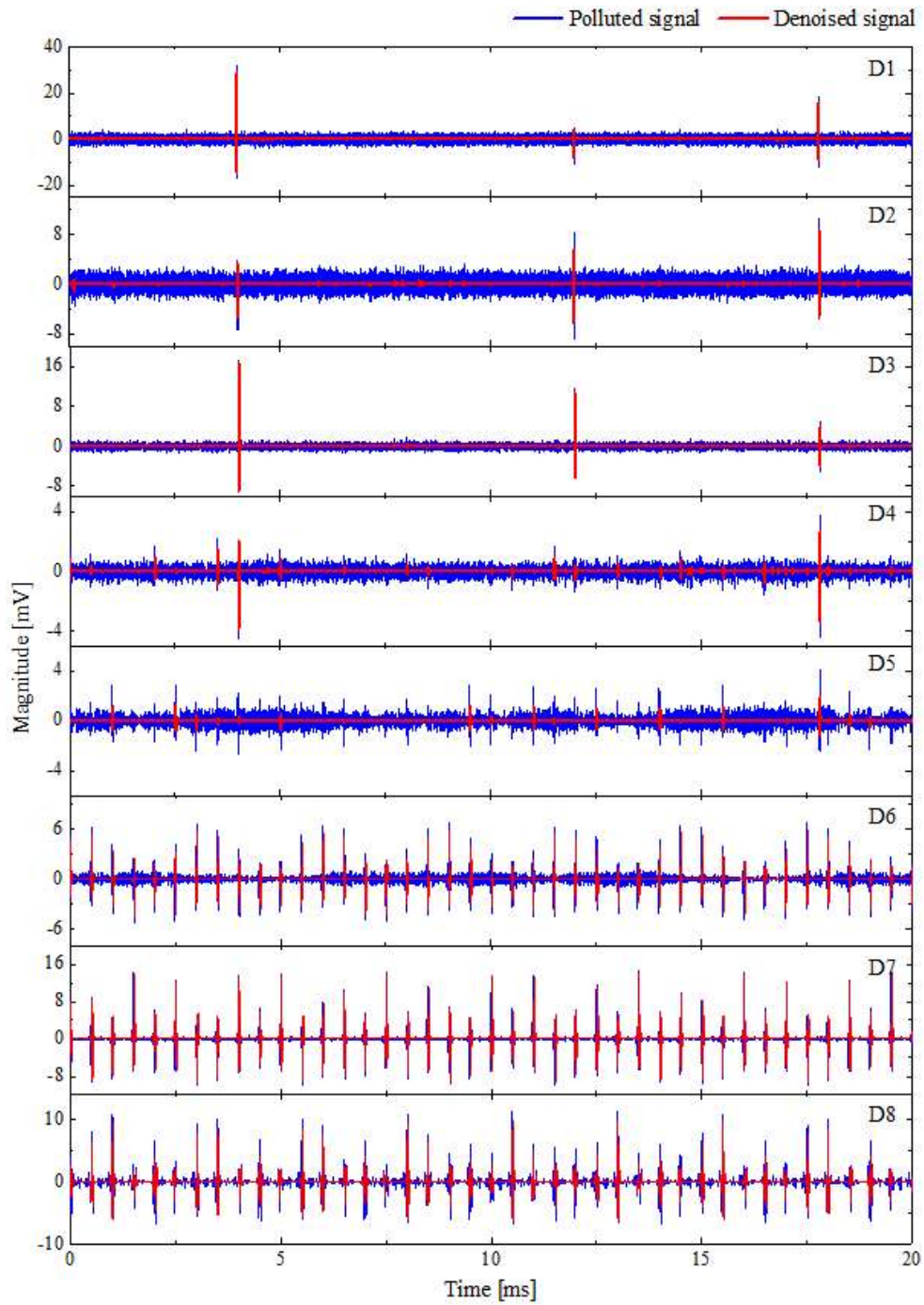
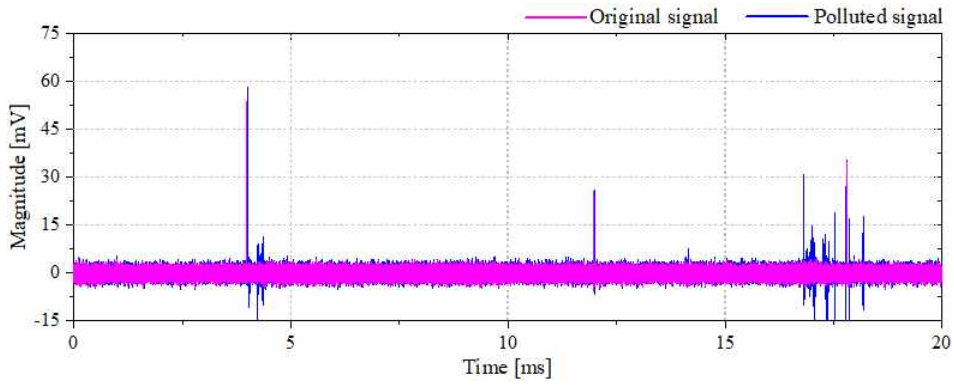
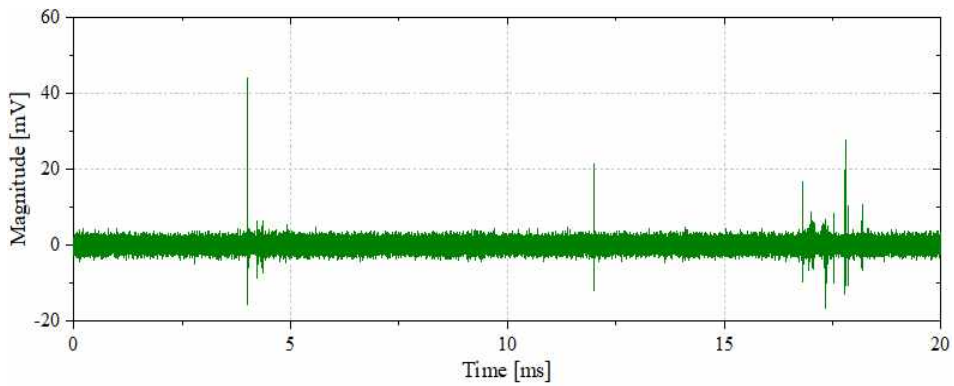


Fig. 4.7 Elimination of non-sinusoidal noise in DEP-type pulse by wavelet method

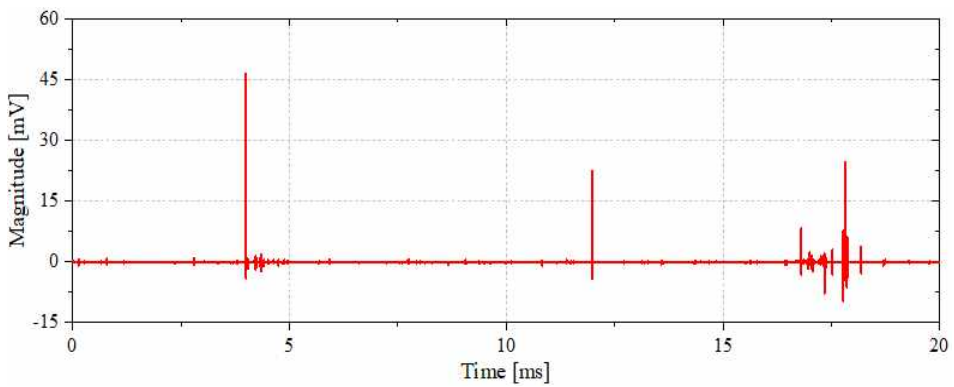
Fig. 4.8 shows discrimination of DEP-type pulse sequence that was interfered by switching impulse. Compared with PD pulses shown in Fig 3.3, the switching impulse in Fig. 4.8(a) had longer pulse width. The peak magnitude of switching impulse was 30 mV and the magnitude of the third PD pulse was 34.84 mV. From the interfered signal shown in Fig. 4.8(a), the third discharge pulse was totally merged with the switching impulse and it was impossible to be discriminated by visual inspection. Owing to the background noise and switching impulse, the SNR of interfered signal was -15.38 dB. Fig. 4.8(b) illustrates the denoising result using the high-pass filter with cutoff frequency of 800 kHz. It can be seen that only partial background noise and switching impulse were suppressed and the third discharge pulse was still buried in the noise and hard to be identified. After denoising by high-pass filter, the reduction in noise was -12.72 dB. The correlation coefficient and change in amplitude were 0.15 and 18.24%, respectively. In Fig. 4.9, the interfered signal was decomposed into 8 levels using bior2.6 as mother wavelet and then was denoised using medium thresholding function and automatic threshold. The blue and red signal presented the interfered and denoised PD sequence at each decomposition level, respectively. Denoised signal was reconstructed by all of the modified detail components from D1 to D8. The denoising result using wavelet method is shown in Fig. 4.8(c), the background noise was completely removed and most of the switching impulse were suppressed. Denoising using wavelet method resulted in a reduction in noise of -7.14 dB, which was higher than that obtained from the high-pass filter method. The correlation coefficient and change in amplitude were 0.20 and 13.89%, respectively.



(a) Original signal and interfered signal



(b) Denoised by filter



(c) Denoised by wavelet method

Fig. 4.8 Discrimination of DEP-type pulse interfered by switching impulse

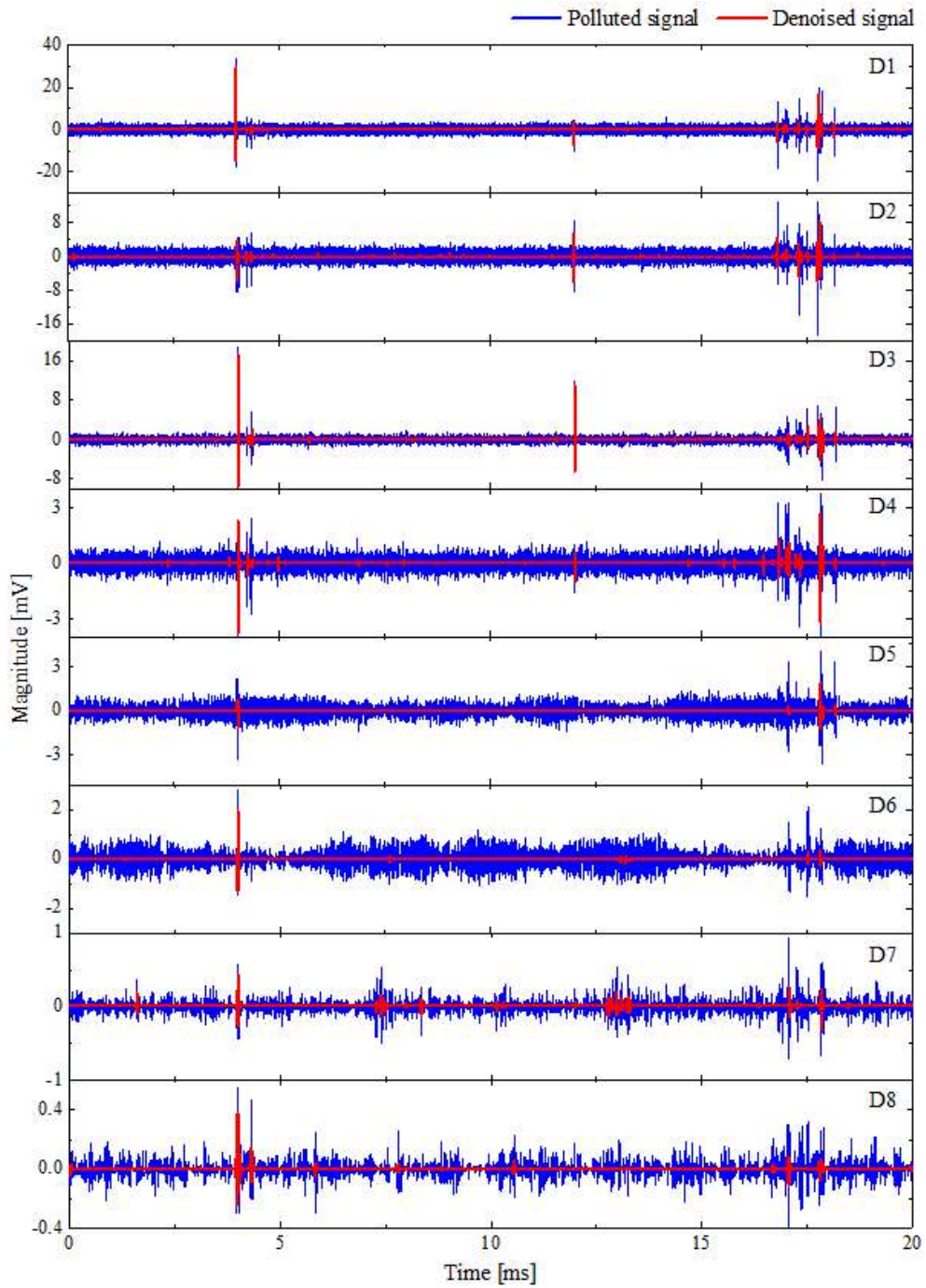
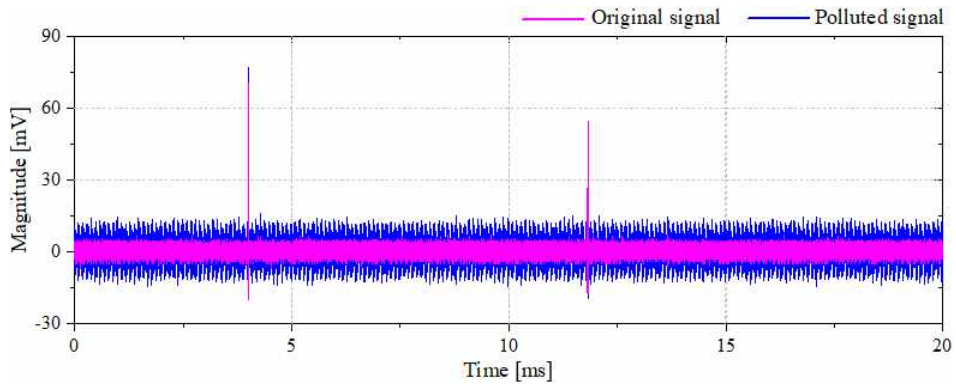


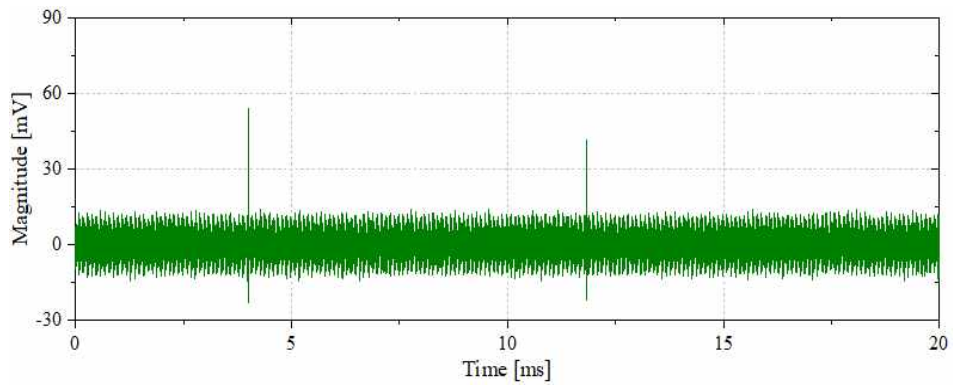
Fig. 4.9 Elimination of switching impulse in DEP-type pulse by wavelet method

## 4.2 DOP-type Pulse Sequence

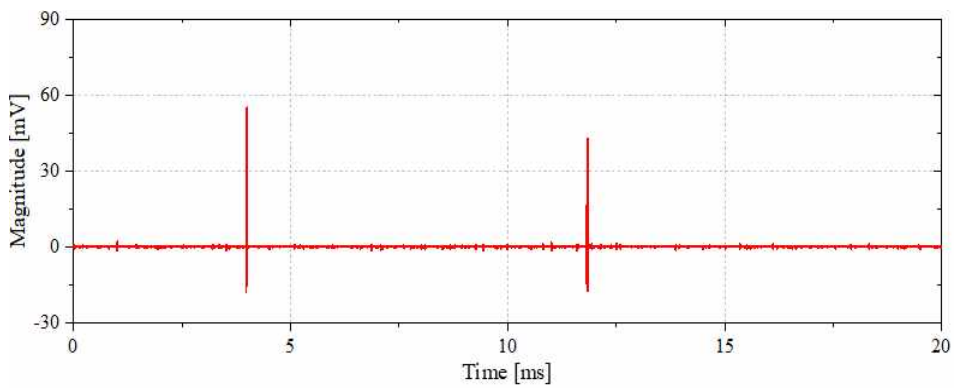
The DOP-type pulse sequence detected from the crack electrode system and interfered by AM interference as well as background noise is shown in Fig. 4.10(a). There were two discharge pulses with magnitudes of 71 mV and 55 mV in the sequence. The AM interference had a central frequency of 600 kHz and a magnitude of 10 mV. It can be seen that the oscillation of the first pulse at negative part cannot be discriminated as it was superposed on the positive rising edge of AM interference. The SNR of DOP-type pulse sequence contained background noise and AM interference was -20.45 dB. Denoising of the interfered signal using the 800 kHz high-pass filter is shown in Fig. 4.10(b). Only partial background noise and AM interference were removed and the denoising resulted in a reduction in noise of 4.55 dB, a correlation coefficient of 0.10, and a change in amplitude of 24.15 %. Fig. 4.11 demonstrates the decomposition of the interfered signal into 8 levels using the mother wavelet bior2.6, medium thresholding function, and automatic threshold. Detail coefficients at each level were modified and all of the detail components from D1 to D8 were used for signal reconstruction. The denoising result obtained from wavelet method is shown in Fig. 4.10(c). It was indicated that the background noise and AM interference were significantly eliminated and the oscillation of the first pulse at negative part was also recovered. After denoising by the wavelet method, the reduction in noise was 6.03 dB. The correlation coefficient and change in amplitude were 0.17 and 22.41%, respectively. Wavelet transform technique shown its higher performance in suppressing background noise and AM interference compared with the high-pass filter.



(a) Original signal and interfered signal



(b) Denoised by filter



(c) Denoised by wavelet method

Fig. 4.10 Discrimination of DOP-type pulse interfered by AM interference



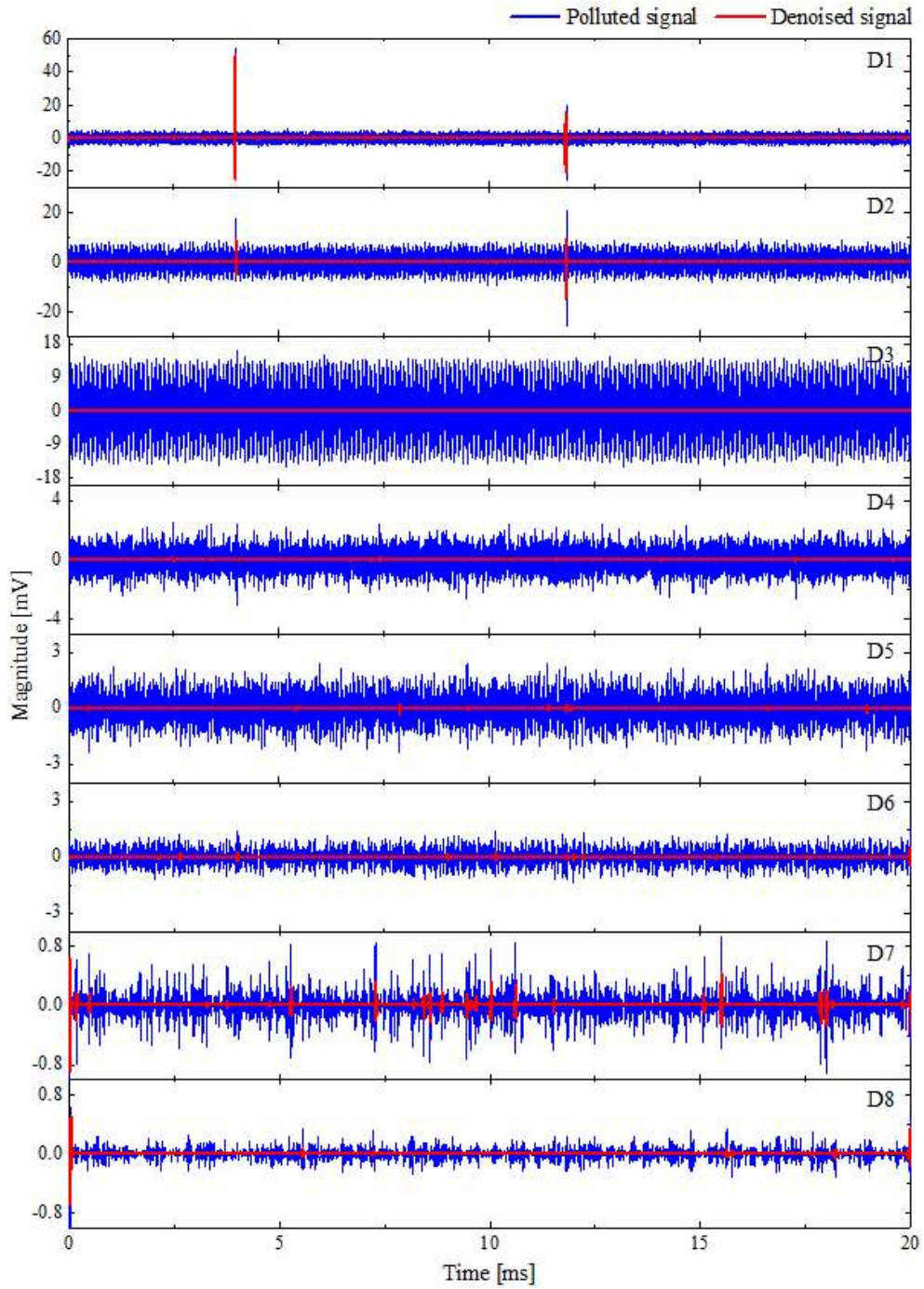
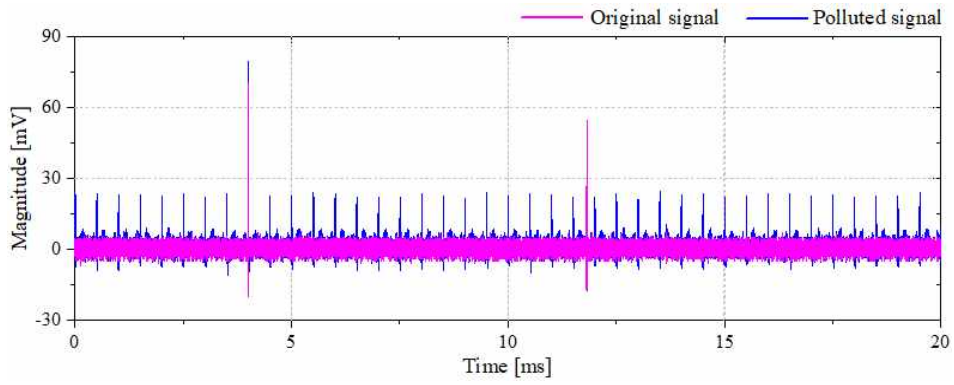


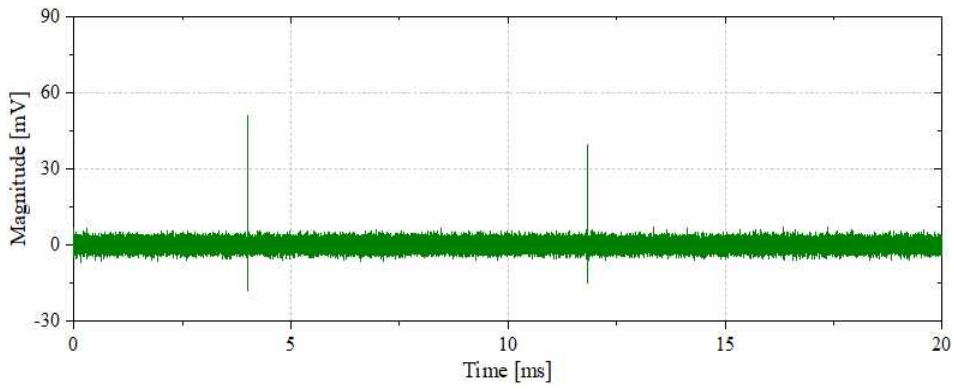
Fig. 4.11 Elimination of AM interference in DOP-type pulse by wavelet method

Fig. 4.12 demonstrates the elimination of periodic non-sinusoidal noise from interfered DOP-type pulse sequence. In Fig. 4.12(a), the interfered signal had a SNR of  $-23.20$  dB. The non-sinusoidal noise had main component with frequency of  $2$  kHz and magnitude of  $20$  mV and other components with magnitudes lower than  $20$  mV. It can be seen that the first PD pulse with magnitude of  $71$  mV merged with the noise pulse, resulting in an increase in the peak magnitude of pulse sequence. This case may lead to an overvaluation of the PD severity and cause an erroneous diagnosis result. The result of denoising using the high-pass filter is shown in Fig. 4.12(b). Applying the high-pass filter suppressed the periodic non-sinusoidal, however, there were still remained interference in the denoised signal. The reduction in noise, correlation coefficient, and change in amplitude of filter method were  $1.04$  dB,  $0.16$ , and  $28.27\%$ , respectively. Fig. 4.13 illustrates the original detail components of interfered signal in 8 levels and the modified detail components that were denoised by bior2.6 mother wavelet, medium thresholding function, and automatic threshold. As denoising of DEP-type pulse sequence interfered by non-sinusoidal noise, most of PD-related components were observed in detail components D1-D5, they were therefore denoised and then used for signal reconstruction. Although denoised by wavelet method, the detail components D6-D8 were found to be related with background noise and periodic non-sinusoidal noise, therefore, they were discarded instead of being used for signal reconstruction. Fig. 4.12(c) shows the denoised signal obtained by wavelet method. The reduction in noise was  $1.87$  dB. The correlation coefficient and change in amplitude were  $0.17$  and  $24.90\%$ , respectively.

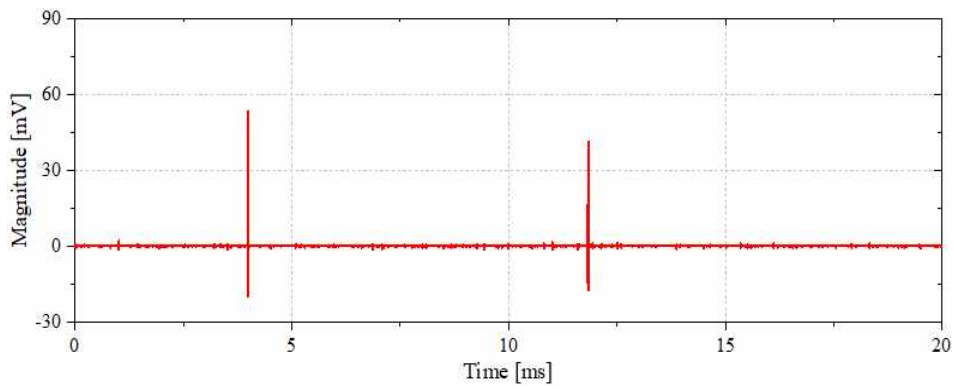




(a) Original signal and interfered signal



(b) Denoised by filter



(c) Denoised by wavelet method

Fig. 4.12 Discrimination of DOP-type pulse interfered by non-sinusoidal noise

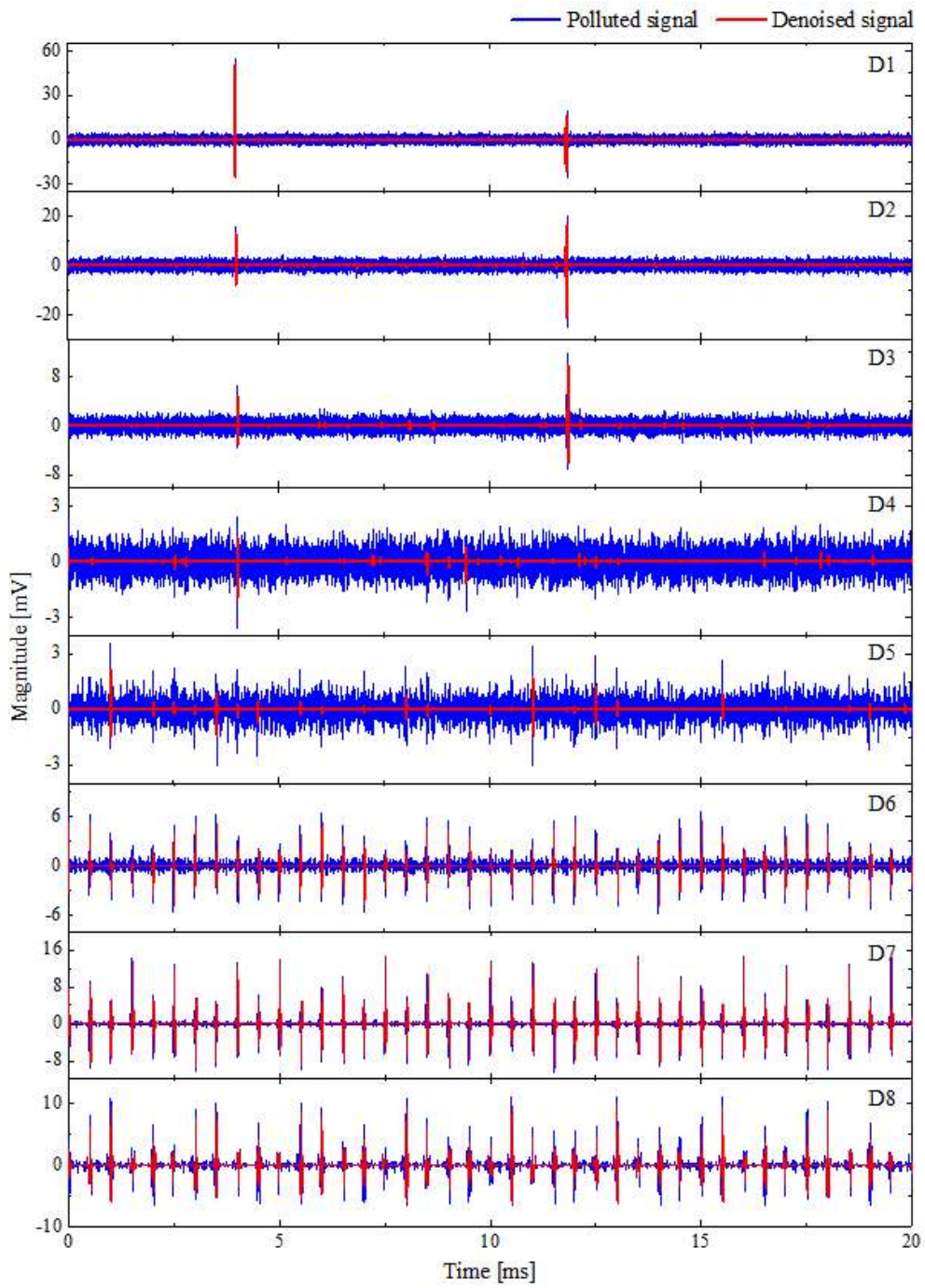
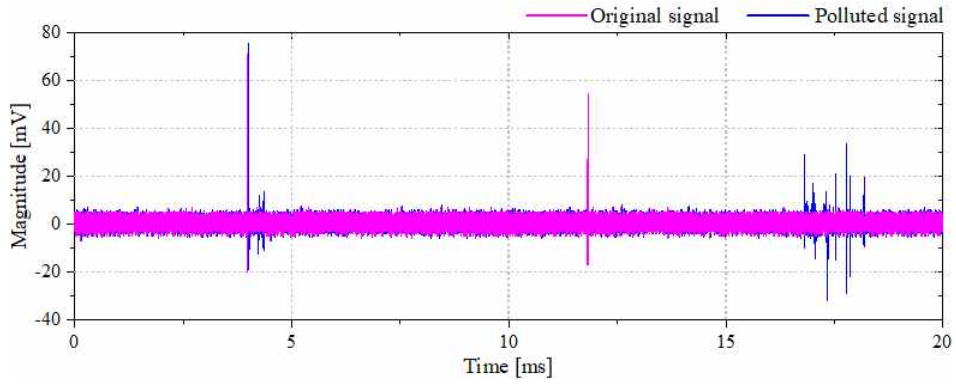
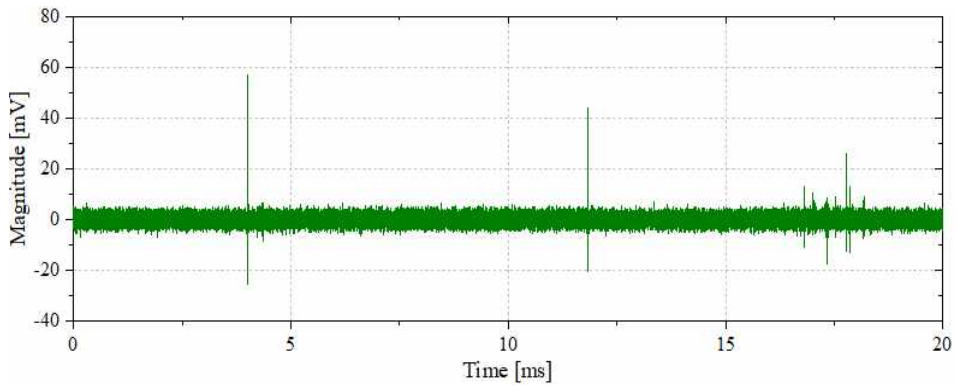


Fig. 4.13 Elimination of non-sinusoidal noise in DOP-type pulse by wavelet method

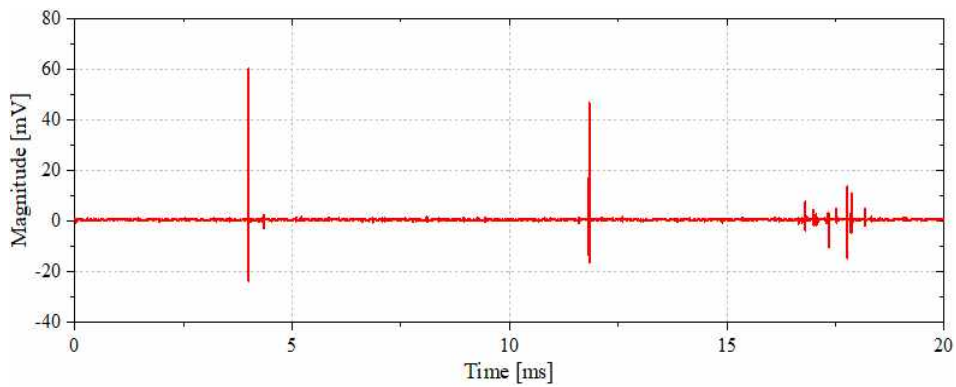
Fig. 4.14 shows the discrimination of DOP-type pulse interfered by switching impulse. It can be seen from Fig. 4.14(a) that although the switching impulses between 15 ms and 20 ms were not superposed with PD pulses, they can be erroneously identified as discharge pulses, resulting mistake in counting the discharge number. After polluting by the switching impulse, the signal had a SNR of  $-10.37$  dB. Result of denoising the interfered signal using the 800 kHz high-pass filter is shown in Fig. 4.14 (b). After applying the high-pass filter, the peak magnitude of switching impulse was reduced from 35 mV to 27 mV. However, the background noise and switching impulse still remained in the original signal and can be observed by visual inspection. In Fig. 4.14 (b), the reduction in noise was  $-8.81$  dB. The correlation coefficient was 0.15 and the change in amplitude after denoising was 20.11%. The interfered signal was decomposed into 8 levels using mother wavelet bior2.6 and then the detail components were denoised by medium thresholding function and automatic threshold. The details of decomposition and denosing are shown in Fig. 4.15, where the blue and red signal presented the interfered and denoised PD components at each decomposition level, respectively. All of the modified detail components in 8 levels were used for reconstructing the denoised signal and the denoising result is shown in Fig. 4.14(c). It was revealed that both the background noise and the switching impulse were greatly eliminated. The peak magnitude of switching impulse was reduced to 15 mV. Denoising using wavelet method resulted in a reduction in noise of  $-4.15$  dB, a correlation coefficient of 0.21, and a change in amplitude of 15.58%. The denoising results showed the superiority of wavelet method compared with the high-pass filter method.



(a) Original signal and interfered signal



(b) Denoised by filter



(c) Denoised by wavelet method

Fig. 4.14 Discrimination of DOP-type pulse interfered by switching impulse

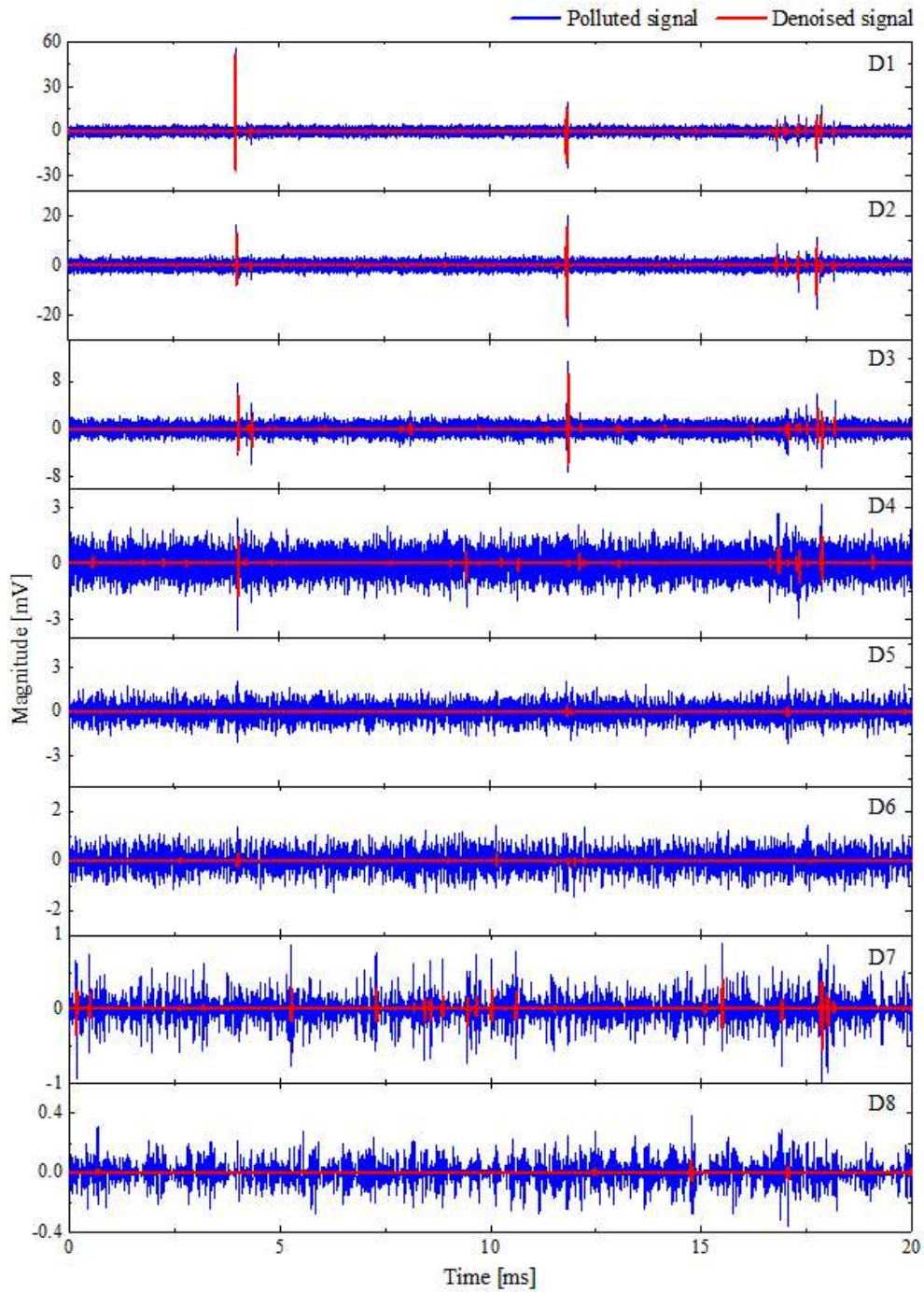


Fig. 4.15 Elimination of switching impulse in DOP-type pulse by wavelet method

A summary of results of PD signal discrimination is shown in Table 4.1. The wavelet method showed its effectiveness in denoising DEP-type PD sequence and DOP-type PD sequence that were interfered by background noise, amplitude modulation radio interference, non-sinusoidal noise, and switching impulse. It was also indicated that discrimination of PD signal using wavelet techniques resulted in higher values of reduction in noise as well as correlated coefficient, and lower value of change in amplitude compared with the high-pass filter. Therefore, the optimized wavelet method can be applied to on-line PD detection in GIS under HVDC for improving the detection sensitivity and the accuracy of insulation diagnosis.

Table 4.1 Results of PD signal discrimination

Pulse sequence	Noise	Wavelet			Filter		
		RN	CC	A%	RN	CC	A%
DEP	AM	11.64	0.17	23.36	6.65	0.07	25.21
	Non-sinusoidal	0.71	0.17	27.67	0.19	0.13	29.41
	Switching impulse	-7.14	0.20	13.89	-12.72	0.15	18.24
DOP	AM	6.03	0.17	22.41	4.55	0.10	24.15
	Non-sinusoidal	1.87	0.17	24.90	1.04	0.16	28.27
	Switching impulse	-4.15	0.21	15.58	-8.81	0.15	20.11
Average		1.49	0.18	21.30	-1.52	0.13	24.23

## Chapter 5 Conclusions

This dissertation dealt with discrimination of PD signals interfered by noises and interferences using wavelet transform for on-line condition monitoring and diagnosis of HVDC GIS, aiming to improve the detection sensitivity and further the accuracy of severity assessment.

Single PD pulses were extracted from typical insulation defects in GIS, including protrusion on conductor (POC), protrusion on enclosure (POE), free particle (FP), and crack inside spacer (CIS), for determining the optimal mother wavelet. The correlation coefficient and dynamic time warping method were used to compare the similarity between PD pulses and various mother wavelets. It was verified that mother wavelet bior2.6 selected by dynamic time warping method was the most appropriate for analyzing PD signal under HVDC.

A damped exponential pulse (DEP) and a damped oscillatory pulse (DOP) were simulated for selecting the optimal thresholding function and threshold. Application of medium thresholding function-automatic threshold in denosing DEP resulted in the highest signal-to-noise ratio (SNR) of 12.59 dB, the highest correlation coefficient of 0.97, and the lowest change in amplitude of 0.67. The similar results were obtained from denosing of DOP using medium function-automatic threshold. The SNR of noisy signal was increased to 17.86 dB. The correlation coefficient and change in amplitude were 0.99 and 8.76, respectively. Therefore, the medium-automatic combination was selected as the optimal thresholding function and threshold.

The optimized wavelet techniques were used for discriminating DEP-type and DOP-type PD sequences that were actually detected from artificial defects and interfered by background noise, amplitude modulation radio interference, periodic non-sinusoidal noise, and switching impulse. Although the PD pulses were immersed in the noises and cannot be distinguished by visual inspection, they can be recovered after applying wavelet denoising. Denoising with the wavelet method resulted in an average reduction in noise of 1.49 dB, correlation coefficient of 0.18, and change in amplitude of 21.30, all of which showed the superiority of wavelet method compared with the high-pass filter method.

The proposed wavelet techniques were verified to be effective in discriminating PD signals from noises and interferences. Results from this dissertation were expected to be applied for insulation diagnosis of HVDC GIS, by which accuracies of PD detection, risk assessment, defect identification and localization can be significantly improved.



## References

- [1] P. Gill, "Electrical Power Equipment Maintenance and Testing", CRC Press, New York, United State, pp. 1-18, 2008.
- [2] G. Balzer, W. Degen, M. Halfmann, T. Hartkopf, and C. Neumann, "Strategies for Optimizing the use of Substation Assets", CIGER Session B3, Paris, France, pp. 1-8, 2004.
- [3] G. M. Wang and G. S. Kil, "Measurement and Analysis of Partial Discharge using an Ultra-High Frequency Sensor for Gas Insulated Structures", *Metrol. Meas. Syst.*, Vol. 24, No. 3, pp. 515-524, 2017.
- [4] CIGRE Working Group D1.03, "Risk Assessment on Defects in GIS based on PD Diagnostics", CIGRE Publication, Paris, France, 2013.
- [5] IEC 60270, "High-Voltage Test Techniques - Partial Discharge Measurements", 3rd Edition, IEC Publication, Geneva, Switzerland, 2015.
- [6] G. M. Wang, S. J. Kim, G. S. Kil, and S. W. Kim, "Optimization of Wavelet and Thresholding for Partial Discharge Detection under HVDC", *IEEE Trans. Dielectr. Electr. Insul.*, Vol. 24, No. 1, pp. 200-208, 2017.
- [7] M. Wang. A. 1. Vandermaar, and K. D. Srivastava, "Review of Condition Assessment of Power Transformers in Service", *IEEE Electr. Insul. Mag.*, Vol. 18, No. 6, pp. 12-25, 2004.
- [8] S. Tenbohlen, D. Denissov, S. M. Hoek, and S. M. Markalous, "Partial Discharge Measurement in the Ultra High Frequency (UHF) Range", *IEEE Trans. Dielectr. Electr. Insul.*, Vol. 15, No. 6, pp. 1544-1552, 2008.
- [9] M. D. Judd, L. Yang, and I. B. B. Hunter, "Partial Discharge Monitoring for Power Transformers using UHF Sensors Part 1: Sensors and Signal Interpretation", *IEEE Electr. Insul. Mag.*, Vol. 21 , No. 2, pp. 5-14, 2005.

- [10] M. Wu, H. Cao, J. Cao, H. L. Nguyen, J. B. Gomes, and S. P. Krishnaswamy, "An Overview of State-of-the-Art Partial Discharge Analysis Techniques for Condition Monitoring", IEEE Electr. Insul. Mag., Vol. 31, No. 6, pp. 22-35, 2015.
- [11] G. M. Wang, H. E. Jo, S. I. Kim, S. W. Kim, and G. S. Kil, "Measurement and Analysis of Partial Discharge in SF<sub>6</sub> Gas under HVDC", Measurement, Vol. 91, pp. 351-359, 2016.
- [12] P. H. F. Morshuis and I. I. Smit, "Partial Discharges at dc Voltage: Their Mechanism, Detection and Analysis", IEEE Trans. Dielectr. Electr. Insul., Vol. 12, No. 2, pp. 328-340, 2005.
- [13] R. Piccin, A. R. Mor, P. Morshuis, A. Girodet, and J. Smit, "Partial Discharge Analysis of Gas Insulated Systems at High Voltage AC and DC", IEEE Trans. Dielectr. Electr. Insul., Vol. 22, No. 1, pp. 218-228, 2015.
- [14] F. H. Kreuger, "Partial Discharge Detection in High-Voltage Equipment", Butterworths, London, United Kingdom, pp. 1-152, 1990.
- [15] A. Haddad and D. F. Warne, "Advances in High Voltage Engineering", The Institution of Engineering and Technology, Stevenage, United Kingdom, pp. 37-54, 2004.
- [16] H. M. Ryan, "High-voltage Engineering and Testing", The Institution of Engineering and Technology, Stevenage, United Kingdom, pp. 319-324, 2013.
- [17] IEC 62271-203, "High-Voltage Switchgear and Controlgear-Part 203: Gas-Insulated Metal-Enclosed Switchgear for Rated Voltages above 52kV", 2nd Edition, IEC Publication, Geneva, Switzerland, 2011.

- [18] H. Zhang, T. R. Blackburn, B.T. Phung, and D. Sen, "A Novel Wavelet Transform Technique for On-line Partial Discharge Measurements Part I : WT De-noising Algorithm", IEEE Trans. Dielectr. Electr. Insul., Vol. 14, No. 1, pp. 3-14, 2007.
- [19] L. Satish and B. Nazneen, "Wavelet-based Denoising of Partial Discharge Signals Buried in Excessive Noise and Interference", IEEE Trans. Dielectr. Electr. Insul., Vol. 10, No. 2, pp. 354-367, 2003.
- [20] G. M. Wang, G. S. Kil, H. K. Ji, and J. H. Lee, "Disturbance Elimination for Partial Discharge Detection in the Spacer of Gas-Insulated Switchgears", Energies, Vol. 10, No. 11, 1762, 2017.
- [21] X. Ma, C. Zhou, and I. J. Kemp, "Interpretation of Wavelet Analysis and Its Application in Partial Discharge Detection", IEEE Trans. Dielectr. Electr. Insul., Vol. 9, No. 3, pp. 446-457, 2002.
- [22] X. Zhou, C. Zhou, and I. J. Kemp, "An Improved Methodology for Application of Wavelet Transform to Partial Discharge Measurement Denoising", IEEE Trans. Dielectr. Electr. Insul., Vol. 12, No. 3, pp. 586-594, 2005.
- [23] R. Bartnikas, "Partial Discharges, Their Mechanism, Detection and Measurement", IEEE Trans. Dielectr. Electr. Insul., Vol. 9, No. 5, pp. 763-808, 2002.
- [24] S. A. Boggs, "Partial Discharge Overview and Signal Generation", IEEE Electr. Insul. Mag., Vol. 6, No. 4, pp. 33-39, 1990.
- [25] H. Okubo, M. Yoshida, T. Takahashi, and T. Hoshino, "Partial Discharge Measurement in a Long Distance SF<sub>6</sub> Gas", IEEE Trans. Power Del., Vol. 13, No. 3, pp. 683-690, 1998.

- [26] CIGRE Working Group D1.29, “Partial Discharges in Transformers”, CIGRE Publication, Paris, France, 2017.
- [27] IEEE, “Guide for Partial Discharge Testing of Shielded Power Cable Systems in a Field Environment”, IEEE Power Engineering Society, New York, United State, 2006.
- [28] U. Fromm, “Interpretation of Partial Discharges at dc Voltages”, IEEE Trans. Dielectr. Electr. Insul., Vol. 2, No. 5, pp. 761-770, 1995.
- [29] G. M. Wang. “Analysis on Statistical Characteristics of Partial Discharge in SF<sub>6</sub> under HVDC”, Master Thesis, Korea Maritime and Ocean University, 2015.
- [30] R. Piccin, “Partial Discharge Analysis in HVDC Gas Insulated Substations”, Delft University of Technology, 2013.
- [31] CIGRE Working Group D1.33, “Guide for Electrical Partial Discharge Measurements in Compliance to IEC 60270”, CIGRE Publication, Paris, France, 2008.
- [32] IEEE, “Guide for the Detection and Location of Acoustic Emissions from Partial Discharge in Oil-immersed Power Transformers and Reactors”, IEEE Power Engineering Society, New York, United State, 2007.
- [33] L. E. Lundgaard, “Partial Discharge Part XIII : Acoustic Partial Discharge Detection-Fundamental Considerations”, IEEE Electr. Insul. Mag., Vol. 8, No. 4, pp. 25-31, 1992.
- [34] IEC TS 62478, “High Voltage Test Techniques – Measurement of Partial Discharges by Electromagnetic and Acoustic Methods”, IEC Publication, Geneva, Switzerland, 2016.

- [35] G. S. Kil, I. K. Kim, D. W. Park, S. Y. Choi, and C. Y. Park, "Measurements and Analysis of the Acoustic Signals Produced by Partial Discharge in Insulation Oil", *Curr. Appl. Phys.*, Vol. 9, No. 2, pp. 296-300, 2009.
- [36] N. Guptas and T. S. Ramu, "Estimation of Partial Discharge Parameters in GIS using Acoustic Emission Techniques", *J. Sound Vib.*, Vol. 247, No. 2, pp.243-260, 2001.
- [37] L. E. Lundgaard, "Partial Discharge Part XIV : Acoustic Partial Discharge Detection-Practical Application", *IEEE Electr. Insul. Mag.*, Vol. 8, No. 5, pp.34-43, 1992.
- [38] L. Yang, M. D. Judd, and C. J. Bennoch, "Time Delay Estimation for UHF Signal in PD Location of Transformer", *Annual Report Conference on Electrical Insulation and Dielectric Phenomena*, pp.414-417, 2004.
- [39] S. M. Markalous, S. Tenbohlen, and K. Fesor, "Detection and Location of Partial Discharges in Power Transformers using Acoustic and Electromagnetic Signals", *IEEE Trans. Dielectr. Electr. Insul.*, Vol. 15, No. 6, pp. 1576-1583, 2008.
- [40] S. Chakravorti, D. Dey, and B. Chatterjee, Biswendu, "Recent Trends in the Condition Monitoring of Transformers Theory, Implementation and Analysis", Springer, London, United Kingdom, 2013.
- [41] H. Zhu, V. Green, M. Sasic, and S. Halliburton, "Increased Sensitivity of Capacitive Couplers for In-service PD Measurement in Rotating Machines", *IEEE Trans. Energy Convers.*, Vol. 14, No 4, pp. 1184-1192, 1999.
- [42] M. S. Kim, "A Study on the Characteristics of Partial Discharge under HVDC in SF<sub>6</sub> Gas", Master Thesis, The Graduate School of Korea Maritime and Ocean University, 2014.

- [43] Z. S. Zhang, D. M. Xiao, and Y. Li, “Rogowski Air Coil Sensor Technique for On-line Partial Discharge Measurement of Power Cables”, IET Sci. Meas. Technol., Vol. 3, No. 3, pp. 187-196, 2009.
- [44] T. Yamagiwa and F. Endo, “Partial Discharge and its Application to Gas Insulated Switchgear”, Gaseous Dielectrics X, pp. 113-122, 2004.
- [45] CIGRE TF 15/33.03.05, “Partial Discharge Detection System for GIS: Sensitivity Verification for the UHF Method and the Acoustic Method”, ELECTRA, No. 183, pp. 75-87, 1999.
- [46] C. Neumann, B. Krampe, R. Feger, K. Feser, M. Knapp, A. Breuer, and V. Rees, “PD Measurements on GIS of Different Designs by Non-conventional UHF Sensors”, CIGRE Publication, Paris, France, 2000.
- [47] IEC 60599, “Mineral Oil-impregnated Electrical Equipment in Service – Guide to the Interpretation of Dissolved and Free Gases Analysis”, 2nd Edition, IEC Publication, Geneva, Switzerland, 2017.
- [48] IEEE C57.104, “Guide for the Interpretation of Gases Generated in Oil-immersed Transformers”, IEEE Power Engineering Society, New York, United State, 2009.
- [49] M. Duval and A. dePabla, “Interpretation of Gas-in-oil Analysis using New IEC Publication 60599 and IEC TC10 Databases”, IEEE Electr. Insul. Mag., Vol. 17, No. 2, pp. 31-41, 2001.
- [50] J. Tang, F. P. Zeng, X. X Zhang, J. Y. Pan, Q. Yao, X. Z. Hou, and Y. Tang, “Relationship between Decomposition Gas Ratios and Partial Discharge Energy in GIS, and the Influence of Residual Water and Oxygen”, IEEE Trans. Dielectr. Electr. Insul., Vol. 24, No. 3, pp. 1126-1234, 2014.

- [51] OMICRON, "Why Partial Discharge Testing Makes Good Sense", 2018.
- [52] W. Koltunowicz and R. Plath, "Synchronous Multi-channel PD Measurements", IEEE Trans. Dielectr. Electr. Insul., Vol. 15, No. 6, pp. 1715-1723, 2008.
- [53] I. Daubechies, "The Wavelet Transform, Time-Frequency Localization and Signal Analysis", IEEE Trans. Inform. Theory, Vol. 36, No. 5, pp. 961-1005, 1990.
- [54] M. Vetterli and C. Herley, "Wavelets and Filter Banks: Theory and Design", IEEE Trans. Signal Process., Vol. 40, No. 9, pp. 2207-2232, 1992.
- [55] B. Moula, A. Mekhaldil, M. Teguvar, and A. Haddad, "Characteristics of Discharge on Non-uniformly Polluted Glass Surfaces using a Wavelet Transform Approach", IEEE Trans. Dielectr. Electr. Insul., Vol. 20, No. 4, pp. 1457-1466, 2013.
- [56] J. Ramirez-Nifio, S. Rivera-Castaneda, V. R. Garcia-Colon, and V. M. Castano, "Analysis of Partial Electrical Discharges in Insulating Materials through the Wavelet Transform", Comput. Mater. Sci., Vol. 9, No. 3, pp. 379-388, 1998.
- [57] I. Shim, I. J. Soraghan, and W. H. Siew, "Detection of PD Utilizing Digital Signal Processing Method. Part 3: Open-loop Noise Reduction", IEEE Electr. Insul. Mag., Vol. 17, No. 1, pp. 6-13, 2001.
- [58] J. Li, T. Jiang, S. Grzybowski, and C. Cheng, "Scale Dependent Wavelet Selection for De-noising of Partial Discharge Detection", IEEE Trans. Dielectr. Electr. Insul., Vol. 17, No. 6, pp. 1705-1714, 2010.
- [59] C. F. F. C. Cunha, A. T. Carvalho, M. R. Petraglia, and A. C. S. Lima, "A New Wavelet Selection Method for Partial Discharge Denoising", Electric Power Syst. Res., Vol. 125, pp. 184-196, 2015.

- [60] G. E. Smith, K. Wood bridge, and C. J. Baker, "Radar Micro-doppler Signature Classification using Dynamic Time Warping", IEEE Trans. Aerosp. Electron. Syst., Vol. 46, No. 3, pp. 1078-1096, 2010.
- [61] H. Sakoe, and S. Chiba, "Dynamic Programming Algorithm Optimization for Spoken Word Recognition", IEEE Trans. Audio, Speech, Language Process., Vol. 26, No. 1, pp. 43-49, 1978.
- [62] S. Salvador and P. Chan, "Toward Accurate Dynamic Time Warping in Linear Time and Space", Intelligent Data Analysis, Vol. 11, No. 5, pp. 561-580, 2007.
- [63] L. Yang, M. D. Judd, and C. J. Bennoch, "Denoising UHF Signal for PD Detection in Transformers Based on Wavelet Technique", IEEE Annual Report Conference on Electrical Insulation and Dielectric Phenomena, pp.166-169, 2004.
- [64] National Instruments, Advanced Signal Processing Toolkit: Wavelet Analysis Tools User Manual, 2005.
- [65] S. Sriram, S. Nitin, K. M. M. Prabhu, and M. J. Bastiaans, "Signal Denoising Techniques for Partial Discharge Measurements", IEEE Trans. Dielectr. Electr. Insul., Vol. 12, No. 6, pp. 1182-1191, 2005.



## Paper Publication

### © International Journal

- [1] Hyang-Eun Jo, Gi-Woo Jeong, Guoming Wang, Gyung-Suk Kil, and Sung-Wook Kim, Identification of Defect Types by Analysis of PD Pulses in SF<sub>6</sub> Gas, International Journal of Applied Engineering Research, Vol. 10, No. 19, pp. 40703-40708, October 2015. (SCOPUS)
- [2] Hyang-Eun Jo, Guoming Wang, Sun-Jae Kim, and Gyung-Suk Kil, Comparison of Partial Discharge Characteristics in SF<sub>6</sub> Gas Under AC and DC, Transactions on Electrical and Electronic Materials, Vol. 16, No. 6, pp. 323-327, December 2015. (SCOPUS, EI)
- [3] Sung-Wook Kim, Jae-Ryong Jung, Guoming Wang, Sun-Jae Kim, and Gyung-Suk Kil, Classification of PD Defects in Gas Insulated Switchgears under HVDC, International Journal of Applied Engineering Research, Vol. 11, No. 4, pp. 2235- 2239, February 2016. (SCOPUS)
- [4] Guoming Wang, Hyang-Eun Jo, Sun-Jae Kim, Sung-Wook Kim, and Gyung-Suk Kil, Measurement and Analysis of Partial Discharges in SF<sub>6</sub> Gas under HVDC, Measurement, Vol. 91, pp. 351-359, September 2016. (SCIE)
- [5] Guoming Wang, Sun-Jae Kim, Seo-Jun Park, Gyung-Suk Kil, and Hong-Keun Ji, Optimal Design of a Follow Current Disconnecter for DC Arresters in Traction Vehicles, Transactions on Electrical and Electronic Materials, Vol. 17, No. 5, pp. 289-292, October 2016. (SCOPUS, EI)

- [6] Guoming Wang, Sun-Jae Kim, Gyung-Suk Kil, and Sung-Wook Kim, Optimization of Wavelet and Thresholding for Partial Discharge Detection under HVDC, IEEE Transactions on Dielectrics and Electrical Insulation, Vol. 24, No. 1, pp. 200-208, February 2017. (SCI)
- [7] Guoming Wang, Seong-Cheol Hwang, Gyung-Suk Kil, and Kyu-Lyong Cho, 110V/220V Auto-selection Method for an LED Bulb on Shipboard, International Journal of Applied Engineering Research, Vol. 12, No. 6, pp. 877-881, March 2017. (SCOPUS)
- [8] Hong-Keun Ji, Young-Jin Cho, Guoming Wang, Seong-Cheol Hwang, and Gyung-Suk Kil, Extraction of Series Arc Signals Based on Wavelet Transform in an Indoor Wiring System, Transactions on Electrical and Electronic Materials, Vol. 18, No. 4, pp. 221-224, August 2017. (SCOPUS, EI)
- [9] Guoming Wang and Gyung-Suk Kil, Measurement and Analysis of Partial Discharge using an Ultra-high Frequency Sensor for Gas Insulated Structure, Metrology and Measurement Systems, Vol. 24, No. 3, pp. 515-524, September 2017. (SCIE)
- [10] Guoming Wang, Gyung-Suk Kil, Hong-Keun Ji, and Jong-Hyuk Lee, Disturbance Elimination for Partial Discharge Detection in the Spacer of Gas-Insulated Switchgears, Energies, Vol. 10, No. 11, pp. 1762(1)-(12), November 2017. (SCIE)
- [11] Hyang-Eun Jo, Guoming Wang, Sun-Jae Kim, and Gyung-Suk Kil, Partial Discharge Characteristics in SF<sub>6</sub>-N<sub>2</sub> Mixture Gases Under High Voltage Direct Current, Science of Advanced Materials, Vol. 10, No. 2, pp. 275 - 278, February 2018. (SCIE)

- [12] Guoming Wang, Seong-Cheol Hwang, Woo-Hyun Kim, and Gyung-Suk Kil, Design and Fabrication of an LED Lantern based on Light Condensing Technology, Journal of International Council on Electrical Engineering, Vol. 8, No. 1, pp. 14-18, February 2018.
- [13] Sung-Wook Kim, Jae-Ryong Jung, Young-Min Kim, Gyung-Suk Kil, and Guoming Wang, New Diagnosis Method of Unknown Phase-shifted PD Signals for Gas Insulated Switchgears, IEEE Transaction on Dielectrics and Electrical Insulation, Vol. 25, No. 1, pp. 102-109, February 2018. (SCI)
- [14] Hong-Keun Ji, Guoming Wang, Woo-Hyun Kim, and Gyung-Suk Kil, Optimal Design of a Band Pass Filter and an Algorithm for Series Arc Detection, Energies, Vol. 11, pp. 992(1)-(13), April 2018. (SCIE)
- [15] Guoming Wang, Woo-Hyun Kim, Jeong-Bae Kong, Gyung-Suk Kil, and Hong-Keun Ji, Analysis of PD Signal for Condition Monitoring of MV Switchboards by the Measurement of Transient Earth Voltage, Transactions on Electrical and Electronic Materials, Vol. 19, No. 3, pp. 195-200, June 2018. (SCOPUS, EI)
- [16] Guoming Wang, Woo-Hyun Kim, Hong-Keun Ji, and Gyung-Suk Kil, Detection and Analysis of Series Arc using Non-conventional Methods in Low-voltage Switchboards, Journal of Electrical Engineering, Vol. 69, No. 4, pp. 317-322, August 2018. (SCIE)
- [17] Guoming Wang, Woo-Hyun Kim, Jong-Hyuk Lee, and Gyung-Suk Kil, Condition Monitoring and Deterioration Analysis of Metal Oxide Varistor, Journal of Electrical Engineering, Vol. 69, No. 5, pp. 352-358, October 2018. (SCIE)

- [18] Guoming Wang, Woo-Hyun Kim, Gyung-Suk Kil, Sung-Wook Kim, and Jae-ryong Jung, Green Gas for Grid as an Eco-Friendly Alternative Insulation Gas to SF<sub>6</sub>: From the Perspective of Partial Discharge under AC, Applied Sciences, Vol. 9, No. 4, 651, February 2019. (SCIE)
- [19] Guoming Wang, Woo-Hyun Kim, Gyung-Suk Kil, Dae-Won Park, and Sung-Wook Kim, An Intelligent Lightning Warning System Based on Electromagnetic Field and Neural Network, Energies, Vol. 12, No.7, pp. 1275(1)-(11), April 2019. (SCIE)

© **Korean Journal**

- [1] Sun-Jae Kim, Hyang-Eun Jo, Guoming Wang, Min-Young Yun, and Gyung-Suk Kil, Partial Discharge Characteristics of Metallic Particles Under HVDC in SF<sub>6</sub> Gas, Journal of the Korean Institute of Electrical and Electronic Material Engineers, Vol. 28, No. 12, pp. 831-836, 2015.
- [2] Hyang-Eun Jo, Guoming Wang, Sun-Jae Kim, Kyoung-Soo Park, and Gyung-Suk Kil, Partial Discharge Characteristics on Protrusion Defects in SF<sub>6</sub>-N<sub>2</sub> Mixture Gases, Journal of the Korean Institute of Electrical and Electronic Material Engineers, Vol. 29, No. 1, pp. 44-49, 2016.
- [3] Min-Young Yun, Kyoung-Soo Park, Guoming Wang, Sun-Jae Kim, and Gyung-Suk Kil, Analysis of Propagation Characteristics of Acoustic Signal in Insulation Oil, Journal of the Korean Institute of Electrical and Electronic Material Engineers, Vol. 29, No. 2, pp. 114-119, 2016.
- [4] Sun-Jae Kim, Guoming Wang, Seo-Jun Park, Gyung-Suk Kil, and Chang-Hwan An, Analysis of Partial Discharge Characteristics in SF<sub>6</sub> Gas Insulation, Journal of the Korean Institute of Electrical and Electronic Material Engineers, Vol. 29, No. 7, pp. 429-434, 2016.
- [5] Kyoung-Soo Park, Guoming Wang, Seong-Cheol Hwang, Sun-Jae Kim, and Gyung-Suk Kil, Deterioration Characteristics and an On-Line Diagnostic Equipment for Surge Protective Devices, Journal of the Korean Institute of Electrical and Electronic Material Engineers, Vol. 29, No. 10, pp. 635-640, 2016.
- [6] Seo-Jun Park, Seong-Cheol Hwang, Guoming Wang, and Gyung-Suk Kil, Partial Discharge Characteristics and Localization of Void Defects in XLPE Cable, Journal of the Korean Society for Railway, Vol. 20, No. 2, pp. 203-209, 2017.

- [7] Woo-Hyun Kim, Seong-Cheol Hwang, Guoming Wang, Gyung-Suk Kil, and Chang-Hwan Ahn, Electrical Characteristic Changes of ZnO Varistors by Energy Absorption, Journal of the Korean Institute of Electrical and Electronic Material Engineers, Vol. 30, No. 12, pp. 817-821, 2017.
- [8] Guoming Wang, Woo-Hyun Kim, Tae-Ho Kang, and Gyung-Suk Kil, Comprehensive Study on Accelerated Degradation of Metal Oxide Varistors, Journal of the Korean Society for Railway, Vol. 21, No. 7, pp. 641-648, 2018.
- [9] Woo-Hyun Kim, Guoming Wang, Gyung-Suk Kil, and Hong-Keun Ji, Detection and Identification of the Series Arc in an Indoor Wiring System, Journal of the Korean Institute of Electrical and Electronic Material Engineers, Vol. 31, No. 6, pp. 412-416, 2018.
- [10] Woo-Hyun Kim, Guoming Wang, Gyung-Suk Kil, Do-Jung Kim, Bong-Won Seo, Su-Young Kim, and Young-Moon Kim, Design and Fabrication of an Underwater Visualization Rescue-rope, Journal of the Korean Society of Marine Engineering, Vol. 42, No. 9 pp. 767-771, 2018.
- [11] Woo-Hyun Kim, Guoming Wang, Tae-Ho Kang, Gyung-Suk Kil, Sung-Wook Kim, Optimal Design of a TEV Sensor for Partial Discharge Detection, Journal of the Korean Society for Railway, Vol. 22, No. 2, pp. 140-149, 2019.

© **Proceedings of International Conference**

- [1] Jin-Wook Kim, Se-Jin Kim, Sun-Jae Kim, Guoming Wang, and Gyung-Suk Kil, “Development of the LED Searchlight for Vessels”, 20th International Conference on Electrical Engineering, pp.1914-1919, Korea, June 15-19, 2014.
- [2] Guoming Wang, Hyang-Eun Jo, Sun-Jae Kim, and Gyung-Suk Kil, Comparison of Partial Discharge Pulse Waveforms Between AC and DC Voltages in SF<sub>6</sub> Gas, 21st International Conference on Electrical Engineering, pp.398(1)- 398(4), Hong Kong, July 5-9, 2015.
- [3] Jin-Wook Kim, Guoming Wang, Min-Young Yun, and Gyung-Suk Kil, A Condensing Technology for a LED Searchlight, 21st International Conference on Electrical Engineering, pp.400(1)-400(5), Hong Kong, July 5-9, 2015.
- [4] Guoming Wang, Sun-Jae Kim, Hyang-Eun Jo, Gyung-Suk Kil, and Sung-Wook Kim, Partial Discharge Localization in Insulation Oil by Electrical-Acoustic Method, 19th International Symposium on High Voltage Engineering, pp.209(1)- 209(4), Czech, August 23-28, 2015.
- [5] Guoming Wang, Sun-Jae Kim, Hyang-Eun Jo, Gi-Woo Jeong, and Gyung-Suk Kil, Algorithm for Defects Identification by Analysis of PD Pulses in SF<sub>6</sub> Gas, 9th International Symposium on High Voltage Engineering, pp.165(1)-165(5), Czech, August 23-28, 2015.
- [6] Hyang-Eun Jo, Sun-Jae Kim, Guoming Wang, Gyung-Suk Kil, and Sung-Wook Kim, Analysis of DIV and DEV in SF<sub>6</sub>-N<sub>2</sub> Mixture Gas, 19th International Symposium on High Voltage Engineering, pp.134(1)-134(4), Czech, August 23-28,2015.

- [7] Hyang-Eun Jo, Guoming Wang, Sun-Jae Kim, Gyung-Suk Kil, Partial Discharge Characteristics under DC in SF<sub>6</sub>-N<sub>2</sub> Mixture Gas, 3th International Conference on Advanced Electromaterials, p.116, Korea, November 17-20, 2015.
- [8] Guoming Wang, Sun-Jae Kim, Seo-Jun Park, and Gyung-Suk Kil, Design and Fabrication of a Dual Voltage LED Bulb, International Conference on Electrical Engineering 2016, pp.90387(1)~(4), Japan, July 3-7, 2016.
- [9] Kyoung-Soo Park, Guoming Wang, Sun-Jae Kim, Tae-Seong Kim, and Gyung-Suk Kil, Design and Fabrication of an LED Searchlight, International Conference on Electrical Engineering 2016, pp.90394(1)~(5), Japan, July 3-7, 2016.
- [10] Guoming Wang, Seo-Jun Park, Gyung-Suk Kil, Sun-Jae Kim, and Sung-Wook Kim, Analysis of Partial Discharge Characteristics by UHF Sensors, 1st Seoul International Electric Fair Conference, pp.2-25, Korea, October 5-7, 2016.
- [11] Guoming Wang, Seo-Jun Park, Seong-Cheol Hwang, and Gyung-Suk Kil, De-noising of Partial Discharge Pulses under HVDC Based on Wavelet Transform, 1st Seoul International Electric Fair Conference, pp.38-41, Korea, October 5-7, 2016.
- [12] Seo-Jun Park, Guoming Wang, Seong-Cheol Hwang, Gyung-Suk Kil, and Eun-Je Jo, Insulation Diagnostic Techniques for High Voltage DC Cable, 1st Asian Conference on Railway Infrastructure and Transportation, pp.252-255, Korea, October 19-20, 2016.
- [13] Guoming Wang, Seo-Jun Park, Gyung-Suk Kil, Sung-Wook Kim, and Hee-Chul Park, Condition Monitoring and Diagnosis by the Analysis of Partial Discharge Pattern for Gas Insulated Switchgears, 1st Asian Conference on Railway Infrastructure and Transportation, pp.256-259, Korea, October 19-20, 2016.



- [14] Guoming Wang, Seong-Cheol Hwang, and Gyung-Suk Kil, Determination of the Time Difference of Arrival for Acoustic Emission Signals Induced by Partial Discharge in Power Transformers, International Conference on Electrical Engineering 2017, pp.1140-1143, China, July 4-7, 2017.
- [15] Seong-Cheol Hwang, Guoming Wang, and Gyung-Suk Kil, Defect Localization by the Time Domain Reflectometry Method in an XLPE Cable, International Conference on Electrical Engineering 2017, pp.1150-1153, China, July 4-7, 2017.
- [16] Guoming Wang, Seong-Cheol Hwang, and Gyung-Suk Kil, Design and Fabrication of an LED Lantern, International Conference on Electrical Engineering 2017, China, pp.2023-2025, July 4-7, 2017.
- [17] Seong-Cheol Hwang, Guoming Wang, and Gyung-Suk Kil, Design of an LED Searchlight based on Light Condensing Technology, International Conference on Electrical Engineering 2017, pp.2026-2029, China, July 4-7, 2017.
- [18] Guoming Wang, Seong-Cheol Hwang, Jeong-Bae Kong, and Gyung-Suk Kil, Reduction of Leakage Current in an EMP Filter Equipped with Surge Protective Device, International Symposium on Marine Engineering and Technology, pp.104- 105, Korea, October 26-27, 2017.
- [19] Guoming Wang, Seong-Cheol Hwang, Woo-Hyun Kim, and Gyung-Suk Kil, Protection Performances of Thermally Protected Metal-Oxide Varistor, International Symposium on Marine Engineering and Technology, pp.106-107, Korea, October 26-27, 2017.
- [20] Guoming Wang, Woo-Hyun Kim, and Gyung-Suk Kil, Design and Fabrication of an LED Searchlight for Drones, 2018 International Conference on Engineering, Technology, and Applied Science (ICETA 2018), pp. 1-5, China Taiwan, June 25-27, 2018.

- [21] Woo-Hyun Kim, Guoming Wang, and Gyung-Suk Kil, A LED Lighting System for Biorhythm Adjustment of Marine Life, 2018 International Conference on Engineering, Technology, and Applied Science (ICETA 2018), pp. 1-5, China Taiwan, June 25-27, 2018.
- [22] Woo-Hyun Kim, Guoming Wang, and Gyung-Suk Kil, Lifetime Predication of Metal-oxide Varistor based on Absorbed Energy, 2018 International Conference on Engineering, Technology, and Applied Science (ICETA 2018), pp. 1-5, China Taiwan, June 25-27, 2018.
- [23] Guoming Wang, Woo-Hyun Kim, Gyung-Suk Kil, and Il-Kwon Kim, Design and Fabrication of a LED Headlight System for High-speed Trains, The 2nd Asian Conference on Railway Engineering and Transportation (ART 2018), pp. 38(1)-(3), Korea, October 17-19, 2018.
- [24] Woo-Hyun Kim, Guoming Wang, Gyung-Suk Kil, Dae-Won Park, and Tae-Seong Kim, An Investigation on the Necessity of Introducing Lightning Warning System in Railway System, 2nd Asian Conference on Railway Engineering and Transportation (ART 2018), pp. 38(1)-(3), Korea, October 17-19, 2018.

◎ **Proceedings of Domestic Conference**

- [1] Gi-Woo Jeong, Sun-Jae Kim, Guoming Wang, and Gyung-Suk Kil, Design and Fabrication of On-Line Lightning Arrester Analyzer for Traction, 2014 Spring Conference of the Korean Society for Railway, pp.145(1)-145(5), 2014.
- [2] Sun-Jae Kim, Gi-Woo Jeong, Guoming Wang, and Gyung-Suk Kil, Seasonal Variation of Ground Impedance for a Copper-rods and a Carbon-block, 2014 Spring Conference of the Korean Society for Railway, pp.147(1)-147(6), 2014.
- [3] Hee-Ju Ha, Hyang-Eun Jo, Guoming Wang, Gyung-Suk Kil, and Byung-Kwon Choi, Operation Characteristics of LEDs at Ultra-low Temperature, The 38th Korean Society of Marine Engineering Spring Conference, p.123, 2014.
- [4] Guoming Wang, Sun-Jae Kim, Hee-Ju Ha, Kyoung-Soo Park, and Gyung-Suk Kil, Operating Characteristics of LED Bulbs at Ultra Low Temperature, The 38th Korean Society of Marine Engineering Fall Conference, p.125, 2014.
- [5] Sun-Jae Kim, Jin-Wook Kim, Gi-Woo Jeong, Guoming Wang, and Gyung-Suk Kil, Design and Fabrication of a LED Working Light for Vessels, The 38th Korean Society of Marine Engineering Fall Conference, p.121, 2014.
- [6] Guoming Wang, Sun-Jae Kim, Hee-Ju Ha, Kyoung-Soo Park, and Gyung-Suk Kil, Partial Discharge Characteristics in SF<sub>6</sub> Gas under HVDC, The Korean Institute of Electrical and Electronic Material Engineers Annual Autumn Conference, p.91, 2014.

- [7] Hyang-Eun Jo, Sun-Jae Kim, Guoming Wang, and Gyung-Suk Kil, Analysis of Partial Discharge Characteristics under AC and DC in SF<sub>6</sub> Gas, 2015 Spring Conference of the Korean Society for Railway, pp.KSR2015S306(1)-(5), 2015.
- [8] Sun-Jae Kim, Guoming Wang, Min-Young Yun, and Gyung-Suk Kil, Partial Discharge Characteristics according to Particle Types in SF<sub>6</sub> Gas, 2015 Autumn Conference of the Korean Society for Railway, pp.KSR2015A281(1)-(6), 2015.
- [9] Kyoung-Soo Park, Sun-Jae Kim, Guoming Wang, Seong-Cheol Hwang, and Gyung-Suk Kil, Deterioration Characteristics of a Railway Arrester by Lightning Impulse Current, 2016 Spring Conference of the Korean Society for Railway, pp.KSR2016S208(1) -(5), 2016.
- [10] Seo-Jun Park, Sun-Jae Kim, Guoming Wang, Gyung-Suk Kil, and Eun-Je Jo, A Study on the Insulation Diagnosis of DC Cable, 2016 Spring Conference of the Korean Society for Railway, pp.KSR2016S209(1)-(4), 2016.
- [11] Kyoung-Soo Park, Sun-Jae Kim, Guoming Wang, Seong-Cheol Hwang, Gyung-Suk Kil, and Sung-Wook Kim, Characteristics of Partial Discharge Depending on Defects in GIS, 2016 Spring Conference of the Korean Society for Railway, pp.KSR2016S210(1)-(5), 2016.
- [12] Guoming Wang, Sun-Jae Kim, Kyoung-Soo Park, and Gyung-Suk Kil, Fabrication and Characteristics of a Disconnecter for DC Lightning Arrester, The Korean Institute of Electrical and Electronic Material Engineers Annual Summer Conference, p74, 2016.

- [13] Seo-Jun Park, Seong-Cheol Hwang, Guoming Wang, and Gyung-Suk Kil, Detection of Series Arc Signals by TEV Sensor in Low-voltage Switchboard, 2016 Autumn Conference of the Korean Society for Railway, pp.KSR2016A257 (1)-(5), 2016.
- [14] Seo-Jun Park, Seong-Cheol Hwang, Guoming Wang, and Gyung-Suk Kil, Analysis of PD Characteristics by Void Position in XLPE Cables, The Korean Institute of Electrical and Electronic Material Engineers Annual Autumn Conference, p33, 2016.
- [15] Seong-Cheol Hwang, Seo-Jun Park, Guoming Wang, and Gyung-Suk Kil, Design and Fabrication of an LED Searchlight for High-speed Boat, The Korean Institute of Electrical and Electronic Material Engineers Annual Autumn Conference, p34, 2016.
- [16] Guoming Wang, Seong-Cheol Hwang, and Gyung-Suk Kil, Design and Fabrication of a 10 W LED Searchlight, the 41th Korean Society of Marine Engineering Spring Conference, p.368, 2017.
- [17] Seong-Cheol Hwang, Guoming Wang, Gyung-Suk Kil, In-Gwan Kim, and Byeong-Sam Kim, Design and Fabrication of a LED Marine Lantern, the 41th Korean Society of Marine Engineering Spring Conference, p.369, 2017.
- [18] Seong-Cheol Hwang, Guoming Wang, and Gyung-Suk Kil, Characteristic Changes of SF<sub>6</sub> Gas by Partial Discharge, 2017 Spring Conference of the Korean Society for Railway, pp.KSR2017S216(1)-(4), 2017.
- [19] Sung-Wook Kim, Jae-Ryong Jung, Yong-Min Kim, Guoming Wang, and Gyung-Suk Kil, PD Diagnosis Method based on Non-phase Synchronized Patterns, 2017 Spring Conference of the Korean Society for Railway, pp.KSR2017S217(1)-(3), 2017.

- [20] Hong-Keun Ji, Young-Jin Cho, Guoming Wang, Seong-Cheol Hwang, and Gyung-Suk Kil, Frequency Characteristic Analysis of Current Signal by Series Arc Discharge, The 48th Korean Institute of Electrical Engineers Summer Conference, pp.1188-1189, 2017.
- [21] Guoming Wang, Seong-Cheol Hwang, Woo-Hyun Kim, and Gyung-Suk Kil, Partial Discharge Diagnosis Technique for Power Facilities in Switchboards, 2017 Autumn Conference of the Korean Society for Railway, pp.KSR2017A175(1)-(2), 2017.
- [22] Guoming Wang, Seong-Cheol Hwang, Woo-Hyun Kim, and Gyung-Suk Kil, Detection Method of Leakage Current for Condition Monitoring of Surge Protective Devices, 2017 Autumn Conference of the Korean Society for Railway, pp.KSR2017A176(1)-(2), 2017.
- [23] Seong-Cheol Hwang, Jeong-Bae Kong, Guoming Wang, and Gyung-Suk Kil, Analysis on the Leakage Current Components of ZnO Varistors by Deterioration, 2017 Autumn Conference of the Korean Society for Railway, pp.KSR2017A178(1)-(2), 2017.
- [24] Guoming Wang, Woo-Hyun Kim, Gyung-Suk Kil, Dae-Won Park, and Tae-Seong Kim, Design and Evaluation of a Portable Light-condensed LED Searchlight, the 42nd Korean Society of Marine Engineering Spring Conference, p.277, 2018.
- [25] Woo-Hyun Kim, Guoming Wang, Gyung-Suk. Kil, D. J. Kim, B. W. Seo, S. Y. Kim, and Y. M. Kim, Visualization of a Underwater Rescue-rope using Optical Fiber, the 42nd Korean Society of Marine Engineering Spring Conference, p.278, 2018.

- [26] Guoming Wang, Woo-Hyun Kim, and Gyung-Suk Kil, Design of a Surge Generator using Coupling and Decoupling Network for Energized Test, 2018 Spring Conference of the Korean Society for Railway, pp.KSR2018S088(1)~(2), 2018.
- [27] Woo-Hyun Kim, Guoming Wang, and Gyung-Suk Kil, Detection Method of Series Arc in Wiring Systems, 2018 Spring Conference of the Korean Society for Railway, pp. KSR2018S104(1)~(2), 2018.
- [28] Woo-Hyun Kim, Guoming Wang, Gyung-Suk. Kil, D. J. Kim, B. W. Seo, S. Y. Kim, and Y. M. Kim, Performance Evaluation of Underwater LED Rescue-rope, the 42nd Korean Society of Marine Engineering Fall Conference, p. 233, 2018.
- [29] Woo-Hyun Kim, Guoming Wang, Tae-Ho Kang, and Gyung-Suk Kil, An LED Lantern using Fresnel Lens, The Korean Institute of Electrical and Electronic Material Engineers Annual Autumn Conference, p.45, 2018.
- [30] Guoming Wang, Woo-Hyun Kim, Tae-Ho Kang, and Gyung-Suk Kil, Analysis on Electrical Characteristics of MOV for Its On-line Diagnosis, The Korean Institute of Electrical and Electronic Material Engineers Annual Autumn Conference, p.46, 2018.
- [31] Guoming Wang, Woo-Hyun Kim, Tae-Ho Kang, and Gyung-Suk Kil, Development of a Lightning Warning System using Electromagnetic Sensors, The Korean Institute of Electrical and Electronic Material Engineers Annual Autumn Conference, p.50, 2018.
- [32] Guoming Wang, Woo-Hyun Kim, Nam-Hoon Kim, and Gyung-Suk Kil, Localization of Lightning Strike using Loop Antennas, 2019 Spring Conference of the Korean Society for Railway, pp. KSR2019S068(1)~(2), 2019.

- [33] Nam-Hoon Kim, Woo-Hyun Kim, Guoming Wang, and Gyung-Suk Kil, Concept Design of a High Power EMP Generator Antennas, 2019 Spring Conference of the Korean Society for Railway, pp. KSR2019S069(1)~(2), 2019.
- [34] Woo-Hyun Kim, Guoming Wang, Nam-Hoon Kim, and Gyung-Suk Kil, Design and Fabrication of an Electronic Relay for 3-phase Induction Motor Protection, 2019 Spring Conference of the Korean Society for Railway, pp. KSR2019S074(1)~(2), 2019.
- [35] Woo-Hyun Kim, Guoming Wang, Nam-Hoon Kim, and Gyung-Suk Kil, A Study on the TEV Sensor for Insulation Diagnosis of Electrical Power Apparatus, 2019 Spring Conference of the Korean Society for Railway, pp. KSR2019S075(1)~(2), 2019.
- [36] Guoming Wang, Woo-Hyun Kim, Nam-Hoon Kim, and Gyung-Suk Kil, Comparisons of Partial Discharge Characteristics in SF<sub>6</sub> and g<sub>3</sub> Gas, The Korean Institute of Electrical and Electronic Material Engineers Summer Autumn Conference, p.50, 2019.
- [37] Guoming Wang, Woo-Hyun Kim, Nam-Hoon Kim, and Gyung-Suk Kil, An Intelligent Lightning Warning Algorithm based on Neural Network, The Korean Institute of Electrical and Electronic Material Engineers Summer Autumn Conference, p.50, 2019.
- [38] Woo-Hyun Kim, Guoming Wang, Nam-Hoon Kim, and Gyung-Suk Kil, Development of a Smart Searchlight using High Power LED, The Korean Institute of Electrical and Electronic Material Engineers Summer Autumn Conference, p.63, 2019.



## 감사의 글

### 致谢

2013년 9월 1일부터 연구실에서 석사과정으로 시작하여 글을 쓰는 현재는 박사과정 졸업을 앞두고 있습니다. 한국에서 6년 동안 어려운 상황이 많았지만, 수많은 분들의 격려와 도움이 있었기에 이루어 낼 수 있었습니다. 도와주신 모든 분들께 진심으로 감사의 마음을 전하고자 합니다.

가장 먼저, 대학원에서 공부할 수 있는 기회를 주시고, 지도와 격려를 아끼지 않으신 길경석 교수님께 깊은 감사를 드립니다. 학문적인 지도뿐만 아니라 인생의 스승으로서 저에게 소중한 가르침을 주셨습니다. 교수님 같은 훌륭하신 분을 스승으로 만날 수 있었던 것은 제 인생에 있어 큰 행운이었습니다. 오늘 그리고 앞으로의 제가 있게 해 신 교수님의 높이신 은혜를 평생 뼈 속까지 새겨서 살겠습니다. 교수님의 가르침과 격려를 바탕으로 사회에 나가 부끄럽지 않은 제자가 되도록 노력 하겠습니다. 다시 한 번 고개 숙여 감사를 올립니다.

바쁘신 와중에도 논문 완성을 위해 세심하게 심사해 주신 김윤식 교수님(위원장님)과 장낙원 교수님, 먼 길 마다하지 않으시고 많은 가르침을 주신 한국전기안전공사 이영식 박사님, 신라대학교 윤중환 교수님께 진심으로 감사의 말씀을 드립니다. 소중한 지도와 의견을 덕분에 논문을 완수할 수 있었습니다. 더불어 대학원 및 논문심사 과정에서 많은 가르침을 주신 이성근 교수님, 전태인 교수님, 서동환 교수님, 주양익 교수님께 감사드립니다.

한국에서 6년 동안 가족과 같은 고전압연구실 모든 선·후배님께 진심으로 감사의 말씀을 드립니다.

연구실 잘 적응할 수 있도록 많은 도움을 주시고 응원해 주신 1대 방장이신 송재용 박사님, 2대 방장이신 박대원 박사님, 3대 방장이신 김선재 박사님께 감사의 마음을 전하고 싶습니다. 석사 과정 때부터 같이 연구실에서 생활하시고 많은 것을 알려 주신 김성욱 박사님, 지홍근 박사님, 조규룡 박사님, 조향은 박사님, 김민수 선배님, 김세진 선배님, 하희주 선배님, 정기우 선배님, 김진욱 선배님, 변성환 선배님께 감사합니다.

연구실에 함께 있어 힘이 되어 주신 후배 형님이신 김태성 석사님, 윤민영 석사님, 박경수 석사님, 박서준 석사님, 황성철 석사님에게도 고마움을 전하고 싶습니다. 자주 학교에 오셔서 응원해 주신 천상규 박사님, 조영진 박사님, 김일권 박사님, 주문노 박사님, 서재석 사장님, 이종혁 선배님, 서항동 선배님, 김황국 선배님, 최수연 선배님, 이정운 선배님, 진창환 선배님, 김동건 선배님께도 이 자리를 빌려 감사의 말씀을 전합니다.

항상 열정적이고 부지런한 모습을 보여 주는 김우현 후배님에게 고마움을 전하고 싶습니다. 2년 동안 많은 것을 도와 주워서 고맙습니다. 열심히 하는 만큼 결실을 맺기를 바랍니다. 연구실에서 잘 적응하고 열심히 하고 있는 강태호님과 김남훈님에게도 고맙습니다. 최선을 다하고 훌륭한 성과를 낼 수 있다고 믿도록 하겠습니다. 신입생 안동현님과 신한신님, 연구실을 잘 선택해서 축하합니다. 석사과정 동안 많이 배우고 성장하기 바랍니다. 그리고 파트타임 석사과정 공정배님, 김태수님, 이경렬님에게도 고마움을 전하고 싶습니다.

感谢父母，给了我生命，给了我所有的一切。是你们的关爱、支持和鼓励，让我成长、成熟，有机会异地求学，并取得博士学位。

感谢伟大祖国，高速发展与繁荣昌盛让我们见证到崭新的时代，也为我们提供了广阔的舞台和无限的机会。

感谢正林绿化工程有限公司的各位叔叔给予我的家庭和我个人无限的希望与帮助，你们是我人生的导师，也是我奋斗目标。

感谢杭州国洲电力科技有限公司的信任，我将以满腔热血和激情投入工作，助公司蓬勃发展，蒸蒸日上，成为行业内的先驱。

感谢成长道路上亲人、长辈、前辈、朋友，老师、同学的教诲与陪伴，感谢求职道路上企业、高校、猎头老师们提供的宝贵机会。

感谢女友，六年间，你未曾出现，使我得以专注于学习和研究。往后余生，我愿执你之手，与你偕老。

感谢自己多年来的坚持与努力。愿你不忘初心，自信，自律，感恩，明确目标，艰苦奋斗。

왕 국 명 王国明

Yeongdo-Gu, Busan, Republic of Korea, 2019.07.